Computational Studies of a few Heterogeneous and Homogeneous Electrocatalytic Conversion Processes for Renewable Energy

A Thesis
Submitted for the Degree of
Doctor of Philosophy
in the Faculty of Science

by

Neha Bothra

Theoretical Sciences Unit
Jawaharlal Nehru Centre for Advanced Scientific Research
(A Deemed University)
Bangalore-560064

January 2021

Dedicated to my Family...

DECLARATION

I hereby declare that the matter embodied in the thesis entitled "**Computational Studies of a few Heterogeneous and Homogeneous Electrocatalytic Conversion Processes for Renewable Energy**" is the result of investigations carried out by me at the New Chemistry Unit, Jawaharlal Nehru Centre for Advanced Scientific Research, Bangalore, India under the supervision of Prof. Swapan K. Pati and that it has not been submitted elsewhere for the award of any degree or diploma.

In keeping with the general practice in reporting scientific observations, due acknowledgement has been made whenever the work described is based on the findings of other investigators.

Neha Bothra

CERTIFICATE

I hereby certify that the matter embodied in this thesis entitled "**Computational Studies of a few Heterogeneous and Homogeneous Electrocatalytic Conversion Processes for Renewable Energy**" has been carried out by Ms. Neha Bothra at the Theoretical Science Unit, Jawaharlal Nehru Centre for Advanced Scientific Research, Bangalore, India under my supervision and that it has not been submitted elsewhere for the award of any degree or diploma.

Prof. Swapan K. Pati
(Research Supervisor)

Acknowledgements

Though only my name is printed in the thesis, these 5 years long journey is incomplete without many people, who have always been there with me to help or motivate or accompany. Here, in this section I would like to pay my gratitude to all of them.

First and foremost, I wish to thank my supervisor Prof. Swapan K. Pati, who has accepted me as his Ph. D. student and allowed me to pursue my interest in his group. His insightful guidance and continuous support in all respect have eased my research journey. Besides being a wonderful supervisor, he is a great person who has stood as a mentor to me beyond research. It is his friendly behaviour with students, which has kept the lab environment positive and warm.

I acknowledge Anusooya Ma'am and Sohan, whose company provided a homely atmosphere in an unknown place. I am grateful to Anusooya Ma'am for always being there whenever I needed a help in all respect. I can not thank her enough for her kind guidance during the colloquium along with my Guide.

I am also extremely grateful to Prof C.N.R. Rao, for this wonderful scientific institute, JNCASR. He is always an inspiration to strive for brilliance.

I am thankful to all my course instructors at JNC, Prof. Swapan K. Pati, Prof.

Shobhana Narasimhan, Prof. Umesh V. Waghmare, Prof. N. S. Vidhyadhiraja, Dr. Meher K. Prakash, Prof. S. Balasubramanian, who have taught me various courses. I am really grateful to my experimental collaborators Prof. Tapas K. Maji (JNCASR) and Prof. Prabeer Barpanda (IISC) for allowing me to find out the scientific reasons of their experimental observations and also to their students, Tarandeep, Krishnakanth, Ritambhari and Lalit for the fruitful discussions we had.

I am grateful to my seniors, Dr. Pallavi Bothra, Dr. Pralok K. Samanta, Dr. Sandhya Rai, Dr. Shubhajit Das who have helped me in various scientific aspects and the discussions with them were always exciting and insightful.

I thank my past and present colleagues at lab - Sharma, Dibyajyoti, Siam, Pallavi, Swastika, Bradraj, Arkamita, Ashvini, Sylvia, Sukanta, Pralok, Amrit, Fransesco, Madhuri, Nisheal, Shubhajit, Abhiroop, Madhulika, Sandhya, Raju, Pallavi, Navamani, Ganesh, Bidhan, Supriti, Anita, Paramita and Shazia. My special thanks to Madhulika for lending her laptop to me during pandemic.

I am thankful to the Academic Section, the Administration, Library, Complab and CCMS for up-keeping all the facilities here. I thank the NVSH and Student Residence staff, Dhanvantari, Utility and Dining Hall, for making my stay comfortable.

I want to thank my batchmates Ananya, Pallabi, Lakshay, Madhulika, Rajendra, Narendra, Niloy, Sreyan, Janky, Sukanya, Malay, Nalina, Sharon, Koyel. My special thanks to Nalina, Sharon, Arya, Ganesh and Raju to be always there with me, I could always count on them during my ups and downs.

A special thanks to my family, Papa, Mummy, Suman jiji and Puchu jiji for their endless support. I can never thank them enough for their love.

Synopsis

Human civilization in the 21^st century is at the cross road due to many factors which are affecting civilization. The major concerns are global warming, depletion of fossil fuel, greenhouse gas emission etc to name a few and these are creating an urgent need to find alternative resources. There are several alternative resources, namely solar, heat, chemical, electrical and electrochemical, but the most effective alternatives would be the one which is renewable, extremely effective, clean and cost-effective. The thesis deals with computational modelling of electrochemical conversion processes using both heterogeneous and homogeneous catalytic routes.

The thesis has eight chapters, including introduction, conclusion and outlook chapters and six work chapters. In the introduction chapter, we have briefly discussed the urgent requirement for renewable energy resources and all the possible routes. We have described the catalysts used experimentally as well as theoretically for heterogeneous and homogeneous catalytic reactions and how effective these are in water splitting to oxygen and hydrogen and carbon dioxide reduction processes. We also have described the thermodynamic and kinetic pathways for each of these electrocatalytic reactions for various catalysts.

All the computational tools considered here are based upon density functional

theory. Quantum Espresso package is used to calculate the activity of periodic systems in chapter 2, 3, 4 and 5. For OER, ORR and HER, we have calculated the free energy values of each step in order to have a detailed thermodynamic analysis. The homogeneous calculations are carried out using the Gaussian 16 package in chapter 6 and 7. Here, we have done kinetic and thermodynamic analyses for CO_2 reduction reaction in basic and neutral pH media for Co-PNP pincer and corrole-based systems respectively.

In the second chapter, we have designed OER catalysts by replacing Ca atoms with cost effective alkaline earths, main group elements and lanthanides to use the effect of electronic structure upon catalytic activity. The reason behind considering Mn-based catalysts is their efficiency in natural photosynthesis systems and also Mn based double perovskites have emerged as efficient catalysts for the OER. We have calculated the theoretical overpotential for each case with varying % of dopants from 10 to 40 on the surface in the alkaline media. In each case 30% doped systems are showing best behaviour and to find out the electronic picture behind it we have plotted projected density of states and found positions of e_g level with respect to Fermi level and covalency are affecting overall activity. Linear regression based model using four electronic structure based descriptors is proposed. This study suggests $Ce_{0.7}Ca_{1.3}Mn_2O_5$ as a best catalyst with overpotential value of 0.14 V.

In the third chapter, we have tried to answer some crucial questions asked by experimental observations. Like Na-analogue, $K_2CoP_2O_7$, a new pyrophosphate material was first time used to check its bifunctional characteristics and found to exhibit better catalytic properties than $Na_2CoP_2O_7$. In order to understand the reason behind, we have done the theoretical modelling which begins with a precise choice of active surface, followed by reaction modelling in the alkaline medium. Our calculation suggests [110] surface to be the active one for both OER and ORR and the coordination of Co-centre is playing a crucial role behind the high activ-

ity. It has been observed that during the reaction the tetra-coordinate Co centre effectively remains so. Interestingly, with the approach of reactant or during the formation of the intermediates one of the four bonded O from the bulk side moves away from Co-centre resulting in it effectively tri-coordinate. Pyrophosphate, having a strong P-O bond helps in showing such flexibility without deformation of overall structure.

In the fourth chapter, we have studied the bifunctionality of the experimentally synthesized class of fluorophosphates, Na_2MPO_4F (M=Mn, Co, Fe). In both cases, Na_2CoPO_4F was found to exhibit superior catalytic performance and Na_2FePO_4F to show the lowest one. Our theoretical calculation suggests the same observation except with Mn-analogue which has been found to show similar activity with Na_2CoPO_4F for OER theoretically but shows lower activity experimentally. Also, the post-ORR TEM suggests the degradation of Na_2FePO_4F which is also observed theoretically.

In the fifth chapter, we have modeled a CoN_4 doped carbon nanotube structure based on its hydrogen evolution reactivity. Experimentally Maji et. al. have synthesized the above mentioned system from a Co-MOF and they have varied N weight %. The XPS analysis suggests the presence of the peak of metallic Co, graphitic N and Co-N4 bonds. Keeping these experimental observations in mind, we modelled only with CoN_4 doped in CNT, followed by considering Co single atom and then a Co_4 cluster encapsulated in the nanotube, with a gradual increase of the N weight % from 3.08% to 7.66% with the variance of 1.52% . Since the reaction is carried out in the acidic medium, for HER we have considered free energy adsorption of H* intermediate on all possible sites and found out the active one. From our calculation, we have concluded that concentration of N-doping is playing a crucial role in enhancing the overall activity rather than encapsulated Co-atom or Co_4-cluster. The HER activity matches well with the experimental observation at N-weight % of 7.66 with N-centre to be the active site.

In the sixth chapter, we have tried to answer a question aroused by a few experimental observations. PNP-pincer complexes with secondary N-center are found to perform better than its tertiary analogue in many reactions, like hydrogenation of nitrile, CO_2, ketones etc due to presence of metal ligand cooperativity (MLC). But in 2015, Bernskoetter's group experimentally found just an opposite behaviour of Fe(II) carbonyl hydride for the hydrogenation of CO_2. The observation continues for Fe-centre with different ancillary ligands (including isonitrile and carbon monoxide) even for Co(I)-PNP pincer complex making them asking a question on benefits of presence of MLC. To find out the actual reason behind, we have done a detailed kinetic analysis of all possible reaction pathways in the presence and absence of an external base for Co(I)-PNP pincer complex with secondary (1a) and tertiary (1b) N and found hydride transfer to be the bottleneck of the reaction in each pathway. The MLC plays a crucial role in sigma complex (catalyst-H_2 adduct) splitting, so this phenomena can not poison the overall reaction mechanism and anyway in this case we are finding this to be favorable for both complexes. There are two reasons behind the huge difference in the turnover number, first is both the structure opens up on the approach of the reactants towards the Co-center causing a strain which is calculated in terms of distortion energies, which is higher for 1a. And second reason is, after removal of proton on N-center in 1a (which is highly possible in the presence of an external base), it forms a stable adduct with CO_2 resulting in a resting state. So our calculation suggests that bifunctionality is not functioning as a catalytic poisoning step.

In the seventh chapter, we report the study of the effect of electron density on CO_2 reduction in the neutral medium and its selectivity for the product, HCOOH vs CO. We have considered Ni(II)-corrole, boracorrole and phosphacorrole as catalysts and studied all possible pathways for the reduction of CO_2 thermodynamically. Interestingly, boracorrole and phosphacorrole, which have an unpaired electron, are able to adsorb CO_2 while corrole is not able to do so. We have considered

the whole pathway after single electron reduction as well and observed phospha-corrole is showing better results. We have considered concerted proton-electron transfer and found HCOOH to be the thermodynamically favourable product for all three systems.

Finally, in the eighth chapter, which is actually the conclusion and outlook chapter, we give a summary of all the chapters and their contributions toward green sustainable energy. Since we have worked on both hetero- and homogeneous catalysis, we are planning to design a heterogenized molecular catalyst which will have high selectivity like homogeneous catalysis and can directly be used as electrode.

List of publications

1. "Tailoring $Ca_2Mn_2O_5$ Based Perovskites for Improved Oxygen Evolution Reaction", **Neha Bothra**, Sandhya Rai and Swapan K. Pati, ACS Applied Energy Materials 1(11), (2018): 6312-6319.

2. "MOF Derived Co_3O_4@ Co/NCNT Nanocomposite for Electrochemical Hydrogen Evolution, Flexible Zinc-Air Batteries, and Overall Water Splitting", Tarandeep Singh, Chayanika Das, **Neha Bothra**, Nivedita Sikdar, Shubhajit Das, Swapan K. Pati, and Tapas Kumar Maji. Inorganic Chemistry 59(5), (2020): 3160-3170.

3. "Metal fluorophosphate polyanionic insertion hosts as efficient bifunctional electrocatalysts for oxygen evolution and reduction reactions",. Lalit Sharma, **Neha Bothra**, Rajeev Kumar Rai, Swapan Pati, and Prabeer Barpanda. Journal of Materials Chemistry A 8(36), (2020): 18651-18658.

4. "Potassium Cobalt Pyrophosphate $K_2CoP_2O_7$: as a Nonprecious and Efficient Bifunctional Electrocatalyst for Metal-Air Battery", Krishnakanth Sada, Ritambara Gond, **Neha Bothra**, Swapan K. Pati and Prabeer Barpanda. Manuscript under preparation.

5. Explaining the deleterious impact of secondary *versus* tertiary Nitrogen center on PNP-pincer Co(I)-complexes for hydrogenation of CO_2[†]. **Neha Bothra**, Shubhajit Das, Swapan K Pati. Manuscript under preparation.

6. Electrocatalytic Reduction of CO_2 on Ni-Corrole Based Systems. **Neha Bothra**, Supriti Dutta, Swapan K Pati. Manuscript under preparation.

Contents

List of Figures

1 Introduction

1.0.1 Environment & Energy

Any human endeavour has energy as an inevitable part, varying in form, source, or function. A report suggesting traces of Britain's coal 300 million years ago is proof that we are using different forms of fossil fuels-from solid (coal) to liquid (oil) to gas (natural gas)-as energy sources from the very beginning. Parallelly, the demand of these fuels increases tremendously with the quality of life. Amenities escorted by fossil fuels have fetched us into the industrial, and then to the information era. These incredible energy sources have paved way for innumerable tools and technologies that shape our world today as is evident from figure 1.1. According to British Petroleum statistical review of world energy, consumption of natural gas, global oil and coal has increased by 3%, 1.8% and 1% respectively.

Furthermore, the processes involved in the extraction, transportation, and processing of fossil fuels as well as the medium of use have left tremendous detrimental impacts on the world economy; both directly and indirectly. Coal excavation in many places is banned due to many reasons; spills and leakages are common phenomenon during withdrawal, carrying and storage of oil and gas results in water and air pollution. Irrespective of the processes (heating, electricity production

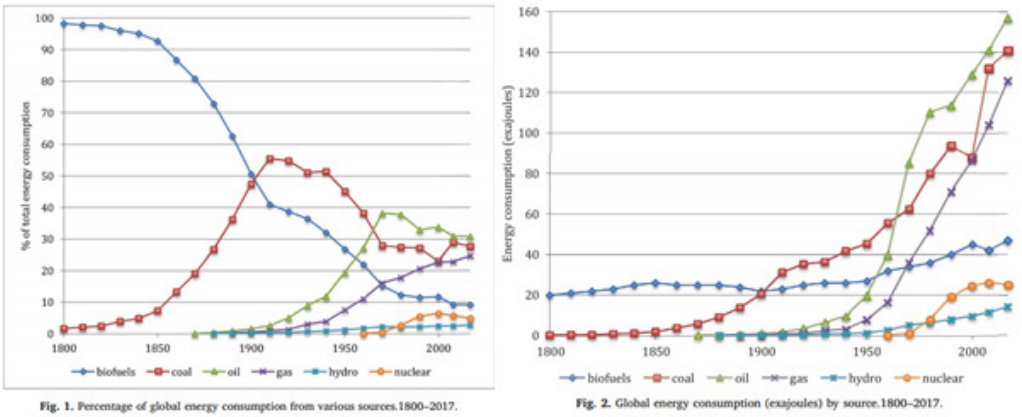

Figure 1.1: Taken from Ref. [1]

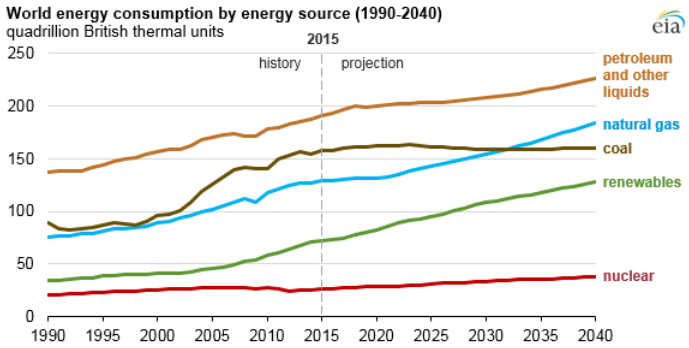

Figure 1.2: Growth in energy consumption by 28 % between 2015 and 2040. Taken from Ref. [1]

etc), the use of fossil fuels is always combustion. Carbon and hydrogen are primary components of these fuels along with a few other elements which were either present from the beginning or were added during refinement, hence, most often, the byproducts are various gases (CH, CO_x, SO_x, NO_x), droplets of tar, soot, ash, and other organic compounds; all of these cause air pollution and soil pollution. Many studies have shown that through chemical reactions, these primary pollutants might be converted to secondary pollutants, like aerosol, ozone, peroxyacyl nitrates, various acids, etc causing acid rain (which disturbs the whole terrestrial and aquatic ecosystems) or ozone layer depletion (allowing ultra-violet ray to enter the earth surface) and many other adverse effects. The major by-products of these reactions are CO_2, CH_4, N_2O, $CHCl_3$. These are collectively known as greenhouse

gases, which maintain an optimum temperature on earth, but when present in excess cause rise of sea level, melting of ice caps, change in climate, leading to what is known as the 'greenhouse effect'.

Interestingly, over time in general one fossil fuel [2] continues to surpass another; in nineteenth-century, coal overtook biomass as the biggest global energy supplier, but it was overthrown by petroleum in the 20th century, petroleum became as big energy suppliers as coal. The limited quantities of these fuels pose a concern as the demand increases rapidly with the world population and economic growth in developing countries. Statistics tells us that with the current consumption rates, we will run out of oil and gas in 20-30 years, and coal by 68 years.

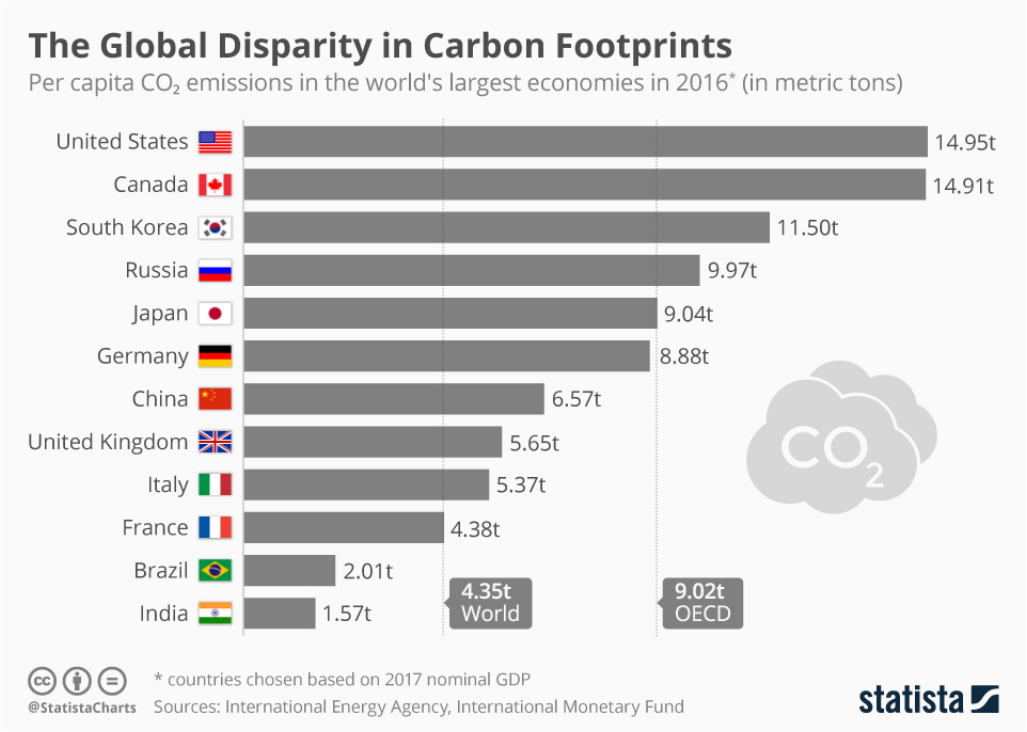

Figure 1.3: CO_2 emission in different countries (https://www.nature.com/articles/d41586-017-07507-y)

1.0.2 Status of Renewable Energy Resources

The severity of the threat posed by fast depleting fossil fuels and anthropogenic environmental issues have demanded sustainable and environmentally benign energy resources, particularly the low-carbon energy sources, which can serve the needs of daily life. Renewable energy sources have come up as a promising remedy for the last few decades and a "transition from fossil fuels" is becoming prominent gradually as mentioned in a special supplement of the Nature journal by Michelle Grayson[3], who says "The transition from fossil fuels is well underway. Each year sees an increase in the amount of electricity generated from renewable sources. . . ." Commonly known renewable energy sources are hydropower, biomass, geothermal, solar tidal, wind, hydrogen energy. However, there are several issues like engineering practicality, applicability, reliability, economy, scarcity of supply, public awareness and acceptability. With time, different groups have come up with new and revised strategies on the improvement of renewable energy techniques. At the strategic level, it is suggested that researchers should either keep the CO_2 level under checked or provide a permanent solution for scarcity of fossil fuels by reducing the pollution. Hoffert et. al.[4] have focused on the partially renewable nuclear energy, sequestering carbon and decarbonizing fossil fuels. Pacala and Socolow[5] emphasized on the usage of hydrogen in vehicles. Depending on geographical location and economic viability, Fthenakis et. al.[6] has proposed improved technical overview for solar energy in United States of America. The ultimate goal is to provide the design, such that, it can avail 100% renewable energies and more than 180 articles have been published over the last 15 years as mentioned in a review article in 2019[7]. There have been additional strategies as well, for instance, Nordic cooperation[8], which covers sovereign states of Denmark, Finland, Iceland, Norway and Sweden's renewable energies and a few other places under the renewable electricity policy development. From 2011 to 2018, Fin-

land worked on wind, biogas[9], wood fuels and forest chips[10,11] related renewable electricity. Their target is to attain a complete renewable electricity production by 2040, whose partial completion is expected by 2020 followed by improvement within remaining years. Fig. 1.4 is taken from https://www.cleanenergywire.org/factsheets/power-gas-fix-all-problems-or-simply-too-expensive .

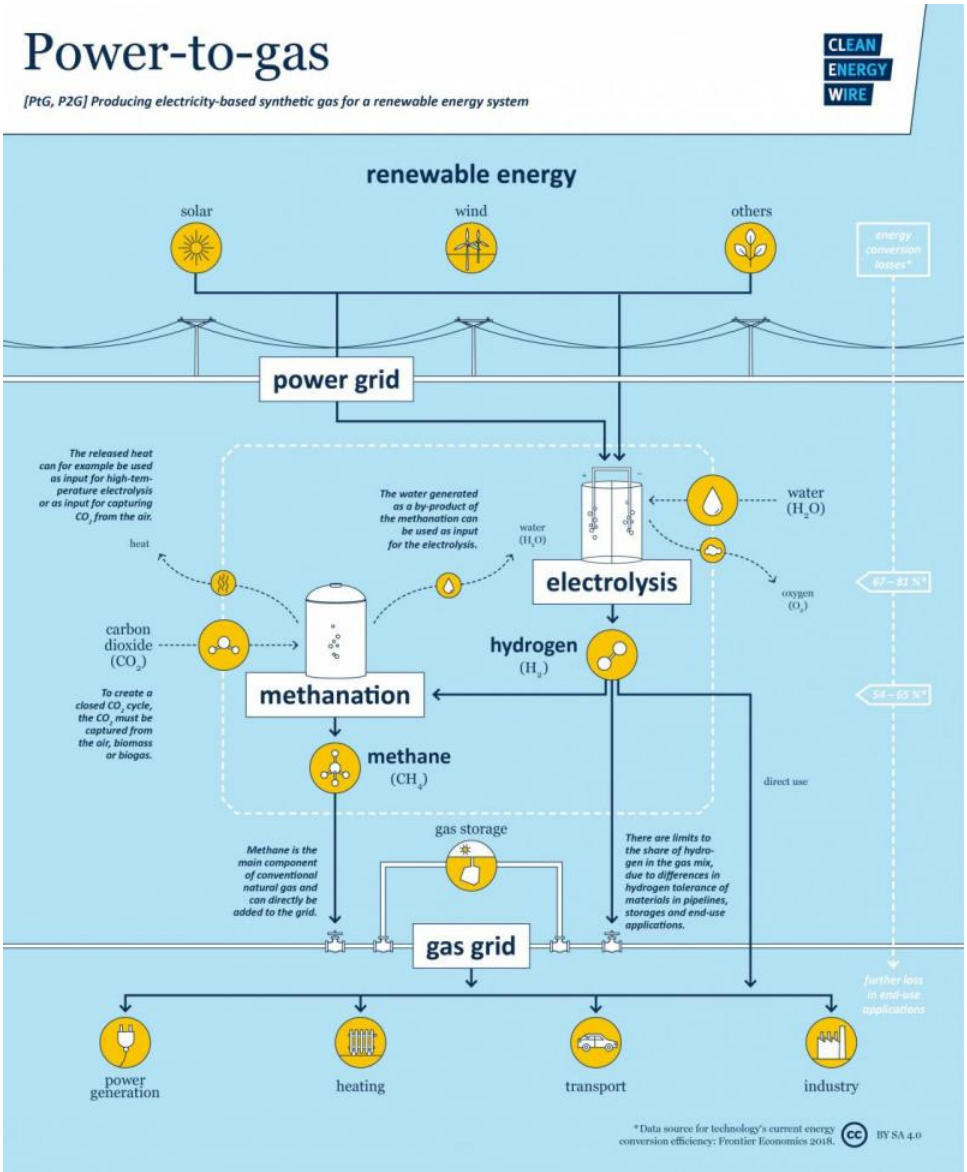

Figure 1.4: Power to Gas Process Chain.

Another project in Finland Neo-Carbon Energy (NCE) research project [12–14] in collaboration with Technical Research Centre of Finland VTT Ltd, Lappeenranta University of Technology LUT and Finland Futures Research Centre FFRC at University of Turku was initiated in 2014. It works in two parts [12], in first part, they focus on constructing an infrastructure for an emission-free sustainable energy system and how to incorporate those in the society. They call the method "neocarbonisation", which implies substituting fossil carbon and fuels with the products from CO_2, water and electricity. They have also focused on power-to-gas (P2G) technologies [15–17], which was first put forward in Japan [18] in the 1980-1990. Again the main motivation behind this has been to store electrical energy in terms of chemical energy, to produce CH_4 and H_2 gas from electricity, as shown in Fig. 1.6, which briefly gives an overview about how it functions. The electrolysis technologies like AEL (alkaline electrolysis) [19–21], PEMEL (proton exchange membrane electrolysis) [22] and SOEL (solid oxide electrolysis) [23–25] play the crucial role in overall process. In a review article in 2008 [26], Mark Z. Jacobson

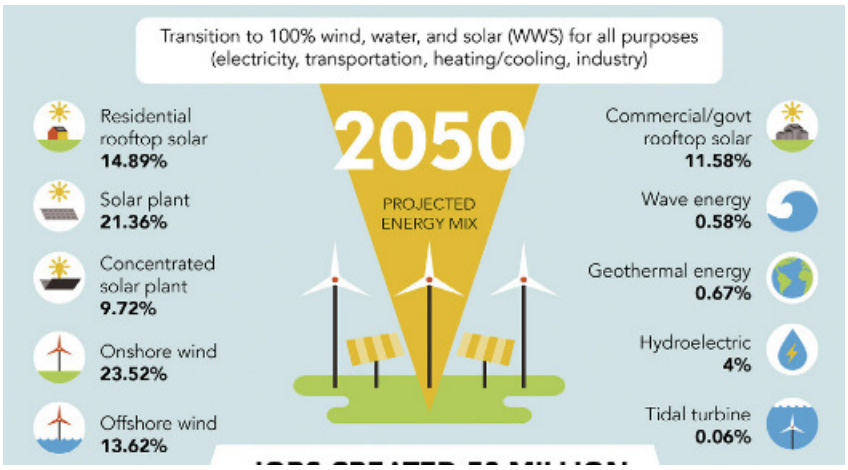

Figure 1.5: Projected energy consumption by 2050.

has provided an overview of nine electric power sources (solar-photovoltaic, CSP (concentrated solar power), geothermal, wind, wave, hydroelectric, nuclear and coal with CCS (carbon capture storage)) and two liquid fuel options (cellulosic

E85, corn 85) applied on the three vehicles (HFCVs, BEVs and E85). The review concludes that coal-CCS and nuclear energy provides comparatively greater negative impacts than the overall benefits. Similarly, biofuel exhibits rather significant demerits with no particular benefits. Later on, along with his colleagues, the author designed roadmaps to cover all aspects of energy infrastructures (transportation, agriculture/fishing/forestary, electricity, industry, cooling/heating etc)) which cover 139 countries powered by wind, water and sunlight (WWS). Jacobson and Delucchi first mentioned that this WWS based solution for global energy issues would be effective in 2011 in two parts. Part I[27] focuses on the obtainability of the WWS resources, energy demand, nature and number of WWS energy systems and the geographical areas. Part II[28] discuss about the applicability of all these systems in larger scale in terms of variability, economics and policies needed for a worldwide infrastructure. In their review article, they have discussed about the practical issues of these renewable sources and suggested possible remedies. For instance, the solar and wind power vary constantly hence it does not match the demand pattern consistently; tidal power can be relied upon because of the predictability; power obtained from geothermal source is constant; hydroelectric power can be regulated with ease. Hence, depending on a single source may not be able to meet the demands or installing more than one renewable energy may lead to wastage of extra energy. Hence, they have come up with a solution in seven ways so that WWS energy systems would be reliable sources without any loss, which are: (i) interlinking geographically spread natural variable sources (e.g. solar, wind, tidal and wave), (ii) consider non-variable sources with variable one to meet the temporary gaps, (iii) smart techniques to shift flexible loads, (iv) store the extra electric power locally, (v) increasing the efficiency with respect to time and should be able to produce H_2 for flexible transport, (vi) storing electric power in electric-vehicle batteries, (vii) forecasting the weather. Later on, with another group of scientists, they have provided a roadmaps of WWF energy systems for

139 countries[29,30] of the world which has increased to 143 countries already.[31,32]

To make these renewable energies part of every day's lives it has to be affordable to each one. One of these methods is the electrochemical energy technology. The electrochemical method is the best method as there is nearly 100% conversion of the reactant to products. These electrochemical processes can be improved with the help of active, stable and cost-effective catalysts. In what follows we describe in brief the electrochemical conversions and catalysis.

Electrochemical Conversions

An electrochemical or galvanic cell consists of a pair of conducting substance (conductors or semiconductors), known as electrodes, immersed into ionically conducting and electronically linking electrolyte, which can be liquid or solid. The chemical reaction, oxidation in anode and reduction in cathode, leads to generation of electricity in the outer circuit and ionic current which flows in the form of ions in electrolyte. Fig 1.6 is a picture of a typical electrochemical cell.

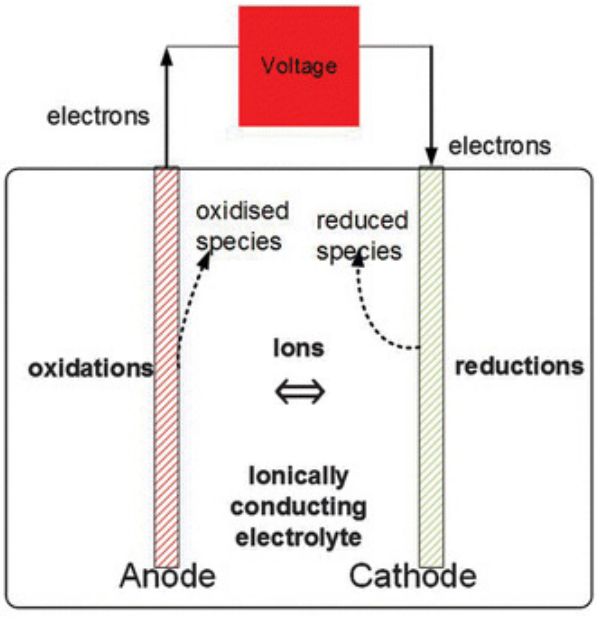

Figure 1.6: An electrochemical cell. Taken from ref[33]

Another type of cell which requires external electric energy for a chemical reaction is called electrolysis cell. Examples of galvanic cells are fuel cells or batteries, whose reactivity can be improved by improving the catalytic activities of the electrodes.

1.0.3 Catalysis

The term, catalyst was first coined in 1836 by Swedish scientist, Jons Jakob Berzelius and since then this has been used extensively in different processes worldwide.The definition for catalyst and catalysis by IUPAC is given as, 'A substance that increases the rate of a reaction without modifying the overall standard Gibbs energy in the reaction; the process is called catalysis'. The steady growth in this field resulted in the current scenarios where 95% chemical production will pass through at least one catalytic step. Along with playing a role in enhancing the activities, catalyst can also modify the product selectivity by controlling the kinetic pathways.

The coherence of phases in the catalytic processes has been broadly divided into two categories: (i) homogeneous catalysis, where both the catalyst and substrate are in same phase, in general liquid phase; (ii) heterogeneous catalysis is when the catalysts are in the solid phases and the reactant are in the gas phase. Both of these catalytic processes have certain advantages and certain disadvantages along with distinctive catalytic pathways. In general, metal ions, Bronsted and Lewis acids/bases, enzymes etc fall under homogeneous catalysis category; both reactants and catalysts being in the same phase interact more conveniently whereas in case of heterogeneous catalysts, the reactants have to get adsorbed on the active site or surface to continue further reaction and finally the product has to be desorbed out of the site or surface to avoid catalytic poisoning. This is shown in pictorial diagram (Fig. 1.7).

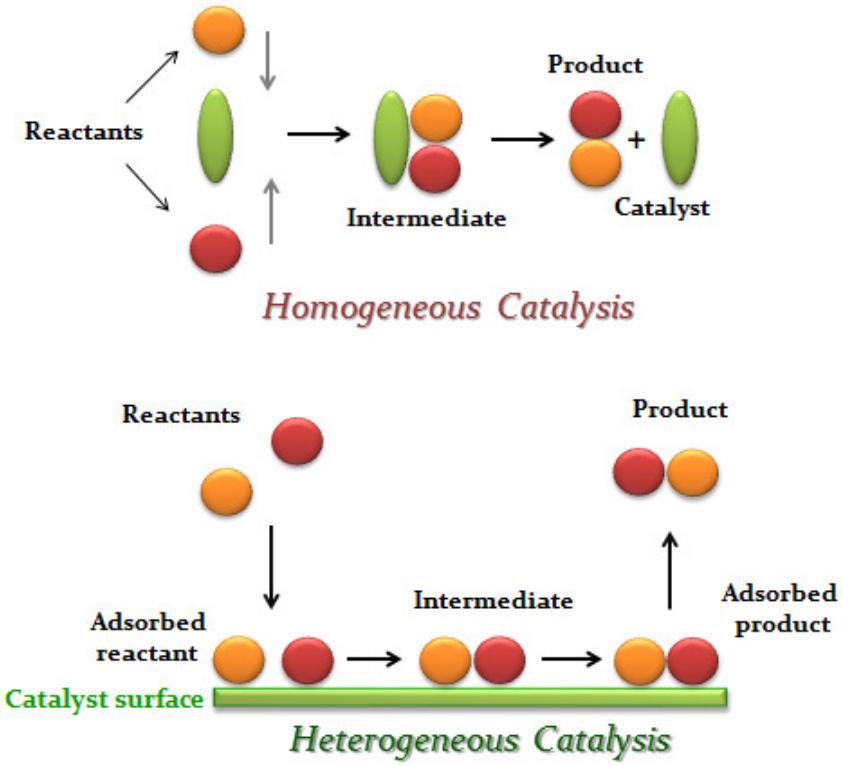

Figure 1.7: Catalytic pathway of homogeneous and heterogeneous catalysis

The pros and cons of both the processes are mentioned in the table below:

Most basic and important among all the catalytic reactions is the one, where water splits into hydrogen and oxygen molecules in two catalytic reactions.

Homogeneous catalysts	**Heterogeneous catalysts**
more selective	less selective
difficult to extract products	easy to extract products
high adaptibility	low adaptibility
lesser thermal (T) and pressure (P) stability	stable at high T, P
higher reproducibility	lower reproducibility

Water splitting Reaction

In the current technology driven world, the fuel cell is used for multipurpose reasons, starting from conventional power supplier to the usage as a fuel in transportation sector. There are broadly two ways to generate the constituent elements, electrochemical and photochemical. Photochemical pathway often leads to a mixture of products due to the difficulties in controlling the rate of the exposure of photo-radiation to access various ground and excited states. In fact, this may be the case in other conversion too but it can be controlled by the wise choice of active sites. Electrochemical water splitting is able to cover this issue, however, the sluggish kinetics of the anode reaction has constrained the supply of H_2 up to 4% only[34]. Another most popular approach is steam reformation to produce H_2 and CO_2[35], however, splitting of water is preferable as it is the reverse reaction of fuel cell and hence the whole pathway promotes a zero carbon emission process. Large number of experimental and theoretical studies have been conducted to obtain environmentally benign, industrially viable, stable and active catalysts to split water. Industrially used catalysts comprises of costly rare metals (4d-5d transition metals). Trasatti and Buzzanca[36] first time used RuO_2 as an electrode for OER in alkaline medium in 1971, which was followed by further studies to improve its reactivity and found [110] surface to be the most active one[37]. In the late 1970's, another group[38] had synthesized IrO_2, which is proven to be another active catalyst for OER with higher stability. Pt electrodes are also found to show good OER activity in alkaline media due to high exchange current density, first reported by Birss et al.[39,40] in 1980s. The key characteristics considered while designing these OER catalysts are a relatively high electronic conductivity and a high affinity to adsorb mainly *OH and sometimes *OOH intermediates. Pt-based catalysts show good results also for ORR in the acidic media[41] and have been used in various places on a large scale. So, these expensive catalysts have intrigued to

find catalysts with good efficiency and low cost, over the last many years. Different kinds of oxides, carbides, metal alloys, clusters, two-dimensional (2d) systems etc have been studied and the search is still on. A detailed mechanistic pathway has also been identified to improve the catalytic activity. And it has been found that, OER in both acidic and alkaline medium is comprised of four steps sharing the same intermediates as shown in the schematic diagram. However, in case of ORR, it can follow either inner-sphere mechanism involving $4e^-$ leading to H_2O or outer-sphere mechanism with $2e^-$ pathway to peroxide in both acidic or alkaline medium. The first one is the favourable one in most of the cases as it leads to thermodynamically stable and favorable pathway.

1.0.4 CO_2 reduction

Amidst the current focus on improving the activity of different renewable green energy sources, the effect of green house gases due to their constantly increasing concentration calls for an immediate attention. A requisite step in this direction is a continuous elevation of excessively generated CO_2 (one of the main member of the green house gases) as a by-product, via chemical conversions to some other useful composition and thus maintaining low concentration in the atmosphere. Currently, the global average concentration of CO_2 is 409.8 parts per million (ppm for short) or 0.04% (according to the survey in 2019), which is around 47% higher than its usual concentration before the Industrial age. In spite of being present in trace amount, CO_2 has always been an integral part in the life-cycle of living beings, thus creating a balance. But as CO_2 is capable of adsorbing and radiating heat, it results in global warming.

1.0.5 Theoretical formulation

The theoretical calculations of both homogeneous and heterogeneous catalytic processes are based upon density functional theory (DFT) based ab-initio methods. A brief overview of DFT based approaches and the background will give the reasoning behind choosing this particular method.

Electronic structure calculations

In quantum mechanics, all kind of characteristics of a system is stored in the corresponding wave function. Electronic information like energy, momentum etc can be derived with the help of corresponding operators from this wave function. It is denoted by a symbol Ψ, and written as $\Psi = \Psi(\mathrm{R,r})$, where R and r represent the summarized spin and spatial coordinates of nuclei and electron respectively. The energy of each system can be obtained by applying Hamiltonian operator ($\hat{H}$) on Ψ(R,r) and the equation is widely known as Schrödinger equation,

$$\hat{H}\Psi(R,r) = E\Psi(R,r) \tag{1.1}$$

$$\hat{H} = -\frac{1}{2}\sum_{i=1}^{N}\nabla_i^2 - \sum_{k=1}^{L}\frac{1}{2M_k}\nabla_k^2 - \sum_{i=1}^{N}\sum_{k=1}^{K}\frac{Z_k}{|r_i - R_k|} + \frac{1}{2}\sum_{i\neq j}^{N}\frac{1}{|r_i - r_j|} + \frac{1}{2}\sum_{k\neq 1}^{K}\frac{Z_k Z_I}{|R_k - R_I|} \tag{1.2}$$

$$\hat{H} = \hat{T_e} + \hat{T_n} + \hat{V_{en}} + \hat{V_{ee}} + \hat{V_{nn}} \tag{1.3}$$

In the above equation, the first term is the kinetic energy of N number of electrons, second term is kinetic energy of L number of nuclei, third, fourth and fifth terms are the potential energies corresponding to nuclei-electron, electron-electron, nuclei-nuclei interactions respectively.

Born-Oppenheimer Approximation

Born-Oppenheimer approximation, also familiar as an adiabatic approximation, allows to decouple the dynamics of nuclei and electrons because the nuclei are almost 2000 times heavier than the electrons, so it can be assumed that nuclei remain static with respect to electrons movement. Hence time-independent Schrödinger equation (SE) can be written for electronic degrees of freedom in the presence of stationary nuclear part. The modified electronic Hamiltonian is,

$$\hat{H}_e = \hat{T}_e + \hat{V_{en}} + \hat{V_{ee}} \tag{1.4}$$

Over a period of time, various approaches with compatible approximations have been considered to solve the SE, which include Hartree-Fock (HF), configuration interaction (CI), coupled cluster, Moller-Plesset perturbation theory, to name a few. Apart from HF theory, other methods are all wave-function based approach. Though these methods provide better results, the latter approaches demand high computational power.

Density Functional Theory

Density functional theory based method is a different approach to solve the SE, which replaces wave function with the electron density of the system to obtain the ground state electronic properties. This method was first proposed in 1960s in two seminar papers by Hohenberg-Kohn.[42] Later in two subsequent years, whose idea was mainly based upon Thomas-Fermi model. This *ab initio* (first principles) based method has gradually drawn attention as it is capable of mapping a complicated interacting problem to an easier non-interacting problem with replacement of the number of degrees of freedom, 3N (N is number of quantum particles) to only 3 spatial coordinates.

Hohenberg-Kohn Theory

This is based upon two theorems,

Theorem-I [Uniqueness]: "For any system of interacting particles in the presence of an external potential $V_{ext}(r)$, the potential $V_{ext}(r)$ can be uniquely determined, upto an additive constant, by the ground state density $n_0(r)$." In other words, the total ground state energy of a system is a unique functional of its density, E[n(r)], hence we can write:

$$E[n(r)] = \langle \Psi[n(r)]|H|\Psi[n(r)]\rangle \tag{1.5}$$

Theorem-II [Variational Theory]: "A functional which is universal for the energy E[n] in terms of density n(r) can be defined, valid for any external potential $V_{ext}(r)$. For any particular $V_{ext}(r)$, the exact ground state energy of the system defines the global minimum value for this functional, and the density which minimizes the functional is the exact ground state density $n_0(r)$". The energy can be expressed as a sum of kinetic energy part (T[$n(r)$]), electrostatic energy part (U[$n(r)$]) and energy due to non-interacting electrons moving under external potential:

$$E[n(r)] = T[n(r)] + U[n(r)] + \int [V(\vec{r})n(\vec{r})d^3r] \tag{1.6}$$

Here the first two terms are independent of external potential and can be written in the form of universal functional of the electron density:

$$T = \int \frac{3}{10}[3\pi^2 n(r)]^{\frac{2}{3}} n(r)dr \tag{1.7}$$

$$U = \frac{1}{2}\int \frac{n(r)}{|r-r'|}dr'dr \tag{1.8}$$

The expression of kinetic energy is however inaccurate and moreover, the deduction of the functional of the interacting systems is not very clear. This is solved by Kohn-Sham approach, where they have proposed an indirect approximate approach to calculate energy functional E[n(r)].

Kohn-Sham Equations:

Kohn and Sham considered a uniform electron density from 3d non-interacting electron gas and iteratively solved the Kohn-Sham equation. They considered, as a first approximation, fictitious system of non-interacting electrons instead of a real system of interacting electrons having the same electron density. This theorem is enabled to calculate energy and other electronic properties of only the ground state. Having the same electron density leads to same ground state energies and other electronic properties. Since electrons are not affecting each other, Kohn-Sham equation can be considered as a set of single particle equations, which are simpler to handle than coupled Schrödinger equation, which gets more complicated with the increase of system size and hence number of electrons. The interacting part of the energies has been taken care of in terms of exchange-correlation and energy is written in terms of density:

$$E_{[\mathrm{n(r)}]} = T_{[\mathrm{n(r)}]} + E_{\mathrm{ext}[\mathrm{n(r)}]} + \frac{1}{2}\int \frac{n(r)}{|r - r'|} + v_{\mathrm{xc}[\mathrm{n(r)}]} \tag{1.9}$$

In the above equation, the first term is the kinetic energy of only non-interacting electrons, the second term is classical Coulomb interaction between nuclei and electron, third term is classical electron-electron interactions also known as Hartree interaction, the final term is exchange-correlation including the non-classical electrostatic interaction energy between electrons and the difference of energy between non-interacting and interacting kinetic energy of electron. The main idea behind this approach is that the first three terms can be dealt with simply and last term

can be modified with better approximations.

Exchange-Correlation Functionals:

The exchange-correlation functionals include two different kinds of electronic interactions; the exchange part comes because of fermionic nature of the electrons. The antisymmetrically paired electrons exchange with each other following Pauli exclusion principle. The other term i.e. correlation term is arising because of the effect of other electrons on kinetic and potential energy. The exact form of each interaction is still unknown, hence the mathematical expressions have been provided for both the terms. Hartree-Fock method was able to provide an exact form of exchange energy but it has not included correlation energy at all. Since the accuracy of calculation depends on the exchange-correlation functionals, various modifications have been done over time.

Local density approximation: LDA is the simplest approximation, where the exchange-correlation term can be expressed as a function of homogeneous electron gas i.e. uniform electron density.

$$E_{ex(n)}^{LDA} = \int e_{\mathrm{xc}}(n(r)n(r)dr \tag{1.10}$$

The mathematical form of exchange and correlation energy is:

$$e_{\mathrm{x}}(n) = -\frac{0.458}{r_{\mathrm{s}}} \tag{1.11}$$

$$e_{\mathrm{c}}(n) = -\frac{0.44}{r_{\mathrm{s}} + 7.8} \tag{1.12}$$

$\mathrm{r_s}$ is the radius of a sphere containing one electron. The correlation energy is deduced by quantum Monte-Carlo simulations, most commonly used one was proposed by Perdew and Zunger.[43] Inspite of being an extensive crude approxima-

tion, it works well for solid systems close to a homogeneous gas and explain a few physical properties like lattice parameters, vibrational frequencies, equilibrium geometries properly. However, it overestimates the binding energies and does not work well for inhomogeneous systems.

Generalized gradient approximation: To account for inhomogeniety of the system, GGA has modified LDA by including the gradient expansion term:

$$E_{\mathrm{ex(n)}} = \int e_{\mathrm{xc}}(n(r), |\partial n(r)|) n(r) dr \tag{1.13}$$

There are several approaches which can be included within GGA calculations, the commonly used ones are PBE[44,45], RPBE[46] and PW91[47]. The choice of functional is dependent upon the characteristics of the system. It has a tendency to underbind.

Several better modifications have been introduced to GGA resulting in meta-GGA, hybrid functionals. This functionals have been modified by considering both the electronic density and individual electronic wavefunctions to compute the energy and other properties.

Basis set and Pseudopotential

To do the calculations, the Kohn-Sham (KS) orbitals have to be expanded based on the nature of systems to solve the KS equation, like plane wave function[48] is used for periodic systems. According to Bloch's theorem, electron's wavefunction can be expressed as a product of plane wave and function correspond to the periodic lattice system:

$$\Psi_{\mathrm{nk}}(r) = e^{\mathrm{ik.r}} u^{\mathrm{nk}}(r) \tag{1.14}$$

here wave vector k is the crystal momentum vector, e Euler's number, i is the imaginary unit. In case of molecular systems, the KS-orbitals are expressed in

terms of Pople-basis sets.

It is well known that, the core electrons do not participate in the chemical reactions or have minimum role in exhibiting any physical or chemical properties; moreover since they are tightly bound and highly localized in nature hence all electron calculations are highly costly to calculate. The concept of pseudopotential approximation has arrived to deduct this computational cost by eliminating the core states calculations. Here instead of strong ionic potentials a weaker pseudo potentials which is a pseudo wavefunction of valence electrons only has been considered. The oscillation of valence electrons in the core region has not been taken into account, a pseudo wavefunction of the valence electrons has replaced the strong ionic potentials. There is a critical distance after nuclei, named as 'cut-off' radius beyond which the pseudo-wave function compares fairly well with the actual one. If this cut-off is high, then the pseudo potential are called softer. The nature of PP approximation depends on its smoothness and transferability properties. There are three types of PP - norm-conserving, ultra-soft and projector-augmented wave.

Finding a transition state:

We discuss here about transition structure followed by finding a transition state in a reaction. A transition structure is the one separating the reactant and product and it stays at the peak of potential energy function with a single degree of freedom. The energy corresponding to transition state is widely known as 'activation energy', which is an important parameter to determine the kinetic fate of a reaction. In terms of mathematical expression, the transition structure is defined as a 'saddle point' on the multi-dimensional molecular potential energy surface. It is a first-order saddle point, where the local maximum is only along the reaction path and local minimum along all other directions. At this point, the first and second derivative of potential with respect to any nuclear coordinate is zero and

positive respectively. Interestingly, it is a local minima along all direction but local maxima along the reaction path. There are few ways in finding the transition states[49] of a molecular reaction in Gaussian software; for example it can be searched with the help of algorithm after providing the structure of reactant and product or scanning the coordinates of reactant or product carefully based upon chemical intuition. Any of these ways are not the trivial one; after optimizing the transition structure, it is connected with the reactant and product with the help of intrinsic reaction coordinate[50].

1.0.6 Softwares used:

To obtain the reported results in this thesis several packages have been used. We have considered both heterogeneous and homogeneous systems; all the electronic structure calculations were carried out with DFT method; geometry optimization, thermodynamic calculations, vibrational frequency analyses, solvent corrections were carried out using Quantum espresso and Gaussian package (releases G16 A.03). The Bader charge analysis has helped for charge analysis of periodic systems and NBO 3.1 package featured as a part of Gaussian programs for bonding analysis. The structures are constructed, visualized and analysed with the help of Gaussview, VESTA, VMD, Xmgrace.

1.0.7 Scope of the thesis

The thesis commences with the study of doping effect on oxygen evolution reactivity of Oxygen deficient double perovskite, $Ca_2Mn_2O_5$ framework and based on these, we have modelled a structure-activity based framework. In chapter 3 and 4, we have been able to find the reason behind bifunctional behaviour i.e. showing both oxygen evolution and oxygen reduction reactions of experimentally synthesized $K_2CoP_2O_7$ and Na_2MPO_4F (M=Mn, Co, Fe) respectively. In chapter

5, we have carried out modelling studies on N-doped carbon nanotube with Co-N_4 system with the help of its experimentally observed hydrogen evolution reactivity. Chapter 6 answers the underlying reason behind huge difference between turn over number (TON) of same pair of Co-PNP pincer complex; one with secondary and another with tertiary N-center through extensive modelling. Chapter 7 deals with the effect of electron density on CO_2 reduction by corrole-based systems. Chapter 8 provides a final conclusion and future outlook. While the work chapters, 2, 6 and 7 are solely based on theoretical modelling, the work chapters, 3, 4 and 5 are in collaboration with experimental observations, which we have explained explicitly with microscopic understandings.

References

[1] U. E. I. Administration, *International Energy Outlook*, 2017.

[2] A. Grübler, N. Nakićenović and D. G. Victor, *Energy policy*, 1999, **27**, 247–280.

[3] M. Grayson, *Nature*, 2017, **s133**, 551.

[4] M. I. Hoffert, K. Caldeira, G. Benford, D. R. Criswell, C. Green, H. Herzog, A. K. Jain, H. S. Kheshgi, K. S. Lackner, J. S. Lewis *et al.*, *Science*, 2002, **298**, 981–987.

[5] S. Pacala and R. Socolow, *Science*, 2004, **305**, 968–972.

[6] V. Fthenakis, J. E. Mason and K. Zweibel, *Energy Policy*, 2009, **37**, 387–399.

[7] K. Hansen, C. Breyer and H. Lund, *Energy*, 2019, **175**, 471–480.

[8] S. Kilpeläinen, *Politics and Governance*, 2020, **8**, 375–383.

[9] M. Gustavsson, E. Särnholm, P. Stigson and L. Zetterberg, *Swedish Environmental Research Institute, Gothenburg*, 2011.

[10] G. Egnell, *Forest Ecology and Management*, 2011, **261**, 148–153.

[11] J.-O. Dalenbäck, U. Pettersson and T. Persson, ESTEC 2011-5th European Solar Thermal Energy Conference, Marseille, France, 20-21 October, 2011, 2011.

[12] S. Heinonen, J. Karjalainen and J. Ruotsalainen, *Neo-Carbon Energy Working Paper*, 2016, **1**, 2016.

[13] S. Heinonen, S. Honkapuro, J. Karjalainen, T. Koljonen, J. Ruotsalainen and L. Similä, *https://cris.vtt.fi/en/publications/final-neo-carbon-energy-countdown-ready-for-renewables*, 2017.

[14] M. Lang, J. Karjalainen and S. Heinonen, *Neo-Carbon Energy WP1 Working Paper*, 2016, **4**, 2016.

[15] E. Pursiheimo, H. Holttinen and T. Koljonen, *IET Renewable Power Generation*, 2017, **11**, 1695–1706.

[16] C. Breyer, E. Tsupari, V. Tikka and P. Vainikka, *Energy Procedia*, 2015, **73**, 182–189.

[17] M. Götz, J. Lefebvre, F. Mörs, A. M. Koch, F. Graf, S. Bajohr, R. Reimert and T. Kolb, *Renewable Energy*, 2016, **85**, 1371–1390.

[18] K. Hashimoto, M. Yamasaki, K. Fujimura, T. Matsui, K. Izumiya, M. Komori, A. El-Moneim, E. Akiyama, H. Habazaki, N. Kumagai *et al.*, *Materials Science and Engineering: A*, 1999, **267**, 200–206.

[19] L. Bertuccioli, A. Chan, D. Hart, F. Lehner, B. Madden and E. Standen, *Fuel cells and hydrogen joint undertaking*, 2014.

[20] A. Ursua, L. M. Gandia and P. Sanchis, *Proceedings of the IEEE*, 2011, **100**, 410–426.

[21] K. Zeng and D. Zhang, *Progress in energy and combustion Science*, 2010, **36**, 307–326.

[22] M. Carmo, D. L. Fritz, J. Mergel and D. Stolten, *International Journal of Hydrogen Energy*, 2013, **38**, 4901–4934.

[23] J. B. Hansen, *Faraday Discussions*, 2015, **182**, 9–48.

[24] S. D. Ebbesen, S. H. Jensen, A. Hauch and M. B. Mogensen, *Chemical Reviews*, 2014, **114**, 10697–10734.

[25] M. Laguna-Bercero, *Journal of Power Sources*, 2012, **203**, 4–16.

[26] M. Z. Jacobson, *Energy & Environmental Science*, 2009, **2**, 148–173.

[27] M. Z. Jacobson and M. A. Delucchi, *Energy Policy*, 2011, **39**, 1154–1169.

[28] M. A. Delucchi and M. Z. Jacobson, *Energy Policy*, 2011, **39**, 1170–1190.

[29] M. Z. Jacobson, M. A. Delucchi, Z. A. Bauer, S. C. Goodman, W. E. Chapman, M. A. Cameron, C. Bozonnat, L. Chobadi, H. A. Clonts, P. Enevoldsen *et al.*, *Joule*, 2017, **1**, 108–121.

[30] M. Z. Jacobson, M. A. Delucchi, M. A. Cameron and B. V. Mathiesen, *Renewable Energy*, 2018, **123**, 236–248.

[31] M. Z. Jacobson, M. A. Delucchi, M. A. Cameron, S. J. Coughlin, C. A. Hay, I. P. Manogaran, Y. Shu and A.-K. von Krauland, *One Earth*, 2019, **1**, 449–463.

[32] M. Z. Jacobson, M. A. Delucchi, M. A. Cameron, S. J. Coughlin, C. A. Hay, I. P. Manogaran, Y. Shu and A.-K. von Krauland, *One Earth*, 2020, **2**, 109.

[33] K. Scott, *chapter 1, Energy and Environment Series*, 2019.

[34] J. Li and G. Zheng, *Advanced Science*, 2017, **4**, 1600380.

[35] C. G. Morales-Guio, L.-A. Stern and X. Hu, *Chemical Society Reviews*, 2014, **43**, 6555–6569.

[36] S. Trasatti and G. Buzzanca, *Journal of Electroanalytical Chemistry and Interfacial Electrochemistry*, 1971, **29**, A1–A5.

[37] P. Castelli, S. Trasatti, F. H. Pollak and W. E. O'Grady, *Journal of Electroanalytical Chemistry and Interfacial Electrochemistry*, 1986, **210**, 189–194.

[38] G. Beni, L. Schiavone, J. Shay, W. Dautremont-Smith and B. Schneider, *Nature*, 1979, **282**, 281–283.

[39] V. I. Birss, A. Damjanovic and P. Hudson, *Journal of The Electrochemical Society*, 1986, **133**, 1621.

[40] V. I. Birss and A. Damjanovic, *Journal of The Electrochemical Society*, 1987, **134**, 113.

[41] A. Damjanovic, D. Sepa and M. Vojnovic, *Electrochimica Acta*, 1979, **24**, 887–889.

[42] P. Hohenberg and W. Kohn, *Physical Review*, 1964, **136**, B864.

[43] J. P. Perdew and A. Zunger, *Physical Review B*, 1981, **23**, 5048.

[44] J. P. Perdew, K. Burke and M. Ernzerhof, *Physical Review Letters*, 1996, **77**, 3865.

[45] M. Ernzerhof and G. E. Scuseria, *The Journal of Chemical Physics*, 1999, **110**, 5029–5036.

[46] B. Hammer, L. B. Hansen and J. K. Nørskov, *Physical Review B*, 1999, **59**, 7413.

[47] Y. Wang and J. P. Perdew, *Physical Review B*, 1991, **44**, 13298.

[48] G. Kresse and J. Furthmüller, *Physical Review B*, 1996, **54**, 11169.

[49] C. Peng and H. Bernhard Schlegel, *Israel Journal of Chemistry*, 1993, **33**, 449–454.

[50] L. Deng and T. Ziegler, *International Journal of Quantum Chemistry*, 1994, **52**, 731–765.

2

Tailoring $Ca_2Mn_2O_5$ Based Perovskites for Improved Oxygen Evolution Reaction

2.1 Introduction

Increase in energy demands and growing concerns worldwide about the global warming have led to a surge in the discovery of economical and efficient catalysts that can be used for the electrochemical energy conversion processes, like oxygen evolution reaction (OER), oxygen reduction reaction (ORR) and hydrogen evolution reaction (HER).[1–6] However, the sluggish kinetics of the OER processes, demands for high overpotential compared to the other two, inhibiting its extensive use in generating green energies. This is also responsible for making it one of the most discussed and explored research areas.

Till date, rutile-type RuO_2 is considered to be the most efficient electrocatalyst for OER, which is used on industrial scale, followed by IrO_2 in acidic medium.[7] But, low abundance and high cost of the metals along with the tendency to get further oxidized hampers its usage in large scale industrial scale.[8–12] Another

goal of catalyst design is to propose catalysts that are sufficiently economical from the synthesis point of view. In this respect, various perovskites have emerged as a promising substitute to the precious metals.[3,4,13] The catalytic activity of 3d transition metal based perovskites with varying doping percentage was identified by Bockris and Otagawa, whose work pioneered the way in understanding the reaction pathway and also the property-activity relationships.[14] These perovskites also serve with an extra benefit in terms of the compositional flexibility provided by them, giving a platform to tune the activity via its electronic structure. In an ABO_3 type perovskite, both 'A' and 'B' sites can be systematically varied with metals of different radii and valences. Partial doping is also a very common practice, bringing a systematic change in the physiochemical properties of the material. There is plethora of literature identifying different combinations of elements,[13,15–18] but it has been observed that the oxygen-deficiency enhances the catalytic activity incurred by the increased electrical conductivity, leading to the development of a series of double perovskites.[19] In addition to this, porosity in the nanostructured materials leads to defects and variable oxygen stoichiometry, resulting in enhanced electrocatalytic performance for ORR/OER reactions.[20–22] Plethora of literature is available on Co based perovskites that have shown extremely good catalytic activity for both ORR and OER processes.[1–4,23,24]

A recent work by Ashok *et al.* on oxygen reduction reactions, reveals that in terms of stability, $LaCoO_3$ lies above $LaMnO_3$, making the former a better catalyst. However, Mn based perovskite gives a higher current density than its Co counter-part, suggesting its potential to show better performance.[25] Hence, it is desirable to design Mn based perovskites with enhanced stability. It has been found that double perovskites have the potential in bridging this gap. An Mn based double perovskite was found to be stable and shows good catalytic activity towards OER/ORR.[22] The superior activity is a result of inherent surface defects and variable oxygen stoichiometry.[22] In addition to that, these double perovskites

result in the 5 coordinated square pyramidal Mn center, where as, a conventional perovskite has a 6 coordinated octahedral symmetry. This results in the further splitting of e_g levels which were degenerate earlier. This e_g filling is a well established descriptor for the activity of a catalyst.[4,26] The e_g splitting causes a more controlled change over the occupancy which ideally is supposed to be ~ 1.2 for a good OER catalyst.

Though, $Ca_2Mn_2O_5$ shows good catalytic activity, it still does not occupy the top position of the traditional volcano plot, which is widely used to scrutinize the efficiency of catalysts. With the idea of enhancing the catalytic activity of the pristine $Ca_2Mn_2O_5$, we have done a comprehensive theoretical modeling of $Ca_2Mn_2O_5$ by replacing Ca with alkaline earth, lanthanides and main group elements in accordance with maintaining the Goldschmidt tolerance factor (t) between 0.71 - 0.90. Goldschmidt tolerance factor is an indicator for the stability and distortion of crystal structures. It can also be used to calculate the compatibility of an ion with the crystal structure. This factor helps in choosing the substituent dopants keeping the overall geometry of the perovskite unchanged. In addition to that, it is already known that for $A_2B_2O_5$, the valency of A can vary between +2 to +4. Thus, we have chosen the dopants of different valency in order to see its impact on the catalytic activity of the surface. The doping is sequentially done by varying the percentage of dopant from 10% to 40%, which eventually tunes the electronic structure of the catalyst. We have also developed a linear regression based model that can predict the activity of the catalyst from its pristine structure. We hope that this work will widen the horizons of rational catalyst designing.

2.2 Methods

First principles calculations were carried out using Quantum Espresso 5.2.0 package.[27,28]. Generalized gradient approximation was incorporated via the exchange

correlation functional parameterized by Perdew-Burke-Ernzerhoff (PBE).[29,30] The core electrons were treated in the Rappe-Rabe-Kaxiras-Joannopoulos ultrasoft pseudopotential method.[31] Due to strong correlation of d–electrons in Mn, the Hubbard U correction[32] was applied to Mn with a specific value of 4.0 eV, in accordance with some recent calculations on Mn.[33] Spin polarization was applied on Mn with spin structure as ferromagnetic, as is reported about the spin state for experimentally synthesized $Ca_2Mn_2O_5$.[22] The 3×3×1 Monkhorst Pack[34] reciprocal grid was used to sample out the total energy numerically. In order to accelerate the computation near the Fermi level, a Methfessel-Paxton smearing of 0.01 was used.[35] The Broyden–Fletcher–Goldfarb–Shanno algorithm[36] was used for full relaxation of the atomic positions of both, slab and adsorbed intermediates. Conjugate gradient method was used for the electronic relaxation and simultaneous DOS, PDOS and Bader charge calculations.[37] The wave function kinetic energy cutoff was 30 Ry, for energy accuracy.

To avoid the asymmetric slab induced dipole moments, all the slabs were constructed symmetrically considering the (001) plane A–Mn–O (A=Ca/Dopants) as the terminating layer. The cell was chosen following a series of calculations, to make sure that the boundary effects are excluded. The inter-adsorbate distance was maintained at more than 5 Å to avoid adsorbate-adsorbate interactions. The 2X1X5 unit cell was finally chosen after checking for the adsorption energy of OH on the surface, for different number of layers. Similar size of unit cells have been used in the previous calculations as well yielding reliable results.[38] Surface Mn was identified as the catalytically active site in all the cases and all the adsorbates, $^*O$, $^*OO$, $^*OH$ and $^*OOH$ were bonded to Mn. As an initial guess, the adsorbates were placed over the Ca and Mn centers. But on structural relaxation, the system always preferred the Mn site for binding. There were two Mn sites on the surface, and we have chosen the one giving lower value of adsorption energy corresponding

to OH binding as the catalytically active Mn to proceed with the further calculations in all the cases. All the adsorbates, *O, *OO, *OH and *OOH were bonded to the catalytically active Mn. This is reasonable assumption for modeling OER, which has been used in recent literature.[38] In order to calculate the energy of the ions in solvent, computational hydrogen electrode[39] (CHE) developed by Nørskov *et al.* was used as the reference electrode. In accordance with this model, the concerted step of proton and electron transfer can be converted to the half energy of hydrogen molecule. The same concept has been applied to estimate the energy of (e^- – OH^-).

$$H_2O(l) \longrightarrow H^+(aq) + OH^- \tag{2.1}$$

From the CHE model electrode theory,

$$\begin{aligned} H^+ + e^- &\longrightarrow \frac{1}{2}H_2 \\ \Delta G_{(H_2O)} &= (H^+_{aq} + e^-) + (OH^- - e^-) \\ \Delta G_{(H_2O)} &= \Delta G_{(\frac{1}{2}H_2)} + (OH^- - e^-) \\ \Rightarrow \Delta G_{(H_2O)} - \Delta G_{(\frac{1}{2}H_2)} &= (OH^- - e^-) \end{aligned} \tag{2.2}$$

Thus, all the electrochemical reaction energies were mapped to the value with reference to reversible hydrogen electrode (RHE). Solvation is expected to influence the adsorption of intermediates on the surface. However, computation of the solvation free energy corrections requires further validation of the models itself with the experiments, which is demanding. In addition to that, little data is available on the explicit water models on perovskites. Considering the results on Pt(111) surface, it was found that the *OH adsorption is stabilized by 0.50 eV and that of *OOH by 0.25 eV, on inclusion of solvation effects.[40] The net effect of the additional water layer on the overpotential will be 0.25 V.[40] Even if the solva-

tion effect is applied, the qualitative interpretation of the results would remain unchanged, in view of the fact that the rate determining step remains the same for all the catalysts considered.[41] The thermodynamic and entropic aspect was included in the 0K electronic energy of the slab+ adsorbate configuration from the previous works of Montoya *et al.*[41] It should be noted that for our calculations, all the reactions are considered at U=0 and pH=0.

For all of our calculations on (un)doped $Ca_2Mn_2O_5$, a 5–atomic layer slab with (001) plane A–O–Mn exposed layer was constructed with 12Å vacuum layer. The (001) surface with transition metal ions has been widely used as a catalytically active and stable surface for simple perovskites in DFT calculations.[42,43] We hypothesize this to be the case of $Ca_2Mn_2O_5$. The simulation slabs used for DFT calculations were fully oxidized and the structures were relaxed. This is inline with other calculations considering the fact that the OER process occurs in KOH where these slabs would expected to be oxidized. Since the PBE functional predicts over–binded triplet O_2–dimer, the O_2 free energy at 298.15 K was estimated as:

$$\Delta G_{O_2} = 2\{\Delta G_{H_2O} - \Delta G_{H_2}\} \tag{2.3}$$

In a similar way, the free energy of OH^- was estimated as:

$$\Delta \mathrm{G_{OH^-}} = \frac{1}{2}\{\Delta \mathrm{G_{total}} - \Delta \mathrm{G_{O_2}} - 2\Delta \mathrm{G_{H_2O}}\} \tag{2.4}$$

where $\Delta G_{total} = 4 \times 1.23\, eV$. Thus, all the electrochemical reaction energies were mapped to the value with reference to reversible hydrogen electrode (RHE). The thermodynamic and entropic aspect was included in the 0K electronic energy of the slab+ adsorbate configuration from the previous works of Montoya *et al.*[41] The equation to calculate Gibbs reaction energy is:

$$\Delta \mathrm{G_r} = \Delta \mathrm{E_{0K}} + \Delta \mathrm{ZPE} + \Delta \mathrm{H_{0K\rightarrow 298.15K}} - \mathrm{T}\Delta \mathrm{S_{0K\rightarrow 298.15K}} \pm \mathrm{neU} \tag{2.5}$$

in which the ΔE_{0K} is the reaction energy at 0K, ΔZPE is the reaction energy from zero point vibration, $\Delta H_{0K\rightarrow 298.15K}$ and $\Delta S_{0K\rightarrow 298.15K}$ are the enthalpy and entropy contribution in bringing the system from 0K to 298.15K, $\pm neU$ is the electrochemical potential energy for 'n' electrons (system reduction +, system oxidation -) under the electrode potential U. It should be noted that for our calculations, all the reactions are considered at U=0 and pH=0. The OER is a 4-electron exchange process and the U^o for all the steps is estimated as:

1. $HO^* + OH^- \longrightarrow O^* + H_2O + e^-$

$U_1^\circ = \Delta G(HO^*) - \Delta G(O^*) - \Delta G(H_2O) - (e^- - OH^-) - eU$

2. $O^* + OH^- \longrightarrow HOO^* + e^-$

$U_2^\circ = \Delta G(O^*) - \Delta G(HOO^*) - (e^- - OH^-) - eU$

3. $HOO^* + OH^- \longrightarrow OO^* + H_2O + e^-$

$U_3^\circ = \Delta G(HOO^*) - \Delta G(OO^*) - \Delta G(H_2O) - (e^- - OH^-) - eU$

4. $OO^* + OH^- \longrightarrow HO^* + O_2 + e^-$

$U_4^\circ = \Delta G(OO^*) - \Delta G(HO^*) - \Delta G(O_2) - (e^- - OH^-) - eU$

For all the calculations on (un)doped $Ca_2Mn_2O_5$, a 5–atomic layer slab with (001) plane A–O–Mn exposed layer was constructed with 12Å vacuum layer. The (001) surface with transition metal ions has been widely used as a catalytically active and stable surface for simple perovskites in DFT calculations.[42,43] We hypothesize this to be the case of $Ca_2Mn_2O_5$. The simulation slabs used for DFT calculations were fully oxidized and the structures were relaxed. This is inline with other calculations considering the fact that the OER process occurs in KOH where these slabs would expected to be oxidized.

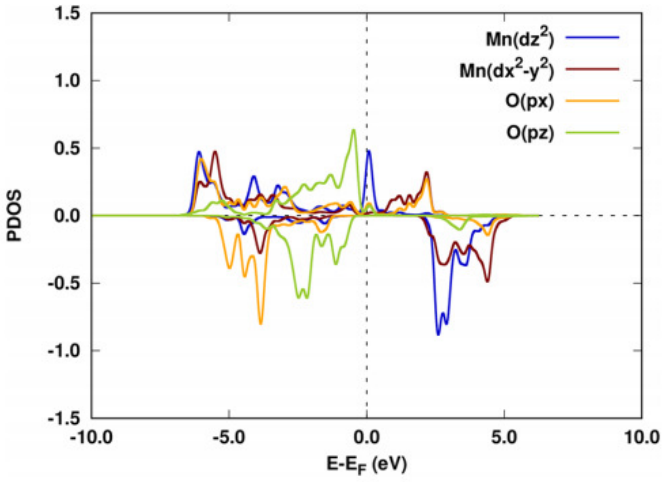

Figure 2.1: The partial density of states (PDOS) of the pristine $Ca_2Mn_2O_5$ for the Mn($d_{x^2-y^2}$), Mn(d_{z^2}), O(p_x) and O(p_z), where Mn is the catalytically active site.

2.3 Results and discussion

2.3.1 Electronic structure of the catalyst

$Ca_2Mn_2O_5$ has an orthorhombic crystal existing in high spin state, where Mn shows a 5 coordinated square pyramidal geometry with O atoms as its neighbours.[22,44] This is a striking difference from the orthorhombic $CaMnO_3$, where Mn center has an octahedral symmetry and is surrounded by 6 O atoms. It is probably due to this symmetry breaking, that the e_g levels become non-degenerate and give rise to more catalytically active Mn centers. The five coordinated Mn can exist in two geometries, i.e. trigonal bipyramidal and the square pyramidal and the d-orbital splitting is strikingly different in the two cases, as shown in fig. 2.2. The covalency of the attached ligands decide which of the two geometries will be favoured. This leads to the proper tuning of the orbital alignment and thus controlling the activity of the catalyst. In covalent complexes where presumably the interactions between the bonded pair of electrons are more important than the bonded–non bonded electron pair interactions, the trigonal bipyramidal configuration is favoured. On the other hand, it is essentially the ionic compounds in which the interactions be-

tween bonding electron pairs and the d-shell predominates and in which a square pyramidal geometry exists. An important point worth mentioning is that the d^4 configuration is more stable in the bipyramidal geometry rather than the square pyramid. The two geometries can interchange which may lead to a significant rearrangement of the d-orbitals.[45] This interchange is mainly governed by the electronic character of the ligands around, the d-shell configuration and the covalency of the metal-ligand bond.[45] The PDOS of $Ca_2Mn_2O_5$ reveals the splitting of the e_g levels (Figure 2.1). This was also observed in some of the earlier works on cobalt based perovskites.[24,46]

2.4 Simulated systems

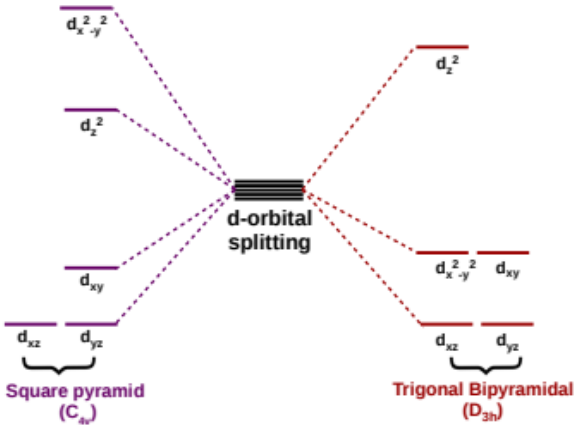

Figure 2.2: Different crystal-field splitting of d-electrons states for the square pyramid and trigonal bipyramid symmetry around the 5 coordinated Mn ions.

2.4.1 Selecting the dopants

The above discussion leads to the fact that tuning the e_g level of the transition metal center may lead to good catalytic activity.[3,4,13] In this work, e_g levels are

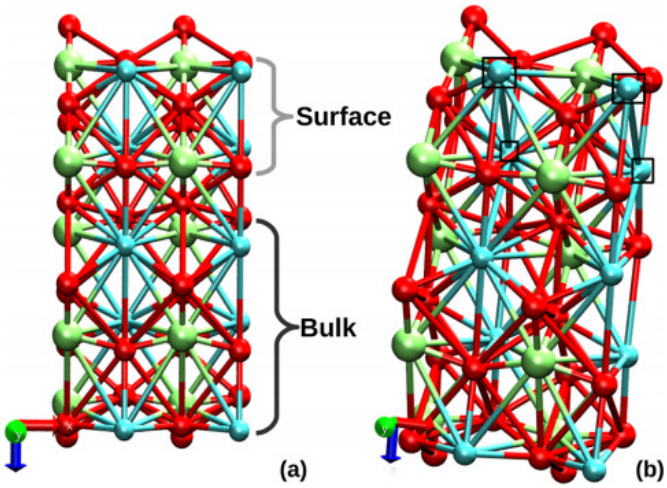

Figure 2.3: (a) Relaxed structure of $Ca_2Mn_2O_5$ (001) surface with 5 layers. The bottom three layers were constrained to represent the bulk, and the top two layers were allowed to change their positions in the presence of adsorbate. The colour code: limegreen=Mn, Cyan=Ca, Red=O (b) The highlighted Ca are the positions that were considered for sequential doping.

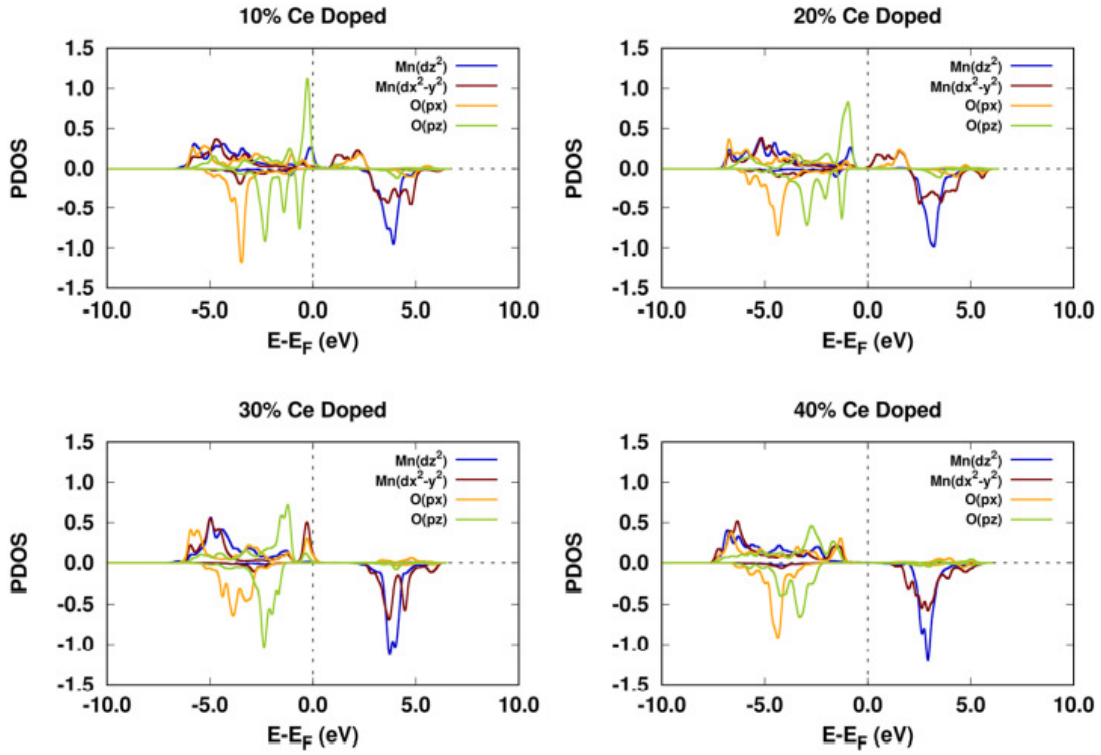

Figure 2.4: The partial density of states (PDOS) of the Ce doped $Ca_2Mn_2O_5$ of the Mn($d_{x^2-y^2}$), Mn(d_{z^2}), O(p_x) and O(p_z), where Mn is the catalytically active site.

tuned by replacing Ca (Site 'A' in $A_2B_2O_5$) on the top two layers of the (001) plane of pristine $Ca_2Mn_2O_5$ with Sr, In, Bi, La, Ce and Eu (Figure 2.3). The doping percentage is sequentially varied from 10 to 40%. Positions of the dopant were varied for all the cases and the minimum energy confirmation was chosen for further study. Similarly, active site of the catalyst was analyzed on the basis of adsorption energies with respect to OH to find the minimum energy catalyst–adsorbate complex as mentioned above. It is known that due to the difference in radii and electronegativity of site 'A', the d-filling of the corresponding 'B' site gets altered due to modification in the B–O bond.[46] Change in electronic environment due to doping is analyzed in terms of the projected density of states (PDOS) plots. As is evident from Figure 2.10, varying the doping percentage of 'A' modifies the O-p and metal d-band. The PDOS of pristine catalyst (Figure 2.1) shows the presence of $d_z{}^2$ orbital crossing the Fermi level which is in close proximity to the occupied O-p_z orbital. This observation is in line with an earlier reported result by Lu *et al.*[44] As a result of doping (Ca with 10% of another element), the density of states corresponding to Mn-d_{z^2} are shifted and reduced and that of O-p_z is increased. As doping percentage is increased, the Mn-d_{z^2}, d_{xz} and d_{yz} tend to get more stabilized and shift away from the Fermi level. On 30% doping with Ce, Mn-$d_{x^2-y^2}$ and O-p_z and O-p_x become degenerate and lie near the Fermi level. On further increase in doping, the density of states is shifted away from the Fermi level. It is important to note that, this reduction in catalytic activity on doping beyond 30% may occur at any composition between 30% and 40%. Our modelled catalysts are restricted by a resolution of 10% with respect to each doping concentration. This suggests that doping 'A' has a huge implication on the electronic structure around 'B' and hence can influence the catalytic activity considerably.

2.4.2 Free energy calculations

As proposed by Goodenough *et al.*, the OER process on the perovskite surface takes place in alkaline medium.[3] The reaction scheme proposed by him is given in Figure 2.5, and involves 4 electron transfer steps. As per recent studies, there are chances of the lattice oxygen to take part in the reaction, making the OH^- and e^- transfer non-concerted, as a result of which reaction becomes pH dependent.[24] This is thermodynamically favoured when the O 2p states at the perovskite Fermi level lie above the redox energy of the O_2/H_2O couple. As per our analysis of the PDOS plots, this does not happen in any of the cases, thus ruling out the possibility of a lattice oxygen participation in the reaction. Table 2.4 has the data on the p-band center. As can be seen that the p-band center is way below the -1.8 eV mark to show instability in OER reaction conditions.[46] The p-band center and the covalency data also depict the inability of the lattice oxygen to take part in the catalysis.[24,47] In order to model the thermodynamics of the reaction, computational hydrogen electrode model proposed by Nørskov *et al.* was used.[39] The reactions were modeled considering the OH^- and e^- transfer as a concerted[48–50] step.

The details are given in the method section. The linear free energy relationships (LFER) allow us to relate the thermodynamics to the kinetics of the reaction for an isoentropic process via Brønsted–Evans–Polyani relation. Thus, a thermodynamic picture is deemed accurate to evaluate the performance of the catalysts.[51,52] It is already known that the free energies scale up/down with the change in applied external potential (U). Hence, the potential determining step remains unchanged, making the theoretical overpotential independent of U and we represent this potential at 0 pH as U^o. Figure 2.6 shows the standard equilibrium potential (U^o_x, x=1,2,3,4) for all the four steps. For an ideal catalyst this value should be the same for all the steps i.e. 1.23 V, at zero U. However, in real catalysts this does

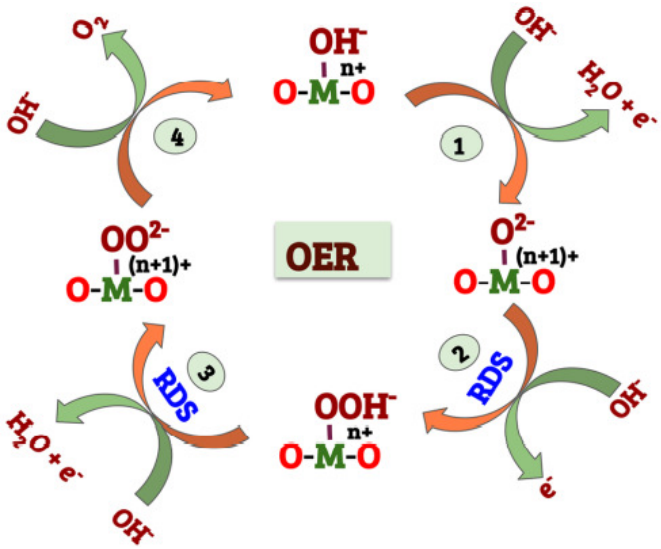

Figure 2.5: The reaction scheme as proposed by Goodenough *et al.*[3] for an OER process taking place on a perovskite surface in alkaline medium.

not happen. We find U_2^o, which involves the O–O bond formation, as the potential determining step for all cases. This further determines the overpotential of the reaction via Equation 2.6.[53]

$$\mathrm{U^{OER}} = \max[\mathrm{U_1^o}, \mathrm{U_2^o}, \mathrm{U_3^o}, \mathrm{U_4^o}]; \qquad \eta^{\mathrm{OER}} = \mathrm{U^{OER}} - 1.23\,\mathrm{V} \tag{2.6}$$

It is interesting to note that the η predicted for $Ca_2Mn_2O_5$ using the above formulation gives a value of 0.26 V which is close to the experimentally reported value of 0.27 V, providing a good confidence in our theoretical predictions. The rate determining step (RDS) is controlled by the e_g filling of the underlying catalyst metal center (Mn, in our case). It is either the O–O bond formation or the proton abstraction from the oxy-hydroxide group, which determine the rate OER.[3] The O–O bond formation is the RDS when $e_g > 1$, which is consistent with our calculations.[3,54] It is evident from Figure 2.6 that increasing the doping concentration does not always reduce the U^o. Rather, in all the cases, U^o increases in

going from 30% to 40%. In most of the cases, 30% doping concentration gives

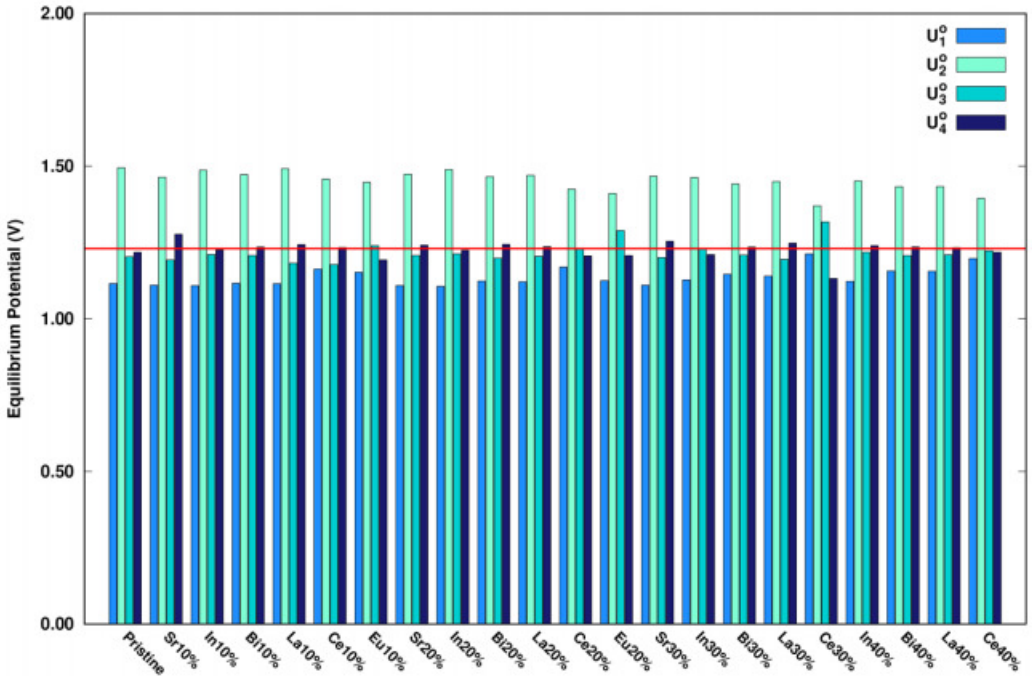

Figure 2.6: A comparison of all the U_x^o (x=1,2,3,4) for all the steps of the OER process in all the studied (un)doped systems. The red line corresponds to the thermodynamic equilibrium potential of 1.23 V, for an ideally reversible process.

minimum overpotential value. This suggests that electronic modification caused at this percentage is ideal for OER. It is known that the nature of 'A' can tune the concentration of oxygen vacancies and the oxidation state of the central metal, which in turn govern the overall OER activity.[46] As discussed earlier, PDOS for Ce (Figure 2.10) shows rearrangement of t_{2g} and e_g levels as the doping percentage is varied. At 30%, the $d_{x^2-y^2}$ overlaps with the p-band of lattice oxygen. This allows for more covalency in the metal-oxygen bonding, thereby modifying the e_g filling of the metal. It can be hypothesized from here that the electronic modulation at 30% doping of Ce is perfectly ideal for OER catalysis, thereby resulting in lower overpotential values.

The e_g filling also depends on the oxidation state of the metal center. It has been

found earlier that the oxidation state of metal center varies with the radius of 'A'.[46] Grimaud *et al.* have reported an increase in the oxidation state of the metal, with respect to the increase in the ionic radius of 'A'. Bader charge analysis shows a reduction in charge of Mn which is inversely proportional to the radii of dopant 'A'. Interestingly, it is also observed that the electronegativity of 'A' also effects the oxidation state of 'B'. Bader charge analysis suggests that as the doping percentage is increased, the oxidation state of the metal center tends to decrease and this points towards an increase in the e_g filling that exceeds more than 1 (ideal case for Mn^{3+} with weak ligands). From our estimation we conjecture that both, over oxidation or over reduction of Mn leads to poor overpotential and we identify 30% doping as ideal for these Mn based perovskites.

2.4.3 Scaling relations

The adsorption energies of all the intermediates suggests that the bond strengths follow the order: $E_{*OH} > E_{O^*} > E_{*OOH} > E_{OO^*}$. It is evident from Figure 2.7 that

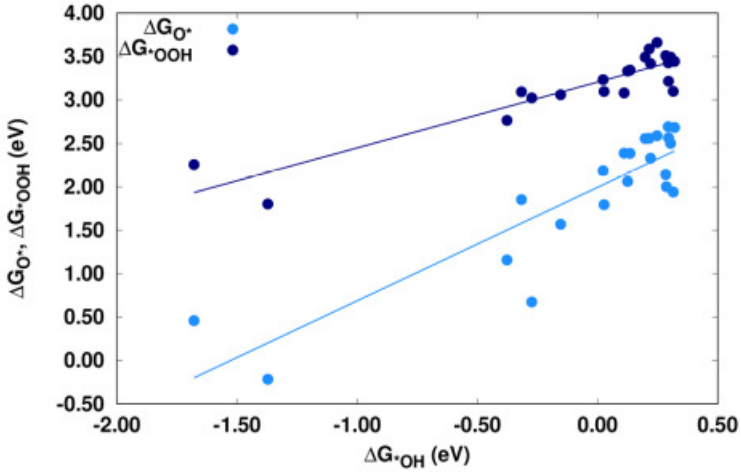

Figure 2.7: Scaling relations between adsorption free energy values of *O and *OOH with that of *OH for various (un)doped catalysts. $\Delta G_{*O} = 1.70\Delta G_{*OH} + 1.97$, $\Delta G_{*OOH} = 0.93\Delta G_{*OH} + 3.18$.

all the adsorption free energies of intermediates scale with ΔG_{*OH} which is in line with earlier reported results.[51–53,55,56] Figure 2.7 shows that ΔG_{*OH} strongly correlates with ΔG_{*OOH} and ΔG_{*O} giving a Pearson correlation[57] coefficient of 0.92 and 0.90, respectively. These scaling relations consequently affect the catalyst design, suggesting that even the most active catalyst will have a non-zero overpotential. The binding energy of *OH and *OOH have 1:1 scaling with a constant difference of 3.18 eV which is in agreement with the earlier finding by Rossmeisl *et al.* where it is mentioned that this scaling is independent of the surface.[49] However, this indicates towards a non-zero overpotential because ideally this difference should be 2.46 (2*1.23) V. The ΔG_{*O} and ΔG_{*OH} have a 2:1 scaling owing to the double bond character of the metal–*O bond. A constant intercept also implies that these intermediates prefer same type of binding site (Mn center in this case).

2.4.4 Identifying Activity Descriptors

Existence of a universal scaling relation between ΔG_{*OOH} and ΔG_{*OH}, eliminates the possibility of a variation in η^{OER} with it. Earlier reports state that the adsorption of *O on the catalyst surface determines the η^{OER} of the reaction, suggesting step (2) or step (3) to be the rate determining step (RDS). Thus, ΔG_{*O}–ΔG_{*OH} is identified as a universal descriptor for the OER process.[52,53] In agreement with these findings, Figure 2.8 shows a linear correlation of ΔG_{*O}–ΔG_{*OH} with η^{OER} with a Pearson correlation of 0.93. The difference in the adsorption energies of *O and *OH is thus determining the overpotential of the reaction, which for an ideal catalyst should be zero. The colinearity in the plot suggests a similar RDS for all the catalysts considered in this study. This is known as the universal volcano relation, where in our case, the adsorbate binds weakly to the catalyst. The higher the catalyst lies towards the peak, the better is its catalytic performance. From

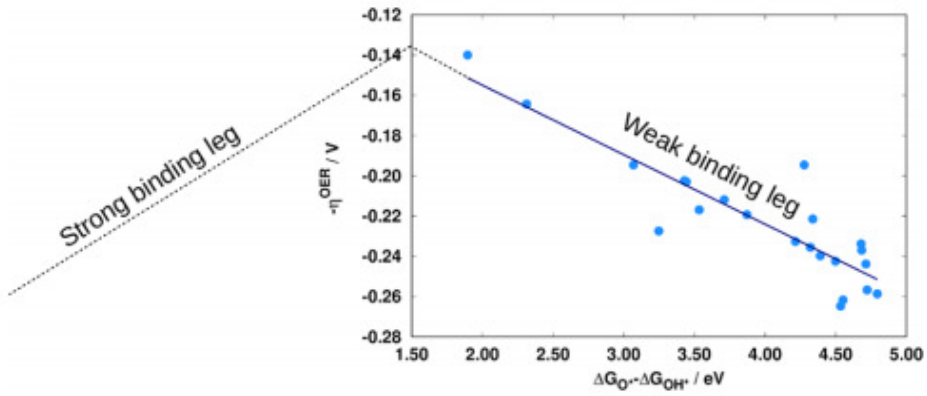

Figure 2.8: Activity volcano relation for (un)doped Mn based double perovskites. $\eta^{\mathrm{OER}} = 0.069(\Delta \mathrm{G}_{*\mathrm{O}} - \Delta \mathrm{G}_{*\mathrm{OH}}) + 0.086$

Figure 2.8, we identify 30% Ce doped $Ca_2Mn_2O_5$ ($Ce_{0.7}Ca_{1.3}Mn_2O_5$) for the class of catalysts considered in this study. η^{OER} for this system is 0.14 V, which is less than that for pristine $Ca_2Mn_2O_5$ (η^{OER}=0.26 V). This difference in the η^{OER} can be attributed to the stability of *O on the Ce doped surface owing to the oxophilicity of the Ce atom. Presence of Ce in vicinity of the reactive site facilitates in the O-O bond formation via a non covalent interaction of Ce with O* resulting in a reduction of electron density over O, facilitating the bond formation with nucleophilic OH^-. The overpotential estimated for Ce doped $Ca_2Mn_2O_5$ is even lower than the experimentally reported overpotential for some Ni-based hydroxides hierarchical nanoarrays, which is 0.23 V, and is reportedly the best catalyst for OER till date, to the best of our knowledge.[58]

2.4.5 Predictive model for OER activity

Development of quantitative structure–activity relationship is central to the rational design of novel catalysts.

These models enable to develop relationship between the desired catalytic ac-

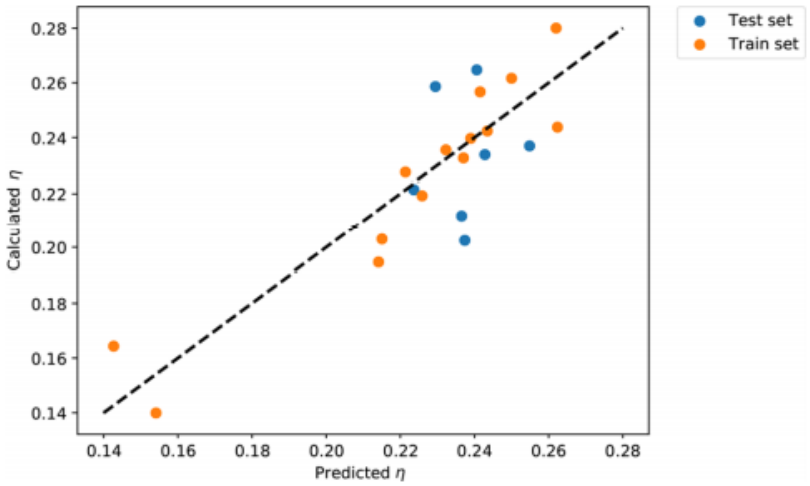

Figure 2.9: The predicted versus the calculated values of η^{OER} using the linear regression based model. The R^2 for this model is 0.83.

tivity and the structural/electronic properties of the material. This enables a fast screening of the probable candidates for catalysis and saves a lot of time, effort and expenses. Such models have been developed in the past which used around 14 structural descriptors on a data set for 51 perovskite catalysts.[?] Here, we use a set of 4 descriptors on a data-set of 21 catalysts where only the 'A' site is varied. The descriptors are based on the geometry, like the tolerance factor, percentage doping, and on the electronic structure, like, Fermi energy, p-band center for the surface lattice oxygen and metal-oxygen covalency. These descriptors are easy to estimate from the very basic theoretical calculations and are highly intuitive about the nature of the material under study. Figure 4.2 shows the predicted versus the calculated values of η^{OER}. The corresponding model is given in Table 2.1.

It is evident from here, that this simple model is able to predict the η^{OER} with a reasonably good accuracy (R^2=0.86). In order to develop the model, data are randomly splitted into training set (composing 70% of the total) and test set. It may be argued that with such a small data-set and low variation in the test systems, this model may be highly biased. However, we would like to emphasize on

Table 2.1: Details of the multiple regression based predictive model. The intercept value for the model is 0.2000 eV. The importance value is estimated as the difference in the corresponding R^2 values, when the corresponding variable is replaced with its average value.

Variable	Coefficient	Importance
Fermi Level (eV)	-0.0075	0.10
p–band center (eV)	0.0100	0.15
t×%doping	0.0393 (eV)	0.10
Covalency	0.1395 (eV)	0.17

Table 2.2: Details of the descriptors used

p-band center	Calculated based on the PDOS as $\frac{\int E.f(E)dE}{\int f(E)dE}$
Mn-O bond covalency	Average Bader charge difference between the surface Mn and O atoms.
t×% doping	$t = \frac{r_A+r_O}{\sqrt{2}(r_B+r_O)}$ where r_A was the radius of the dopant. This factor was multiplied with percentage doping.
Fermi energy	Highest occupied energy level of a material at absolute zero temperature.

the fact that a relatively simple model is able to capture a wide range of elements of the periodic table and can stand useful for further generalization by testing it on a wider range of data. Moreover, the model is relatively simple and thus, much more intuitive for rational materials design. An importance analysis is done in order to evaluate the contribution of the variables towards the model. It is found that the covalency of the metal-oxygen bond is the most dominant factor in determining the OER activity, followed by p-band center. The Fermi energy and the tolerance factor parameter have equal effect on the predictive ability of the model.

2.4.6 Multiple Regression based predictive model

The supervised machine learning can be divided into two parts: regression and classification, where regression predicts continuous value outputs and classification predicts discrete outputs. Multiple linear regression falls in the first category. This

simply corresponds to a linear relationship between two or more variables. When the number of descriptors/variables exceeds 1, it falls in the category of multiple linear regression. We used the Scikit–learn library within python to develop the model.[?] The dataset was randomly split into 70% training set and 30% test set. The model was based on the slope that corresponds to the data of the training set and the y–intercept which again is derived from the training set. The model was evaluated based on the R^2 value. The better the model, R^2 approaches 1.
The importance analysis for the variables was also done in order to evaluate how much impact would a descriptor have on the model. This was done by replacing the value of the descriptor with an average value and see the difference in R^2 before and after the substitution.

The PDOS for all the pristine catalysts is given in Figures 10 to 13. Only the significant O p–band, Mn d–band are shown. In case of 30% Ce doped catalyst, a dominant O p–band is observed near the valence band maximum. The oxygen p–band center was calculated based on the PDOS of every system, by intergrating oxygen PDOS over the p–band using:

$$\mathrm{p-band\,center} = \frac{\int \mathrm{E.f(E)dE}}{\int \mathrm{f(E)dE}} \tag{2.7}$$

where E is the electronic energy and f(E) is the density of states corresponding to that E. To get the charge density on the atoms, we have used Bader analysis, which is based upon partitioning charge density grid into Bader volume by steepest ascent method.[59]

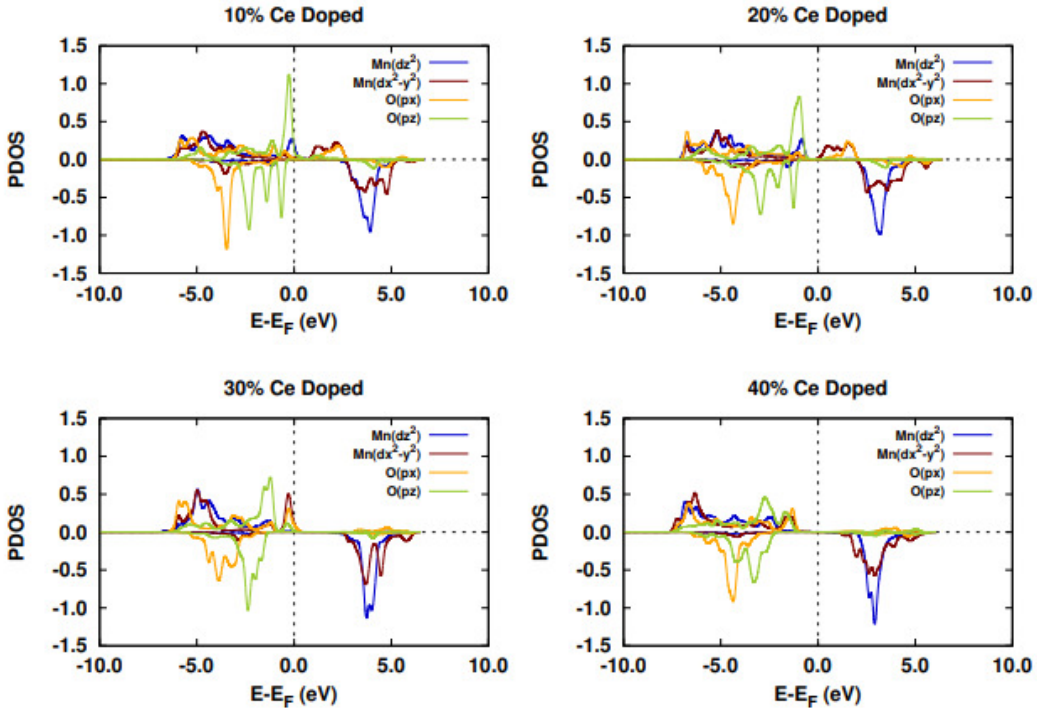

Figure 2.10: The partial density of states (PDOS) of the Ce doped $Ca_2Mn_2O_5$ of the Mn($d_{x^2-y^2}$), Mn(d_{z^2}) and O(p_z), where Mn is the catalytically active site.

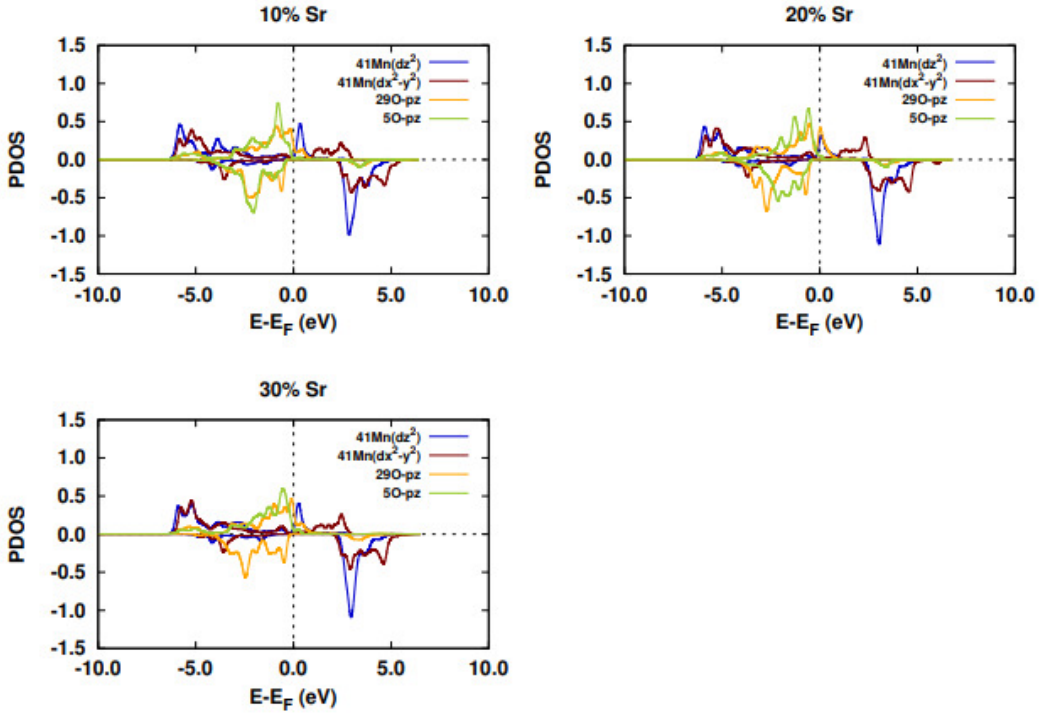

Figure 2.11: The partial density of states (PDOS) of the Sr doped $Ca_2Mn_2O_5$ of the Mn($d_{x^2-y^2}$), Mn(d_{z^2}) and O(p_z), where Mn is the catalytically active site.

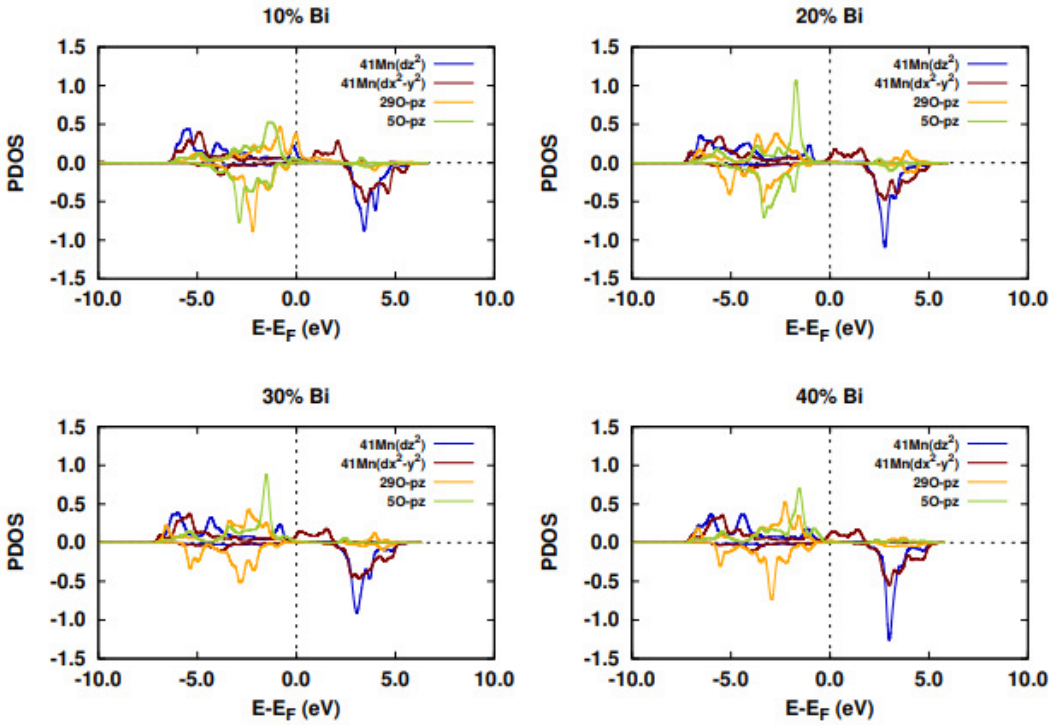

Figure 2.12: The partial density of states (PDOS) of the Bi doped $Ca_2Mn_2O_5$ of the Mn($d_{x^2-y^2}$), Mn(d_{z^2}) and O(p_z), where Mn is the catalytically active site.

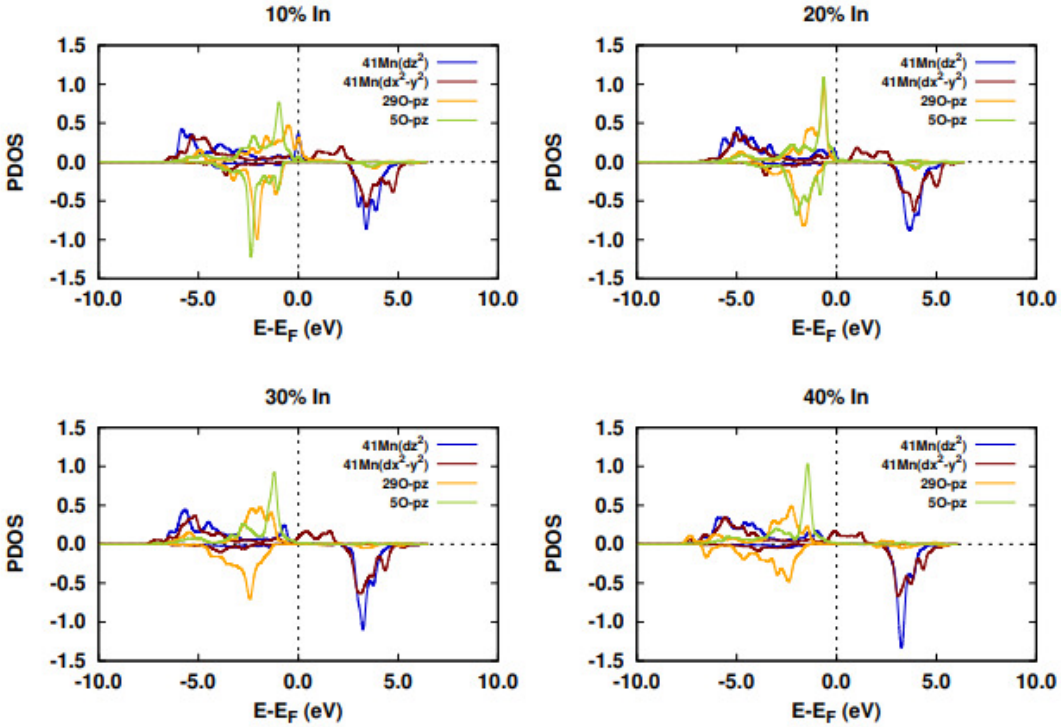

Figure 2.13: The partial density of states (PDOS) of the In doped $Ca_2Mn_2O_5$ of the Mn($d_{x^2-y^2}$), Mn(d_{z^2}) and O(p_z), where Mn is the catalytically active site.

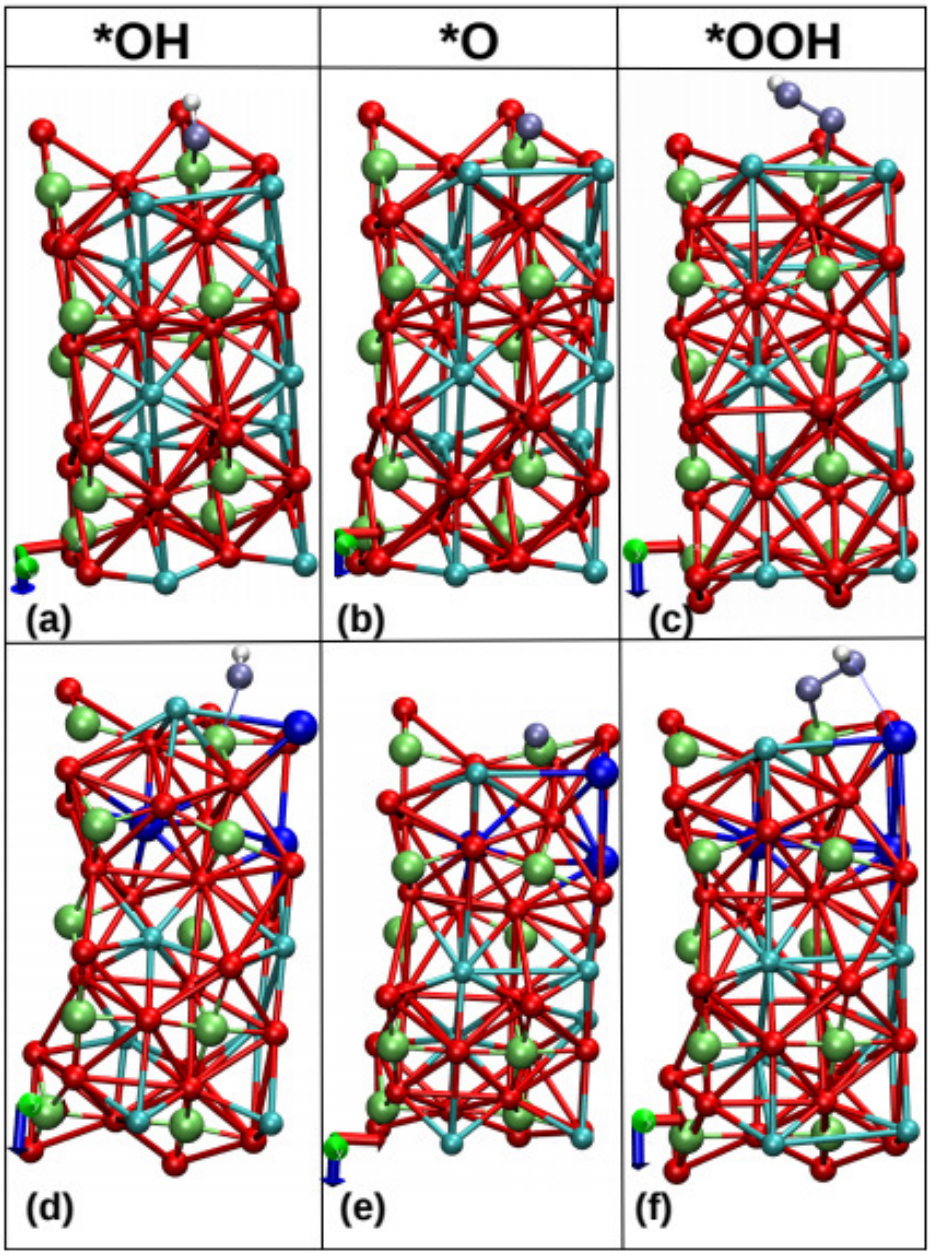

Figure 2.14: Atomic structures of pristine (a,b,c) and 30% Ce doped (d, e, f) $Ca_2Mn_2O_5$ with adsorbed *OH, *O and *OOH, respectively. The colour code is: deep blue is Ce, limegreen is Mn, Cyan is Ca, Red is O. Adsorbed oxygens are in ice blue colour to differentiate them from lattice oxygen. White ball represents hydrogen. The dotted line shows non–covalent interaction between adsorbed *OOH and lattice oxygen.

Table 2.3: The standard equilibrium potential (in eV) for the four steps of OER process corresponding to the (un)doped catalysts

System	U_1^o	U_2^o	U_3^o	U_4^o
$Ca_2Mn_2O_5$	1.12	1.49	1.20	1.22
Sr 10%	1.11	1.46	1.19	1.28
In 10%	1.11	1.49	1.21	1.23
Bi 10%	1.12	1.47	1.21	1.24
La 10%	1.11	1.49	1.18	1.24
Ce 10%	1.16	1.46	1.18	1.23
Eu 10%	1.15	1.45	1.24	1.19
Sr 20%	1.11	1.47	1.21	1.24
In 20%	1.11	1.49	1.21	1.22
Bi 20%	1.12	1.47	1.20	1.24
La 20%	1.12	1.47	1.20	1.24
Ce 20%	1.17	1.42	1.23	1.21
Eu 20%	1.13	1.41	1.29	1.21
Sr 30%	1.11	1.47	1.20	1.25
In 30%	1.13	1.46	1.23	1.21
Bi 30%	1.15	1.44	1.21	1.24
La 30%	1.14	1.45	1.19	1.25
Ce 30%	1.21	1.37	1.32	1.13
In 40%	1.12	1.45	1.22	1.24
Bi 40%	1.16	1.43	1.21	1.24
La 40%	1.16	1.43	1.21	1.23
Ce 40%	1.20	1.39	1.22	1.22

Table 2.4: The data that was used for generating the linear regression based model. The e_g filling was not the part of the final model owing to its inaccuracy in predicting the overpotential (η).

System	η	Fermi level	e_g filling	p-band center	t×%dope	Covalency
$Ca_2Mn_2O_5$	0.26	2.23	1.03	-2.19	0.00	0.57
10%Sr	0.23	2.48	1.02	-2.23	0.09	0.67
20%Sr	0.24	2.25	1.02	-2.07	0.18	0.62
30%Sr	0.24	2.62	1.02	-2.23	0.27	0.64
10%In	0.26	2.42	1.02	-2.25	0.08	0.57
20%In	0.26	2.46	1.02	-2.17	0.15	0.46
30%In	0.23	2.50	1.03	-2.42	0.23	0.51
40%In	0.22	2.95	1.03	-2.65	0.30	0.43
10%Bi	0.24	2.31	1.02	-2.11	0.08	0.56
20%Bi	0.24	2.60	1.02	-2.22	0.17	0.48
30%Bi	0.21	3.02	1.02	-2.46	0.25	0.53
40%Bi	0.20	3.27	1.02	-2.57	0.34	0.53
10%La	0.26	2.30	1.02	-2.04	0.08	0.60
20%La	0.24	2.48	1.02	-2.11	0.17	0.52
30%La	0.22	3.11	1.03	-2.55	0.25	0.46
40%La	0.20	3.56	1.03	-2.70	0.34	0.40
10%Ce	0.23	2.47	1.03	-2.76	0.08	0.46
20%Ce	0.19	3.11	1.03	-2.62	0.17	0.41
30%Ce	0.14	3.34	1.04	-2.58	0.25	-0.03
40%Ce	0.16	4.24	1.02	-3.02	0.33	-0.06

2.5 Conclusions

In summary, a comprehensive study has been made on Mn based oxygen deficient double perovskite i.e. $Ca_2Mn_2O_5$ by doping Ca with Sr, In, Bi, La, Ce and Eu. The dopant percentage is varied from 10% to 40%, in order to see the effect of these different percentages on the catalytic activity of the perovskite. It is found that due to doping, the density of states near the Fermi level are affected, leading to a square pyramidal type d-orbital ordering. This leads to the tuning of the e_g level and hence the catalytic activity of the system. We identify 30% doping as ideal, which tunes the electronic structure optimally for good OER activity. For all the cases, we identify the O–O bond formation as the rate determining step, and it correlates well with being the RDS for e_g occupancy > 1. Of all the elements studied, 30% Ce doped catalyst shows the best results in terms of the lowest thermodynamic overpotential. We develop a linear regression based predictive model that uses simple, but intuitive descriptors, like metal-oxygen bond covalency, p–band center, Fermi level and tolerance factor. These kind of models would make the catalyst design faster and efficient by considerably reducing the effort and computational cost that goes into the screening of the potential catalysts. With these results, we hope for the development of novel cost-effective perovskite based catalysts for OER.

References

[1] J. Hwang, R. R. Rao, L. Giordano, Y. Katayama, Y. Yu and Y. Shao-Horn, *Science*, 2017, **358**, 751–756.

[2] B. Han, K. A. Stoerzinger, V. Tileli, A. D. Gamalski, E. A. Stach and Y. Shao-Horn, *Nature materials*, 2017, **16**, 121–126.

[3] J. Suntivich, K. J. May, H. A. Gasteiger, J. B. Goodenough and Y. Shao-Horn, *Science*, 2011, **334**, 1383–1385.

[4] J. Suntivich, H. A. Gasteiger, N. Yabuuchi, H. Nakanishi, J. B. Goodenough and Y. Shao-Horn, *Nature Chemistry*, 2011, **3**, 546–550.

[5] S. Muy, J. C. Bachman, L. Giordano, H.-H. Chang, D. L. Abernathy, D. Bansal, O. Delaire, S. Hori, R. Kanno, F. Maglia *et al.*, *Energy & Environmental Science*, 2018, **11**, 850–859.

[6] E. A. Ahmad, V. Tileli, D. Kramer, G. Mallia, K. A. Stoerzinger, Y. Shao-Horn, A. R. Kucernak and N. M. Harrison, *The Journal of Physical Chemistry C*, 2015, **119**, 16804–16810.

[7] N.-I. Kim, Y. J. Sa, T. S. Yoo, S. R. Choi, R. A. Afzal, T. Choi, Y.-S. Seo, K.-S. Lee, J. Y. Hwang, W. S. Choi *et al.*, *Science Advances*, 2018, **4**, 9360.

[8] H. Wang, H.-W. Lee, Y. Deng, Z. Lu, P.-C. Hsu, Y. Liu, D. Lin and Y. Cui, *Nature Communications*, 2015, **6**, 1–8.

[9] V. Pfeifer, T. E. Jones, S. Wrabetz, C. Massué, J. J. V. Vélez, R. Arrigo, M. Scherzer, S. Piccinin, M. Hävecker, A. Knop-Gericke *et al.*, *Chemical Science*, 2016, **7**, 6791–6795.

[10] J. W. D. Ng, M. García-Melchor, M. Bajdich, P. Chakthranont, C. Kirk, A. Vojvodic and T. F. Jaramillo, *Nature Energy*, 2016, **1**, 1–8.

[11] Y.-C. Lu, Z. Xu, H. A. Gasteiger, S. Chen, K. Hamad-Schifferli and Y. Shao-Horn, *Journal of the American Chemical Society*, 2010, **132**, 12170–12171.

[12] S. Park, Y. Shao, J. Liu and Y. Wang, *Energy & Environmental Science*, 2012, **5**, 9331–9344.

[13] J. Suntivich, H. A. Gasteiger, N. Yabuuchi and Y. Shao-Horn, *Journal of The Electrochemical Society*, 2010, **157**, B1263.

[14] J. O. Bockris and T. Otagawa, *The Journal of Physical Chemistry*, 2002, **87**, 2960–2971.

[15] J. Sunarso, S. S. Hashim, N. Zhu and W. Zhou, *Progress in Energy and Combustion Science*, 2017, **61**, 57–77.

[16] H. Sun, G. Chen, J. Sunarso, J. Dai, W. Zhou and Z. Shao, *ACS Applied Materials & Interfaces*, 2018, **10**, 16939–16942.

[17] M. Jiang, J. Li, Y. Zhao, L. Pan, Q. Cao, D. Wang and Y. Du, *ACS Applied Materials & Interfaces*, 2018, **10**, 19746–19754.

[18] F. De Angelis, D. Meggiolaro, E. Mosconi, A. Petrozza, M. K. Nazeeruddin and H. J. Snaith, *ACS Energy Letters*, 2017, **2**, 857–861.

[19] J. Du, T. Zhang, F. Cheng, W. Chu, Z. Wu and J. Chen, *Inorganic Chemistry*, 2014, **53**, 9106–9114.

[20] S. H. Oh, R. Black, E. Pomerantseva, J.-H. Lee and L. F. Nazar, *Nature Chemistry*, 2012, **4**, 1004–1010.

[21] S. H. Oh and L. F. Nazar, *Advanced Energy Materials*, 2012, **2**, 903–910.

[22] J. Kim, X. Yin, K.-C. Tsao, S. Fang and H. Yang, *Journal of the American Chemical Society*, 2014, **136**, 14646–14649.

[23] J.-I. Jung, M. Risch, S. Park, M. G. Kim, G. Nam, H.-Y. Jeong, Y. Shao-Horn and J. Cho, *Energy & Environmental Science*, 2016, **9**, 176–183.

[24] A. Grimaud, O. Diaz-Morales, B. Han, W. T. Hong, Y.-L. Lee, L. Giordano, K. A. Stoerzinger, M. T. Koper and Y. Shao-Horn, *Nature Chemistry*, 2017, **9**, 457–465.

[25] A. Ashok, A. Kumar, R. R. Bhosale, F. Almomani, S. S. Malik, S. Suslov and F. Tarlochan, *Journal of Electroanalytical Chemistry*, 2018, **809**, 22–30.

[26] U. Maitra, B. Naidu, A. Govindaraj and C. Rao, *Proceedings of the National Academy of Sciences*, 2013, **110**, 11704–11707.

[27] P. Giannozzi, S. Baroni, N. Bonini, M. Calandra, R. Car, C. Cavazzoni, D. Ceresoli, G. L. Chiarotti, M. Cococcioni, I. Dabo *et al.*, *Journal of Physics: Condensed Matter*, 2009, **21**, 395502.

[28] T. A. Barnes, T. Kurth, P. Carrier, N. Wichmann, D. Prendergast, P. R. Kent and J. Deslippe, *Computer Physics Communications*, 2017, **214**, 52–58.

[29] M. Ernzerhof and G. E. Scuseria, *The Journal of Chemical Physics*, 1999, **110**, 5029–5036.

[30] C. Adamo and V. Barone, *The Journal of Chemical Physics*, 1999, **110**, 6158–6170.

[31] A. M. Rappe, K. M. Rabe, E. Kaxiras and J. Joannopoulos, *Physical Review B*, 1990, **41**, 1227.

[32] S. Dudarev, G. Botton, S. Savrasov, C. Humphreys and A. Sutton, *Physical Review B*, 1998, **57**, 1505.

[33] Y.-L. Lee, M. J. Gadre, Y. Shao-Horn and D. Morgan, *Physical Chemistry Chemical Physics*, 2015, **17**, 21643–21663.

[34] J. D. Pack and H. J. Monkhorst, *Physical Review B*, 1977, **16**, 1748.

[35] M. Methfessel and A. Paxton, *Physical Review B*, 1989, **40**, 3616.

[36] R. Fletcher, *Practical methods of optimization*, John Wiley & Sons, 2013.

[37] T. A. Arias, M. Payne and J. Joannopoulos, *Physical Review Letters*, 1992, **69**, 1077.

[38] B. Zhao, L. Zhang, D. Zhen, S. Yoo, Y. Ding, D. Chen, Y. Chen, Q. Zhang, B. Doyle, X. Xiong *et al.*, *Nature Communications*, 2017, **8**, 1–9.

[39] J. K. Nørskov, J. Rossmeisl, A. Logadottir, L. Lindqvist, J. R. Kitchin, T. Bligaard and H. Jonsson, *The Journal of Physical Chemistry B*, 2004, **108**, 17886–17892.

[40] V. Tripković, E. Skúlason, S. Siahrostami, J. K. Nørskov and J. Rossmeisl, *Electrochimica Acta*, 2010, **55**, 7975–7981.

[41] J. H. Montoya, M. Garcia-Mota, J. K. Nørskov and A. Vojvodic, *Physical Chemistry Chemical Physics*, 2015, **17**, 2634–2640.

[42] A. Kushima, S. Yip and B. Yildiz, *Physical Review B*, 2010, **82**, 115435.

[43] Y. Wang and H.-P. Cheng, *The Journal of Physical Chemistry C*, 2013, **117**, 2106–2112.

[44] Y. Lu, F. Lu, Z. Yang, J. Wu, H. Yu, X. Xie, J. Xu, F. Cheng, J. Chen, K. Xiong *et al.*, *AIP Advances*, 2016, **6**, 095210.

[45] L. Sacconi, *Pure Appl. Chem*, 1968, **17**, 95–127.

[46] A. Grimaud, K. J. May, C. E. Carlton, Y.-L. Lee, M. Risch, W. T. Hong, J. Zhou and Y. Shao-Horn, *Nature Communications*, 2013, **4**, 1–7.

[47] J. S. Yoo, Y. Liu, X. Rong and A. M. Kolpak, *The Journal of Physical Chemistry Letters*, 2018, **9**, 1473–1479.

[48] J. G. Lee, J. Hwang, H. J. Hwang, O. S. Jeon, J. Jang, O. Kwon, Y. Lee, B. Han and Y.-G. Shul, *Journal of the American Chemical Society*, 2016, **138**, 3541–3547.

[49] J. Rossmeisl, A. Logadottir and J. K. Nørskov, *Chemical Physics*, 2005, **319**, 178–184.

[50] B. Han, V. Viswanathan and H. Pitsch, *The Journal of Physical Chemistry C*, 2012, **116**, 6174–6183.

[51] P. Bothra and S. K. Pati, *ACS Energy Letters*, 2016, **1**, 858–862.

[52] W. T. Hong, M. Risch, K. A. Stoerzinger, A. Grimaud, J. Suntivich and Y. Shao-Horn, *Energy & Environmental Science*, 2015, **8**, 1404–1427.

[53] I. C. Man, H.-Y. Su, F. Calle-Vallejo, H. A. Hansen, J. I. Martinez, N. G. Inoglu, J. Kitchin, T. F. Jaramillo, J. K. Nørskov and J. Rossmeisl, *ChemCatChem*, 2011, **3**, 1159–1165.

[54] S. Gupta, W. Kellogg, H. Xu, X. Liu, J. Cho and G. Wu, *Chemistry–An Asian Journal*, 2016, **11**, 10–21.

[55] J. K. Nørskov, T. Bligaard, J. Rossmeisl and C. H. Christensen, *Nature Chemistry*, 2009, **1**, 37–46.

[56] J. Greeley, I. Stephens, A. Bondarenko, T. P. Johansson, H. A. Hansen, T. Jaramillo, J. Rossmeisl, I. Chorkendorff and J. K. Nørskov, *Nature Chemistry*, 2009, **1**, 552–556.

[57] J. Adler and I. Parmryd, *Cytometry Part A*, 2010, **77**, 733–742.

[58] T. Zhou, Z. Cao, P. Zhang, H. Ma, Z. Gao, H. Wang, Y. Lu, J. He and Y. Zhao, *Scientific Reports*, 2017, **7**, 46154.

[59] W. Tang, E. Sanville and G. Henkelman, *Journal of Physics: Condensed Matter*, 2009, **21**, 084204.

3

Potassium Cobalt Pyrophosphate $K_2CoP_2O_7$: as a Nonprecious and Efficient Bifunctional Electrocatalyst for Metal-Air Battery

3.0.1 Introduction

One of the most important ways to meet the ever increasing demands of global energy is improving the energy storage systems. Rechargeable or secondary lithium-ion batteries (LIBs) are dominating in this storage sector but it is phasing geopolitical stability. Also, Li abundance in the Earth crust is less than 20 ppm which has led the scientific community to explore alternative batteries such as sodium-ion batteries (SIBs), potassium-ion batteries (KIBs) and zinc-ion batteries (ZIBs) due to its earth abundance.[1–4] Along with the secondary batteries various other types of energy conversion and storage systems share good market values such

as fuel cells, supercapacitors and rechargeable metal-air batteries. In the recent years, rechargeable metal-air batteries are able to meet the continuous growing demand due to the high capacity delivered by such systems. In fact, these have applications towards smart-grid energy storage and electric vehicle propulsion. Tremendous research and developments are on the way to enhance the efficiency of catalysts which are crucial components in energy conversion of electricity into fuels and chemicals.[5] In the present chapter, a novel catalyst with excellent bi-functional activity in alkaline medium for metal-air battery application has been proposed.

A rechargeable metal-air involves oxygen reduction reaction (ORR) and oxygen evolution reaction (OER) electrochemical reactions, corresponding to the discharging and charging processes, respectively. Interestingly, this requires the same material to perform both the reactions and hence offering a very high energy density and stable discharge voltage[6–8]. This property is also known as bifunctionality and finding such a material is really an issue and remains the main bottleneck. The primary goal is to find such highly active catalysts who can prove its potential to replace existing state of the art catalysts for ORR and OER purpose[9,10]. In this work Co-based pyrophosphate system has been chosen based on previous reports, which showed phosphate based materials as efficient electrocatalysts. A dozen of materials like transition metal alloys, oxides/hydroxides/oxyhydroxides, nitrides, phosphides, sulfides and selenides have been reported and studied, which suggests them to perform only a half-reaction either ORR or OER and a very few for both[11–16]. There are a few other transition metals-based phosphate moieties, which exhibit bifunctionality[17–21]. In this work, $K_2CoP_2O_7$ has been synthesized and for the first time has been used in both K-ion battery and Zn-air battery. Earlier observation suggests that presence of Co-based catalyst in spinel structure Co_3O_4 shows bifunctionality; here the activity is inversely proportional to the co-ordination of Co. In fact, with proper theoretical modelling, it has been found to

be a good model system with efficient bifunctionality.

3.0.2 Theoretical Modelling:

All theoretical calculations were carried out in Quantum Espresso 6.2.0[22,23] considering plane wave basis of energy cut off 30 Ry and density cut off 300 Ry. Rappe Rabe Kaxirus Joannopoulas ultrasoft pseudopotential[24] was considered along with generalized gradient approximation parameters by Perdew, Burke and Ernzerhof (GGA-PBE)[25,26] for exchange-correlation functional. A 1×1 3d slab was considered with 15 Å vacuum along the z-direction. The Hubbard U parameter (GGA+U) of 3.32 eV was considered for the Co atoms. The whole system was sampled by $4 \times 4 \times 1$ uniform k-point mesh. For projected density of states (pDOS) calculation was carried out on $12 \times 12 \times 1$ k-point mesh.

3.0.3 Results and Discussions:

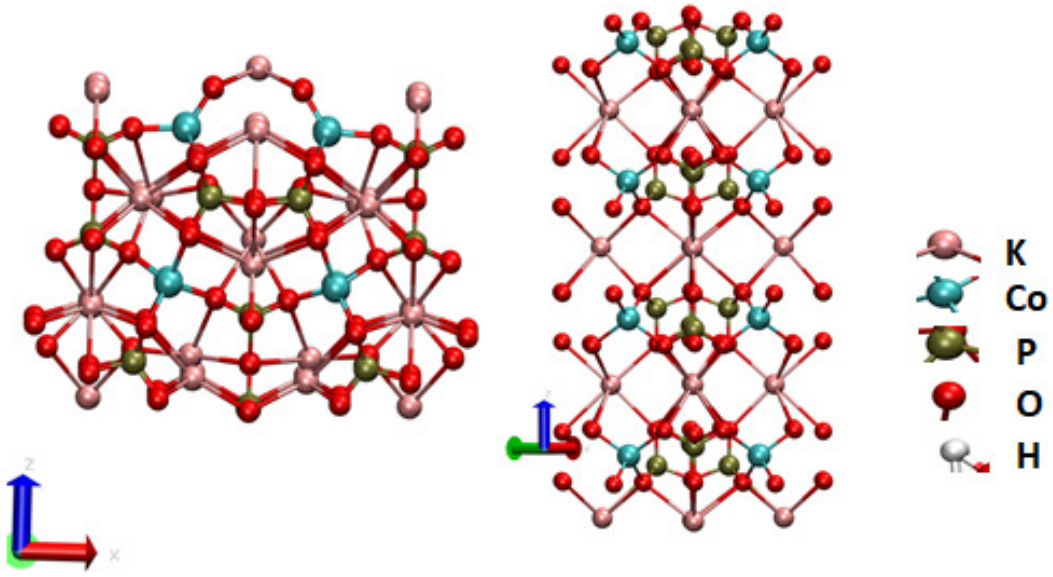

Figure 3.1: Left side: [110] surface; right side: [001] surface of $K_2CoP_2O_7$

Structural analyses:

Gabelica Robert first synthesized twisted-melilite $K_2CoP_2O_7$(P42/mnm) in 1981 [27]. Here the structure is synthesized via solution combustion method with unit cell parameters in the range of a = b $\sim$ 7.3 – 8.6 Å and c $\sim$ 4.8–5.6 Å . It contains vertex-sharing CoO_4 and PO_4 tetrahedra units arranged in a sheet-like framework. Each PO_4 tetrahedra combine to from P_2O_7 units. In each sheets covalent interactions exist among K-atoms and Os of CoO_4 and PO_4 tetrahedra. Our experimental

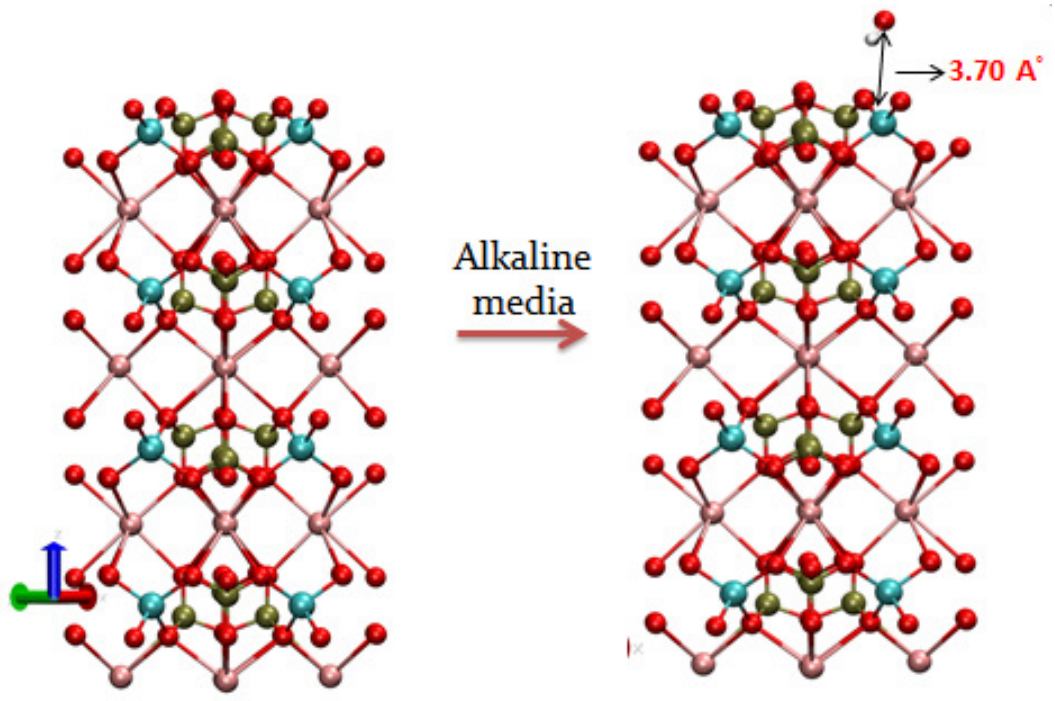

Figure 3.2: Interation of OH* adsorbate on [001] plane of $K_2CoP_2O_7$

collaborators could not detect the active surface of their system and hence we considered the commonly occurring low index surfaces, [110], [101] and [001] (the latter two are shown in Fig. 3.2). Among these, [101] plane, even though was found to be active for $Na_2CoP_2O_7$ was discarded in $K_2CoP_2O_7$ due to improper ratio of P:O ratio (7:25) in contrast to the experimental one (2:7). Since the reaction is carried out in alkaline medium, we first considered adsorption of OH intermediate

[110]-surface	Co-surf O(1)	Co-surf O(2)	Co-surf O(3)	Co-bulk O(4)
Pristine	1.68	1.92	2.09	**2.22**
OH	1.69	1.98	2.07	**3.52**
O	1.68	1.92	1.96	**3.54**
OOH	1.66	1.90	2.02	**3.48**
OO	1.66	1.91	1.99	**3.38**

Table 3.1: Change in the four Co-O bond lengths of active-tetrahedral Co-center of $K_2CoP_2O_7$.

on each of these low index surfaces. For [001] plane, we found a very low propensity of OH towards Co atom, which is shown in figure 2, based on which we did not consider this surface further. Finally, we considered [110] surface. The bulk $K_2CoP_2O_7$ has 4-coordinated Co atoms with symmetric bonds. However, in the [110] surface exposed Co atoms have highly distorted tetrahedral structure, which is observed from the four different Co-O bond lengths compared to symmetry in the bulk structure. As is clear from the earlier studies, OER activity is directly dependent on the geometry of Co. Yonfu Sun et al have already shown the importance of coordination of Co in water oxidation reaction [28,29], where tri-coordinated Co exhibits better activity compared to tetra- and penta-coordinated Co. In our case, the three Co-O bonds, which are exposed to surface is comparatively shorter than the one which is present in the bulk side. Interestingly, with the progress of the reaction, where the three surface Co-O distances remain almost the same as the pristine structure, while the fourth one Co-O bond shows an increase of nearly $\sim$1.3 Å. All the bond lengths are given in Table 1.

ORR:

Experimentally, they found the system to exhibit good ORR. The reason behind superior activity of $K_2CoP_2O_7$ is explored through our theoretical calculations.

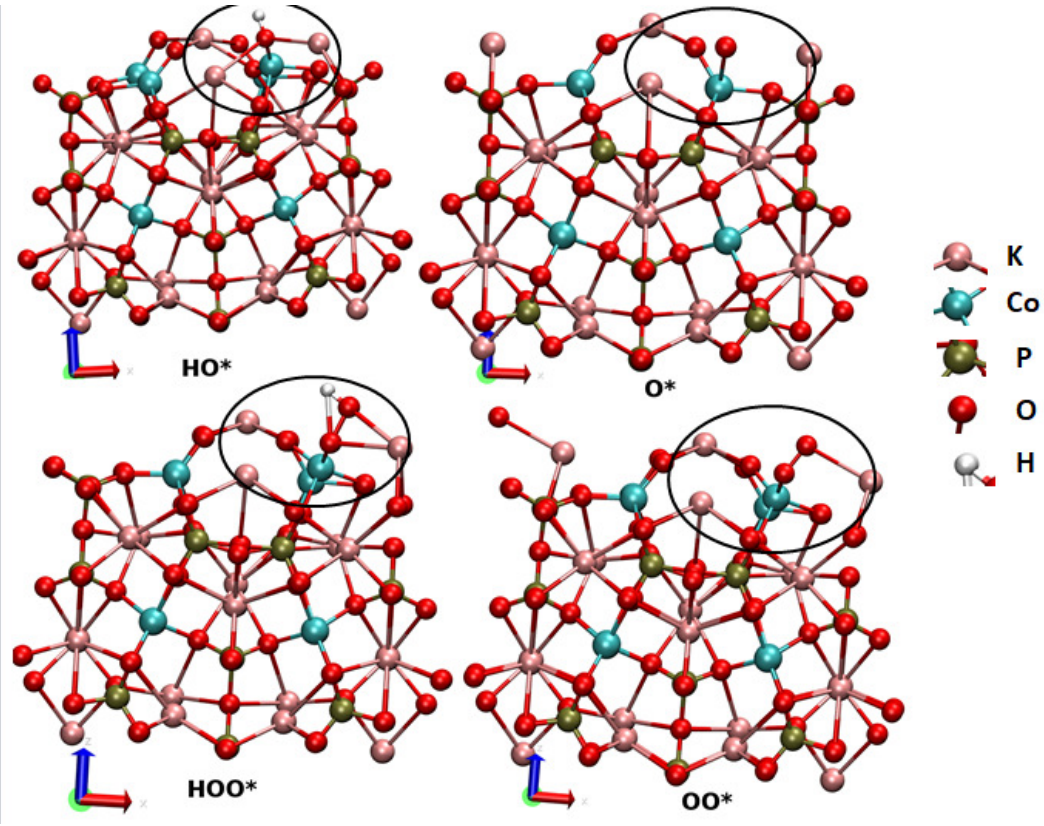

Figure 3.3: Stabilized intermediates

To understand the ORR mechanism in alkaline medium (0.1 M KOH, pH=13), four elementary steps have been modeled as follows:

1. $HO^* + O_2 + e^- \longrightarrow OO^* + OH^-$

   $U_1^\circ = \Delta G(HO^*) + \Delta G(O_2) - \Delta G(OO^*) + (e^- - OH^-) + eU$

2. $OO^* + H_2O + e^- \longrightarrow HOO^* + OH^-$

   $U_2^\circ = \Delta G(OO^*) + \Delta G(H_2O) - \Delta G(HOO^*) + (e^- - OH^-) + eU$

3. $HOO^* + e^- \longrightarrow O^* + OH^-$

   $U_3^\circ = \Delta G(HOO^*) - \Delta G(O^*) + (e^- - OH^-) + eU$

4. $O^* + H_2O + e^- \longrightarrow HO^* + OH^-$

   $U_4^\circ = \Delta G(O^*) + \Delta G(H_2O) - \Delta G(HO^*) + (e^- - OH^-) + eU$

ΔG_1	ΔG_2	ΔG_3	ΔG_4
1.22	1.49	1.08	1.17

Table 3.2: ΔG values for four steps of ORR (in eV).

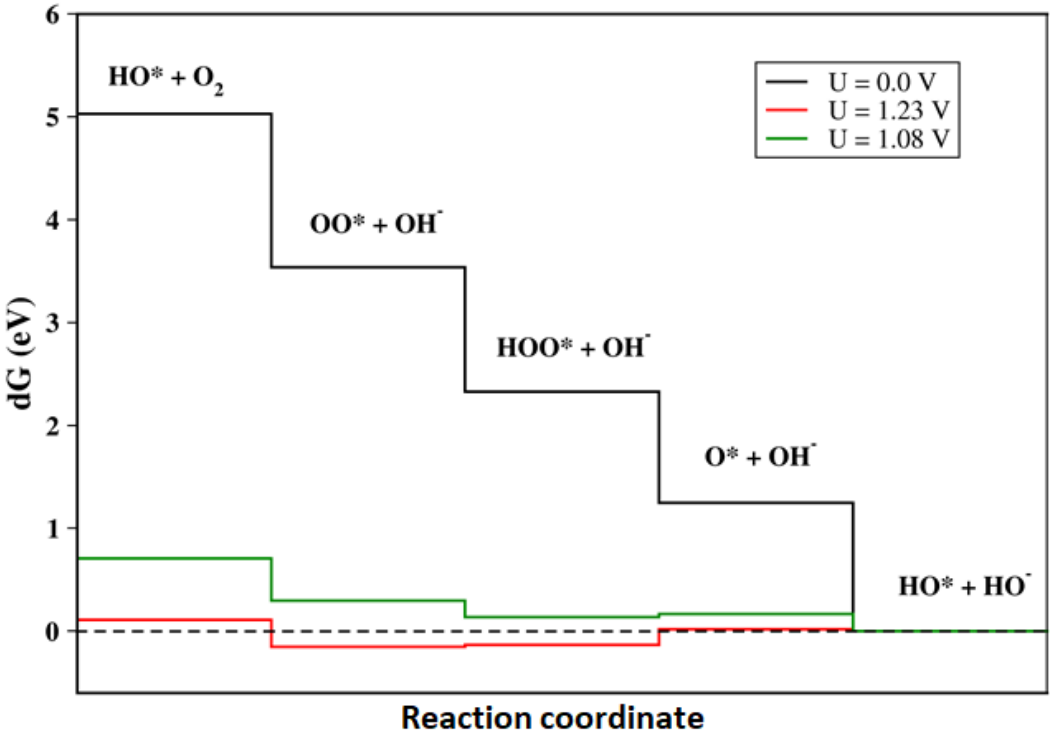

Figure 3.4: Free energy plot of ORR on the [110] surface at pH 13.0

Here * denotes the active site attached to surface. ΔG_x are the free energies of each step calculated by $\Delta G = \Delta E + \Delta ZPE - T\Delta S$ equation. The four equilibrium potentials U_x° ($\Delta G_x/e$) are obtained from the above equations. We have calculated Gibbs free energies for each of the steps. The electronic energies were obtained from the density functional theory-based calculations. The entropy contributions of the intermediates (OH*, OOH*, O*, H_2O and H_2) were taken from a previous paper based on perovskite. We have considered the implicit solvent model, where the energy of ions in solvent was included in the entropy value of water.

The energy of each step is calculated by considering computational hydrogen

electrode model (CHE)[30,31] of Norskov et al. This model involves a concerted transfer of OH^- and e^- in each step. The catalytic activity which is expressed in terms of overpotential is calculated as follows:

$$\eta = 1.23 - min(\Delta G_1, \Delta G_2, \Delta G_3, \Delta G_4) \tag{3.1}$$

After extensive analysis of all the Gibbs potentials, we find that the fourth step i.e. formation of HO*, where the Co oxidation state is changed from +4 to +3 state is the rate-determining step. It is because the formation of HO* partially disrupts perfect bonding features of Co-O bond, as this bond length elongates from 1.71 to 1.93 A. The overpotential value was found to be 0.15 V. The lower overpotential for ORR is attributed to the fact that the formation of HO* intermediate is more facile in the presence of two adjacent K atoms on the surface. However, the perfect 100% accessibility of this surface with two K ions participating in stabilizing the OH intermediate may not be feasible experimentally. We believe, because of this experimentally they did not find such lower overpotential value.

OER:

The OER activity of the proposed material has been checked in 0.1 M KOH against Hg/HgO reference electrode. Interestingly, most of the catalysts are found to be active in the higher concentration of base (1M KOH) including benchmark catalyst RuO_2. Here also the activity is compared with RuO_2, $Na_2CoP_2O_7$ and $NaCoPO_4$. 200 cycles have been considered in a cyclic voltammogram to check the stability of OER activity. Similar to other phosphate systems, two pairs of redox peaks were observed associated with Co^{3+}/Co^{2+} and Co^{4+}/Co^{3+} conversion.[21,28,29]

We also have modeled the same system to find the OER mechanism in alkaline medium.

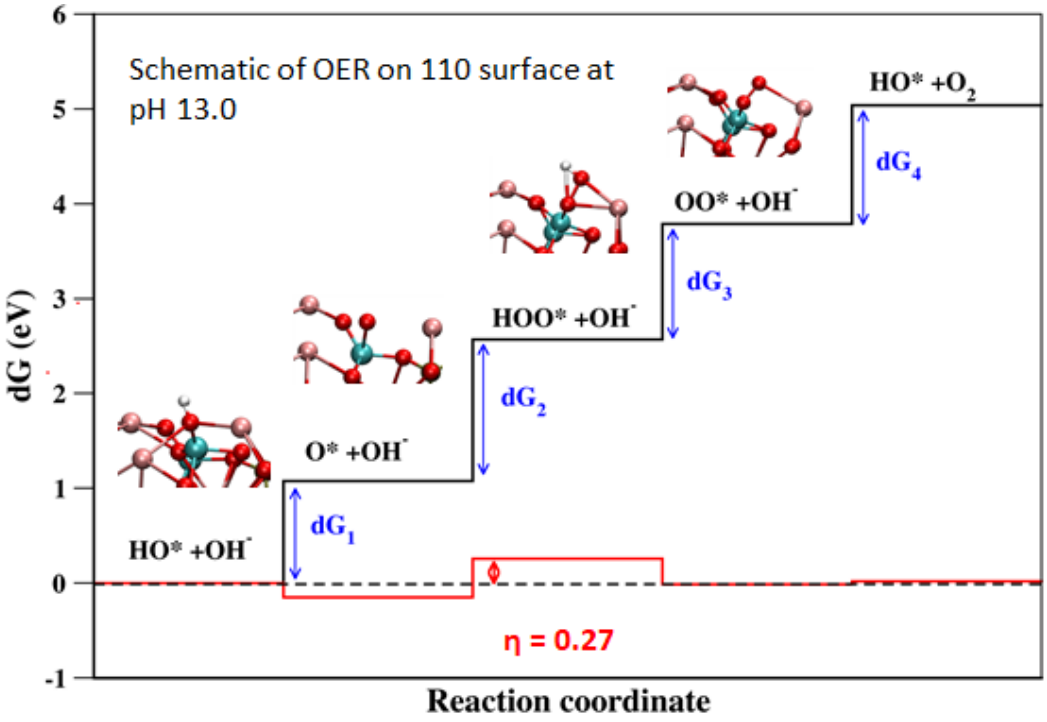

Figure 3.5: Free energy plot of OER on the [110] surface at pH 13.0

1. $HO^* + OH^- \longrightarrow O^* + H_2O + e^-$

   $U_1^\circ = \Delta G(HO^*) - \Delta G(O^*) - \Delta G(H_2O) - (e^- - OH^-) - eU$

2. $O^* + OH^- \longrightarrow HOO^* + e^-$

   $U_2^\circ = \Delta G(O^*) - \Delta G(HOO^*) - (e^- - OH^-) - eU$

3. $HOO^* + OH^- \longrightarrow OO^* + H_2O + e^-$

   $U_3^\circ = \Delta G(HOO^*) - \Delta G(OO^*) - \Delta G(H_2O) - (e^- - OH^-) - eU$

4. $OO^* + OH^- \longrightarrow HO^* + O_2 + e^-$

   $U_4^\circ = \Delta G(OO^*) - \Delta G(HO^*) - \Delta G(O_2) - (e^- - OH^-) - eU$

$$\eta = max(\Delta G_1, \Delta G_2, \Delta G_3, \Delta G_4) + 1.23eV \tag{3.2}$$

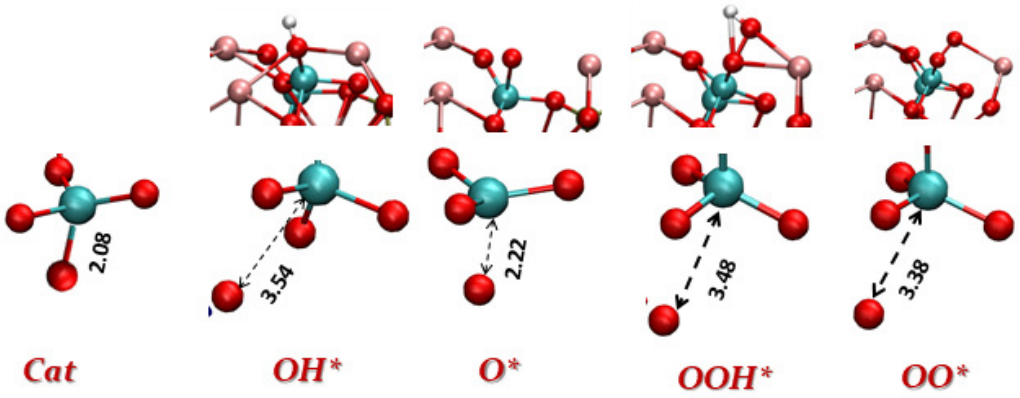

Figure 3.6: Variation in coordination of active Co-center during the reaction

It is well known that the water oxidation reaction (OER) is favorable on the surfaces with low coordinated active site, since such a site favors the *OH binding probability. We have studied the OER activity on the [110] surface, as this favors the coordination of *OH intermediate in alkaline condition. Interestingly, during the reaction, the Co center remains effectively tetra coordinated rather than penta coordinated which is well depicted by figure 6. In reality, Co-O bond (one in the bulk side) gets elongated as the oxygen (bulk) moves away making room for the intermediate to bond. So, during interaction with the reactant or intermediates, Co-center is actually tri-coordinated, which falls inline with the previous observation of tri-coordinated Co-center showing better catalytic activity.

Such flexibility in the bonding is again due to the highly stable P_2O_7 unit which allows rotations, which was also observed experimentally. Along with these, a significant non-covalent type of interaction is found with the nearby K atom, which provides extra stability to the intermediate structures. However, this interaction varies depending on the nature and orientation of intermediates. These two points, namely, effectively tetra-coordination and cooperative interaction with K further strengthen the propensity of stability of OH in [110] in comparison to [001] plane (where no K atom is present). The rate-determining step in [110] surface

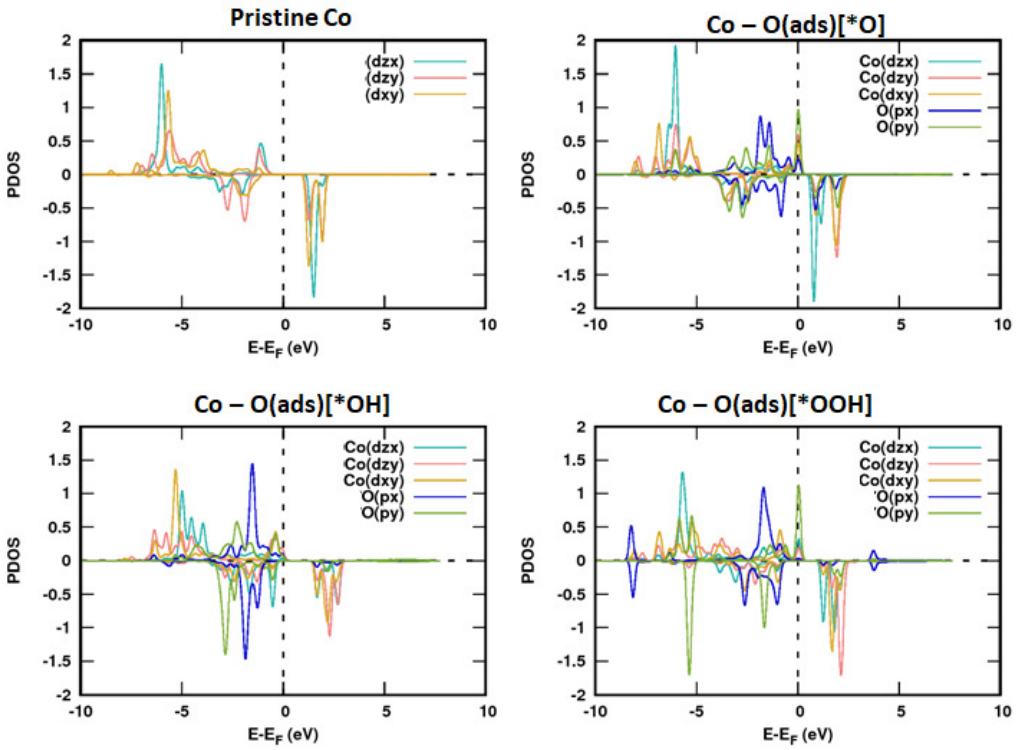

Figure 3.7: The 1st plot in pDOS correspond to only the t_2 orbitals of Co (active one) on which intermediates are getting adsorbed. The 2nd, 3rd and 4th plots correspond to the pDOS plot of adsorbed intermediates O, OH and OOH respectively, along with Co t_2 orbitals.

of $K_2CoP_2O_7$ is found to be the formation of O-O bond (in HOO* intermediate), which involves reduction of Co from +4 to +3. Finally, analyzing the Gibbs free energy values of all the steps and the rate-determining step, we find the overpotential for the OER process to be 0.26 V. This is close to the experimental value. It is also to be noted that the Co reduction (from +4 to +3) also has been found experimentally. The main point is that the Co reduction induces d-electrons in the crystal field, thereby playing a very important role in the OER.

The electronic analyses have been carried out with the help of pDOS analyses (Fig. 5.5) of each intermediates. The t_2 orbitals are found to be present on the Fermi levels, which help in exhibiting good catalytic activities.

3.0.4 Conclusion:

Experimentally potassium based pyrophosphate was successfully synthesized and first time investigated as a bi-functional catalyst. Our theoretical analyses have found [110] plane to be the active surface in contrast to the Na-analogue, where [101] plane is the active one. The theoretical modelling of ORR/OER are done considering alkaline medium. The catalyst has showed excellent stability due to pyrophosphate linkages, which is also found through the theoretical calculation. Theoretical analyses suggest that the flexibility in Co-O bond of $K_2CoP_2O_7$ is the reason behind its excellent activity as bifunctional catalyst.

References

[1] N. Yabuuchi, K. Kubota, M. Dahbi and S. Komaba, *Chemical Reviews*, 2014, **114**, 11636–11682.

[2] K. Kubota, M. Dahbi, T. Hosaka, S. Kumakura and S. Komaba, *The Chemical Record*, 2018, **18**, 459–479.

[3] A. Eftekhari, *Journal of Power Sources*, 2004, **126**, 221–228.

[4] M. Song, H. Tan, D. Chao and H. J. Fan, *Advanced Functional Materials*, 2018, **28**, 1802564.

[5] Z. W. Seh, J. Kibsgaard, C. F. Dickens, I. Chorkendorff, J. K. Nørskov and T. F. Jaramillo, *Science*, 2017, **355**, year.

[6] G. Girishkumar, B. McCloskey, A. C. Luntz, S. Swanson and W. Wilcke, *The Journal of Physical Chemistry Letters*, 2010, **1**, 2193–2203.

[7] J.-S. Lee, S. Tai Kim, R. Cao, N.-S. Choi, M. Liu, K. T. Lee and J. Cho, *Advanced Energy Materials*, 2011, **1**, 34–50.

[8] M. K. Debe, *Nature*, 2012, **486**, 43–51.

[9] D. Schonvogel, J. Hülstede, P. Wagner, A. Dyck, C. Agert and M. Wark, *Journal of The ElectroChemical Society*, 2018, **165**, F3373.

[10] Y. Lee, J. Suntivich, K. J. May, E. E. Perry and Y. Shao-Horn, *The Journal of Physical Chemistry Letters*, 2012, **3**, 399–404.

[11] Y. Hou and M. Lohe, *Energy & Environmental Science*, 2016, **9**, 478–483.

[12] J. Zhang, T. Wang, D. Pohl, B. Rellinghaus, R. Dong, S. Liu, X. Zhuang and X. Feng, *Angewandte Chemie*, 2016, **128**, 6814–6819.

[13] J. Wang and H. Zhong, *ACS Nano*, 2016, **10**, 2342–2348.

[14] H. Zhong, J. Wang, F. Meng and X. Zhang, *Angewandte Chemie*, 2016, **128**, 10091–10095.

[15] F. Dionigi and P. Strasser, *Advanced Energy Materials*, 2016, **6**, 1600621.

[16] B. Zhang, X. Zheng, O. Voznyy, R. Comin, M. Bajdich, M. García-Melchor, L. Han, J. Xu, M. Liu, L. Zheng *et al.*, *Science*, 2016, **352**, 333–337.

[17] H. Wan, R. Ma, X. Liu, J. Pan, H. Wang, S. Liang, G. Qiu and T. Sasaki, *ACS Energy Letters*, 2018, **3**, 1254–1260.

[18] Y. Liu, H. Wang, D. Lin, C. Liu, P.-C. Hsu, W. Liu, W. Chen and Y. Cui, *Energy & Environmental Science*, 2015, **8**, 1719–1724.

[19] Y. Zhan, S. Yang, M. Lu, Z. Liu and J. Y. Lee, *Electrochimica Acta*, 2017, **227**, 310–316.

[20] H. Kim, J. Park, I. Park, K. Jin, S. E. Jerng, S. H. Kim, K. T. Nam and K. Kang, *Nature Communications*, 2015, **6**, 1–11.

[21] R. Gond, K. Sada, B. Senthilkumar and P. Barpanda, *ChemElectroChem*, 2018, **5**, 153–158.

[22] P. Giannozzi, S. Baroni, N. Bonini, M. Calandra, R. Car, C. Cavazzoni, D. Ceresoli, G. L. Chiarotti, M. Cococcioni, I. Dabo *et al.*, *Journal of Physics: Condensed Matter*, 2009, **21**, 395502.

[23] T. A. Barnes, T. Kurth, P. Carrier, N. Wichmann, D. Prendergast, P. R. Kent and J. Deslippe, *Computer Physics Communications*, 2017, **214**, 52–58.

[24] A. M. Rappe, K. M. Rabe, E. Kaxiras and J. Joannopoulos, *Physical Review B*, 1990, **41**, 1227.

[25] M. Ernzerhof and G. E. Scuseria, *The Journal of Chemical Physics*, 1999, **110**, 5029–5036.

[26] C. Adamo and V. Barone, *The Journal of Chemical Physics*, 1999, **110**, 6158–6170.

[27] M. Sale, M. Avdeev, Z. Mohamed, C. D. Ling and P. Barpanda, *Dalton Transactions*, 2017, **46**, 6409–6416.

[28] Y. Sun, S. Gao, F. Lei and Y. Xie, *Chemical Society Reviews*, 2015, **44**, 623–636.

[29] J. B. Goodenough, R. Manoharan and M. Paranthaman, *Journal of the American Chemical Society*, 1990, **112**, 2076–2082.

[30] J. K. Nørskov, J. Rossmeisl, A. Logadottir, L. Lindqvist, J. R. Kitchin, T. Bligaard and H. Jonsson, *The Journal of Physical Chemistry B*, 2004, **108**, 17886–17892.

[31] J. H. Montoya, M. Garcia-Mota, J. K. Nørskov and A. Vojvodic, *Physical Chemistry Chemical Physics*, 2015, **17**, 2634–2640.

4

Na_2MPO_4F (M = Fe, Co, Mn): Alkali Metal Fluorophosphates as Efficient Bifunctional Electrocatalysts for Oxygen Evolution and Reduction Reaction

4.0.1 Introduction:

From the previous chapter, we have already learnt about the crucial role of metal-air batteries to the society and also the necessity of improving catalytic activities for water splitting/ oxygen reduction in this regard. These reactions are widely known to be kinetically sluggish due to involvement of four ($H^+ + e^-$). The commercially used catalysts for these two reactions are comprised of costly, scarce noble metals and hence demands for eco-friendly, economical and efficient cata-

lysts. Till date phosphate-based and phosphate-derived systems are found to show good activity along with stability as a bifunctional catalysts and specifically with the 3d transition metals[1–3], which encourages a further probe in this direction. Gorlin and Jaramillo[4] have found that $Mn_3(PO_4)_2$ shows better OER activity due to PO_4 framework which stabilize high oxidation state of Mn(3+) require for better activity. Similarly, sodium cobalt phosphates found to be excellent bifunctional catalyst[5]. So, different observation suggests the presence of phosphate group has been proved to enhance the catalytic activity. Cao *et. al.*[6] have synthesized sodium fluorophosphate, later Barpanda *et. al.*[7] used Na_2CoPO_4F as an efficient bifunctional electrocatalyst. This result has intrigued the latter group to compare the electrocatalytic activity of Na_2CoPO_4F with Na_2MnPO_4F (NMPF) and Na_2FePO_4F (NFPF). Where NFPF is considered as a cathode system for both Li- and Na-ion based secondary batteries, other two systems are considered only for Na-based sytems. Though the three systems share the chemical formula but not the same crystallographic structures (the figures are shown in Fig. 4.1). NMPF crystallizes in monoclinic structure and NCPF, NFPF in orthorhombic. The influence of crystal structures on catalytic properties has been unravelled with the help of density functional based theoretical studies. Various post-mortem analyses have assured about the stability of materials.

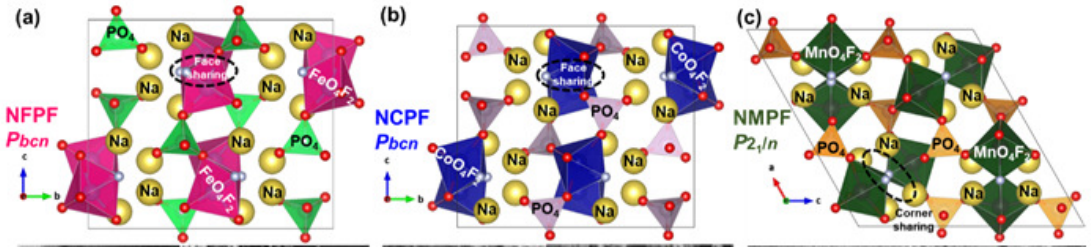

Figure 4.1: Crystallographic structures of (a) Na_2FePO_4F, (b) Na_2CoO_4F and (c) Na_2MnPO_4F

4.0.2 Density functional theory:

We have done electronic and structural analyses of the catalytic cycles of each fluorophosphate systems (Na_2MPO_4F; M = Mn, Co, Fe) with the help of density functional based theoretical analyses. We have considered Quantum Espresso 6.1 [8,9] with a plane wave basis of density cut off 300 Ry and energy cut off 30 Ry. The considered exchange-correlation functional is generalized gradient approximation based by Perdew, Burke & Ernzerhof (GGA-PBE) [10,11] with an ultrasoft pseuodopotential by Rappe, Rabe, Kaxiras, Joannopoulos [12] for NMPF and NCPF and Vanderbilt pseudopotential [13] for NFPF. The choice of surfaces [100] plane for NFPF and NCPF; [010] for NMPF is justified later in the structural analyses section. The corresponding supercells are big enough to prevent interactions among its reactants (considering the systems to be periodic in two directions). $2 \times 1 \times 1$ 3d slabs with 15 Åvacuum along x-direction and $1 \times 2 \times 1$ with 15Åvacuum along y-direction are considered for NFPF, NCPF and NMPF respectively. The k-point mesh considered for the first two systems is $1 \times 4 \times 4$ and for third one is $4 \times 1 \times 4$. In case of projected density of states (pDOS) calculation, $1 \times 8 \times 8$ k-point mesh points are considered for the first two systems while $8 \times 1 \times 8$ for the third one.

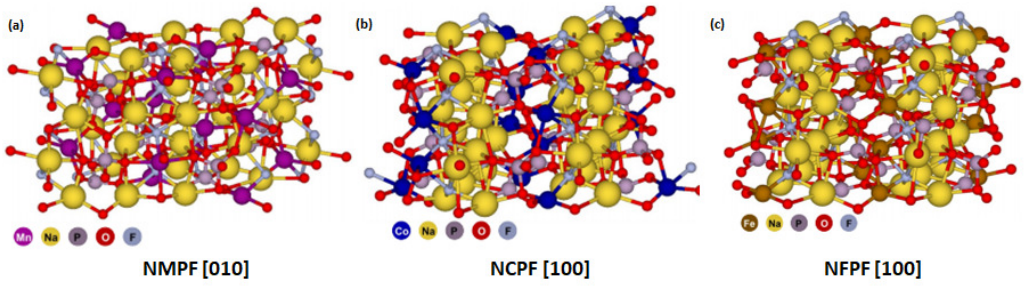

Figure 4.2: Theoretically optimized structures of (a)[010] Na_2MnPO_4F; (b)[100] Na_2CoPO_4F and (c) [100] Na_2FePO_4F.

4.0.3 Result and discussions:

Structural analyses:

All the systems have been synthesized in Prof. Barpanda's group using their lab protocol and previous work[14,15], i.e. solution combustion route by Barpanda and colleague. Through powder x-ray diffraction pattern, structure was analyzed and NCPF and NFPF have found to be layered orthorhombic structure with Pbcn space group. The structure resembles with Na_2MgPO_4F structure[16] layered orthorhombic structure and Pbcn space group. The structure has adjacent face sharing MO_4F_2 octahedra subunits connected via F atom to form $M_2O_7F_2$ bioctahedra unit. So, these units are alligned along x-axis connected via F atoms and further interconnected tetrahedra phosphate unit along z-axis again to form a layered structure with a pair of different crystallographic sites of Na. On the contrary, NMPF belongs to P21/n space group, with eight formula units of four different types of Na-atoms. Here also bi-octahedra $Mn_2O_8F_2$ are formed by connecting two MnO_4F_2 unit through F atom. Again, with the help of tetrahedra phosphate groups along x- and z- directions, the structure has 3d tunneled framework.

We have begun the theoretical calculation by analyzing the plane of all three systems, where all these reactions occur within a normal reaction conditions and are facile. After extensive computations for each of the systems and with number of surfaces, we find that the effective surfaces are [100], [100] and [010] for NCPF, NFPF and NMPF respectively (shown in Fig. 4.2). The other possible low energy surfaces have been discarded mainly because of the unavailability of the active cite on the surface or being covered by the other coordinations. Such surfaces of each system are shown in Fig. 4.3.

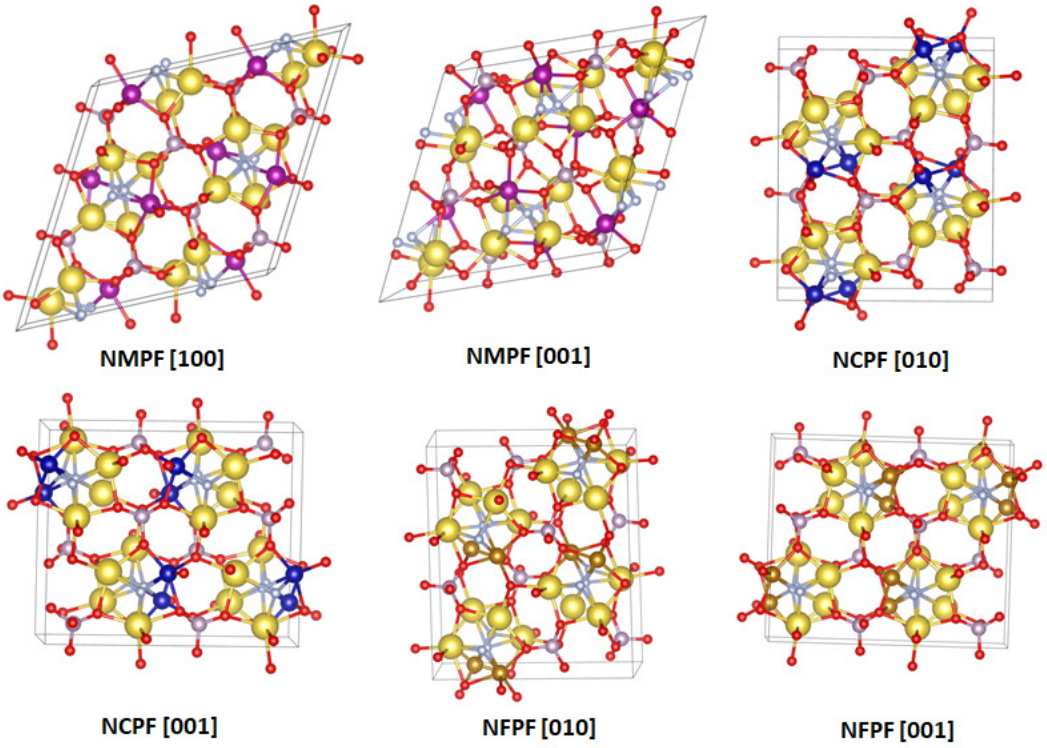

Figure 4.3: Crystallographic structures of the planes.

Electrocatalytic measurement:

Experimentally, the ORR and OER activity were carried out using three-electrode setup with Hg/HgO (1M NaOH) as reference electrode, Pt wire as counter electrode and RRDE coated with slurry acted as working electrode. From cyclic voltammogram, the onset potentials of NMPF and NFPF are found to be on more positive side compared to NCPF suggesting NCPF to be the more efficient catalyst. The catalytic activities of each systems are benchmarked against standard 20% Pt/C catalyst. Again the linear sweep voltammetry (LSV) shows the catalytic activity in the following order: NFPF < NMPF < NCPF with the onset potentials of 20% Pt/C, NFPF, NMPF and NCPF to be 0.948 V, 0.891 V, 0.909 V and 0.903 V respectively. Also, NCPF has similar half wave potential as 20% Pt/C with a better Taffel plot than the latter showing a good ORR activity of

NCPF.

The OER activity of the systems are standardized with respect to RuO_2, here also NCPF has outperformed the other two with the overpotential value of 0.38 V vs. RHE. While the rest two have shown larger overpotentials with poor current densities.

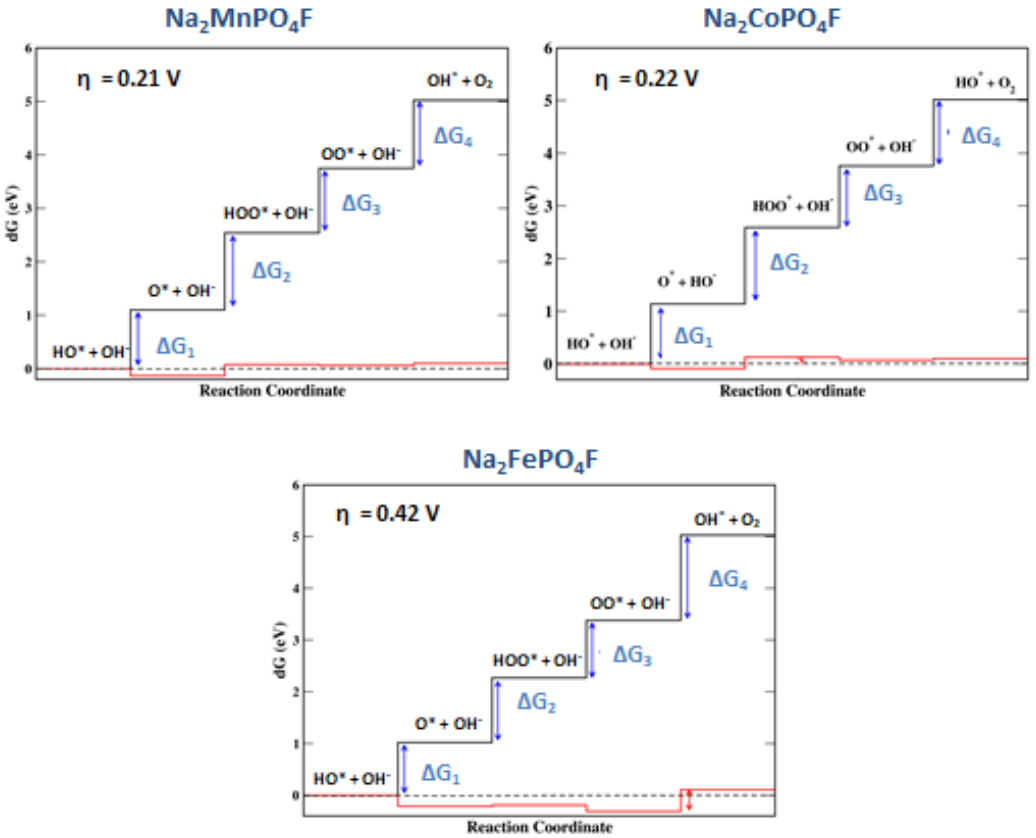

Figure 4.4: Step plots of OER for NMPF, NCPF and NFPF. The free energies are calculated using DFT approach

Theoretical Analyses:

OER

Since the reaction medium is alkaline medium with pH = 13.0, the steps associated with the OER are as follows:

1. $HO^* + OH^- \longrightarrow O^* + H_2O + e^-$
   $U_1^\circ = \Delta G(HO^*) - \Delta G(O^*) - \Delta G(H_2O) - (e^- - OH^-) - eU$

2. $O^* + OH^- \longrightarrow HOO^* + e^-$
   $U_2^\circ = \Delta G(O^*) - \Delta G(HOO^*) - (e^- - OH^-) - eU$

3. $HOO^* + OH^- \longrightarrow OO^* + H_2O + e^-$
   $U_3^\circ = \Delta G(HOO^*) - \Delta G(OO^*) - \Delta G(H_2O) - (e^- - OH^-) - eU$

4. $OO^* + OH^- \longrightarrow HO^* + O_2 + e^-$
   $U_4^\circ = \Delta G(OO^*) - \Delta G(HO^*) - \Delta G(O_2) - (e^- - OH^-) - eU$

$$\eta = max(\Delta G_1, \Delta G_2, \Delta G_3, \Delta G_4) + 1.23\ eV \tag{4.1}$$

The [100] plane of NCPF has four Co-atoms on the surface belonging to two different groups; one Co-center is penta-coordinated (three Co-O bonds and two Co-F bonds) and another one is hexa-coordinated with elongated Co-O bonds (four Co-O bonds and two Co-F bonds). Being in the alkaline medium, the active site for OER has been chosen based upon favorable adsorption of OH_- adsorbent. Our theoretical studies has found that Co-center with penta-coordination showing better activity compared to the other type of Co-centers. As penta-coordinated Co-centers has two stronger Co-F bonds (2.14 Å vs 2.41 Å) compared to hexa-coordinated Co-centers and bonding with the F-atoms increases ionicity of metal center helping in the facile bonding. This explains the minimal strain generation in the overall structure (due to very less changes in Co-O and Co-F bond lengths) with OH-adsorption. In case of NMPF as well moderate changes in the bond lengths have been found upon OH-adsorption. In case of NFPF, octahedral site is favorable one and adsorption of OH generates strain in the octahedra structure leading to structural disintegration. This rises a question on the stability of NFPF at the end of the cycle.

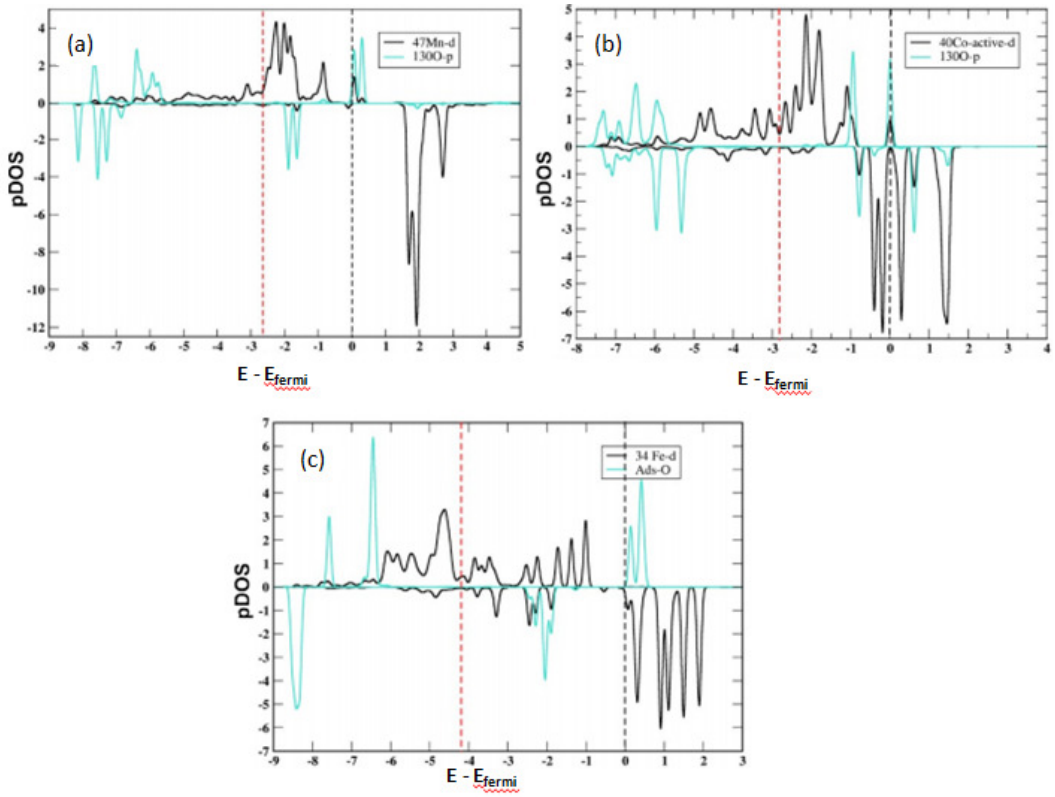

Figure 4.5: Density of states (DOS) of overlapping of d orbitals of 3-d transition metal atom and adsorbed oxygen atom for (a) Na_2MnPO_4F, (b) Na_2CoPO_4F and (c) Na_2MnPO_4F respectively.

Experimentally, our collaborators find that after one cycle, the NFPF structure deteriorates as found through TEM analysis. Interestingly, our analysis of OER overpotentials for all the three systems suggest that NCPF to be the best system and the order follows, NCPF > NMPF > NFPF in terms of OER activity being best to worst. The experimental observations also give the same trend in OER activity. Most importantly, the rate determining step (RDS) for OER for NMPF and NCPF is the second step (step 2) i.e. the formation of peroxide radical (*OOH) from oxide radical (*O) with the overpotential value of 0.21 V and 0.22 V respectively (as shown in the step plot in Fig. 4.4).

On the contrary replacement of adsorbed dioxygen (*OO) intermediate with hydroxide (*OH) is the RDS for NFPF with the overpotential value of 0.42 V. The

Materials	$\Delta G_1(eV)$	$\Delta G_2(eV)$	$\Delta G_3(eV)$	$\Delta G_4(eV)$
NMPF	1.13	1.45	1.16	1.28
NCPF	1.14	1.45	1.17	1.26
NFPF	1.02	1.25	1.11	1.65

Table 4.1: ΔG values of the four steps of NMPF, NCPF and NFPF for OER

possible degradation of the NFPF system after one cycle and the the exception in the RDS in the case of NFPF is due to low-lying empty d-band center in Fe 3d band. The details are explained by the d-band structure of the materials shown in Fig. 4.5.

Although all the 3d transition metals have narrow band widths and electronic degrees of freedom are localized, particularly Fe has a special band character. The conduction band of Fe is quite low lying and bottom of the conduction band in general lie quite low, which is below most of the anti-bonding molecular orbitals of molecules which are adsorbed on the surface. Due to this energy scenario, the electron reaches the low-lying conduction band of Fe, making a strong chemical bond with the Fe surface, thereby deteriorating the sample surface.

In the case of NFPF, the Fe 3d conduction band edge is quite lower in energy, due to which there is a charge transfer from the bonding molecular orbital of the adsorbed molecular species to the Fe surface. To find the extent of charge transfer to a surface, Nørskov et al have provided a d-band theory[17], which basically estimates how much the anti-bonding states are shifted up through the Fermi level (empty). In the case of NCPF, there is a significant overlap of the d-orbital of cobalt and the p-orbital of adsorbed oxygen. In fact, due to this, there is a formation of perfect octahedral structure in NCPF, which in turn gives rise to small Co-O bond distance and over all excellent bifunctional character to NCPF.

On the other hand, in case of NFPF system, the intermediate *OO (when adsorbed on Fe surface) is difficult to dissociate to replace it with *OH and thereby

giving rise to large overpotential for NFPF. Interestingly, in experimental system also the NFPF gets destroyed after one cycle, a proof of low-lying conduction band in Fe system.

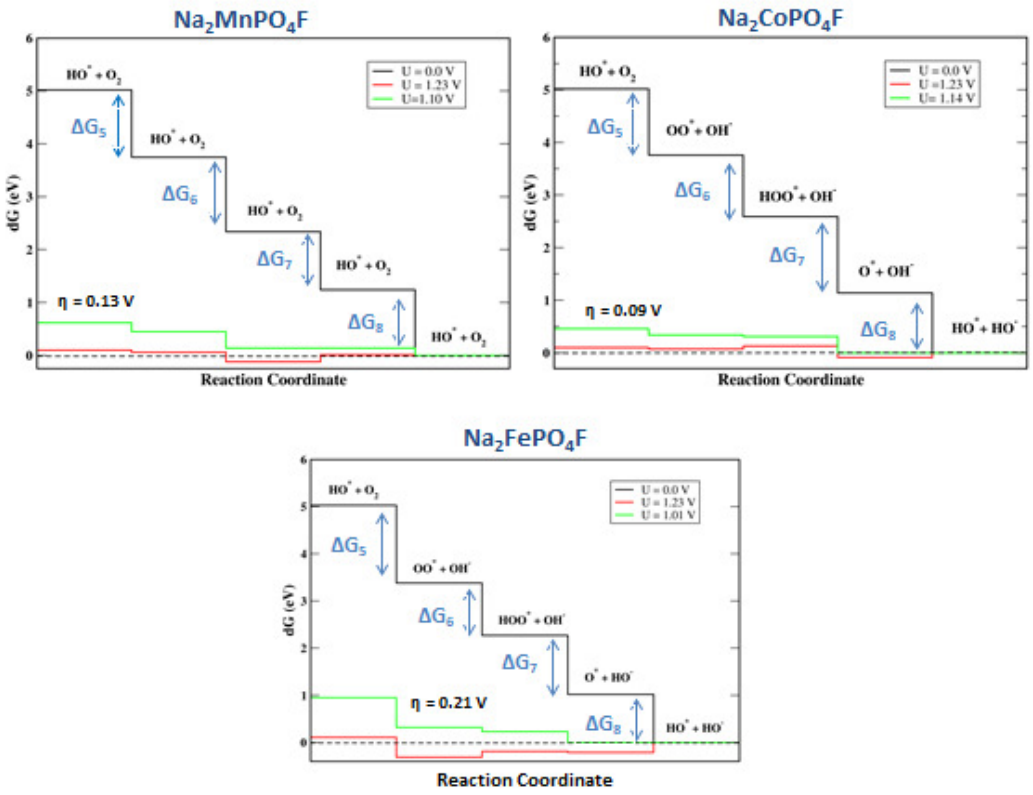

Figure 4.6: Step plots of ORR for NMPF, NCPF and NFPF. The free energies are calculated using DFT approach.

ORR

In alkaline media, the reaction steps for ORR are as follows:

5. $HO^* + O_2 + e^- \longrightarrow OO^* + OH^-$

   $U_1^\circ = \Delta G(HO^*) + \Delta G(O_2)$ - $\Delta G(OO^*) + (e^-$ - $OH^-) + eU$

6. $OO^* + H_2O + e^- \longrightarrow HOO^* + OH^-$

   $U_2^\circ = \Delta G(OO^*) + \Delta G(H_2O)$ - $\Delta G(HOO^*) + (e^-$ - $OH^-) + eU$

7. HOO* + e^- $\longrightarrow$ O* + OH^-
   U_3° = ΔG(HOO*) - ΔG(O*) + (e^- - OH^-) + eU

8. O* + H_2O + e^- $\longrightarrow$ HO* + OH^-
   U_4° = ΔG(O*) + ΔG(H_2O) - ΔG(HO*) + (e^- - OH^-) + eU

$$\eta = 1.23 - min(\Delta G_1, \Delta G_2, \Delta G_3, \Delta G_4) \tag{4.2}$$

Analysis of all the Gibbs free energy values along with the exact potential for ORR process, we find that the RDS is the final step, where *O (oxygen adsorbed on surface) is replaced with *OH (hydroxyl adsorbed on surface) for all the three systems. From RDS step data (in Fig. 4.6), we find the overpotential values of 0.10 V, 0.09 V and 0.21 V for NMPF, NCPF and NFPF, respectively. It corroborates with the experimental findings on the overpotential values; i.e., NCPF $\sim$ NMPF $>$ NFPF. Interestingly, the formation of OH* intermediate is the rate determining step for NFPF in either of the reactions (OER and ORR) and the underline reason is the same, i.e., huge distortion in the structure of NFPF upon OH^- adsorption.

Materials	$\Delta G_1(eV)$	$\Delta G_2(eV)$	$\Delta G_3(eV)$	$\Delta G_4(eV)$
NMPF	1.28	1.16	1.45	1.13
NCPF	1.26	1.17	1.45	1.14
NFPF	1.65	1.11	1.25	1.02

Table 4.2: ΔG values of the four steps of NMPF, NCPF and NFPF for ORR

Interestingly, experimentally the structures were analyzed in TEM after ORR cycles and it was found that NFPF system showed amorphization and disintegration of the sample surface while highest degree of crystallinity is retained by the NCPF sample. To find the structural stability of the three systems during the formation of *OH intermediate, we have shown the catalytic sites with its corre-

sponding bonds in the pristine state and after adsorbing OH^- in Fig. 4.7. This observation refers to the structural instability, particularly for NFPF (also found in TEM analysis experimentally).

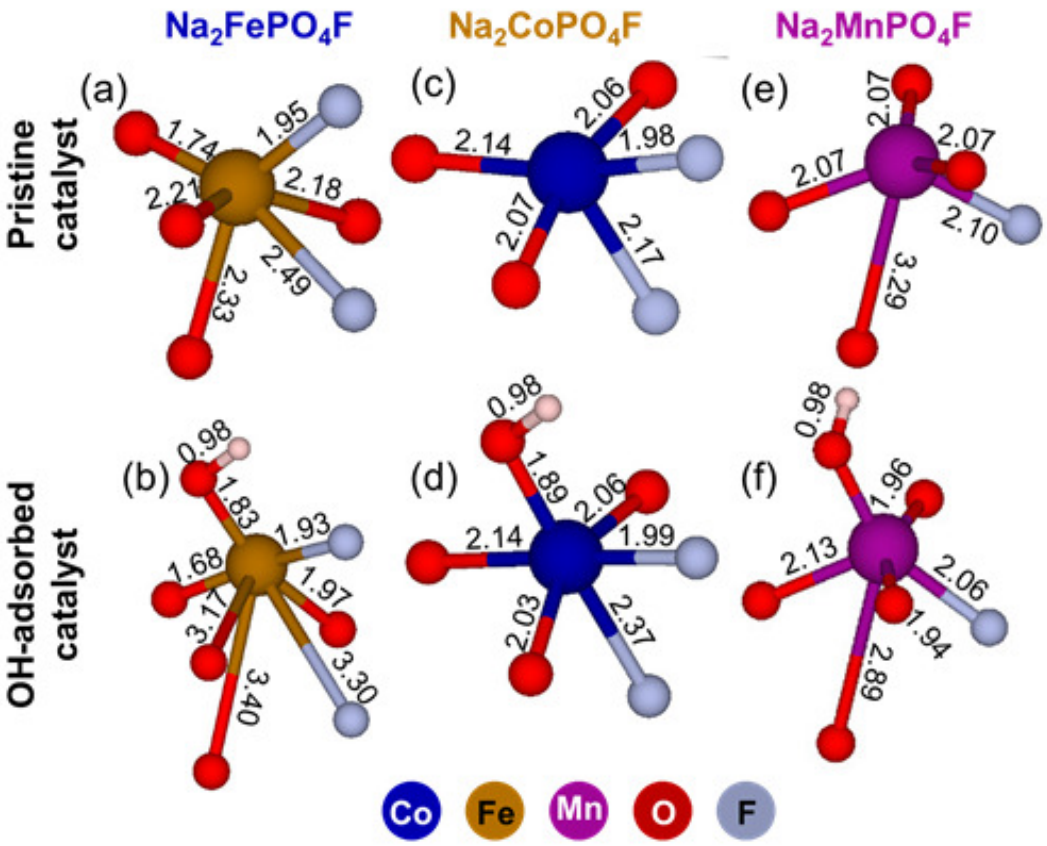

Figure 4.7: Local environment of the active metal centers of the [100] surface for the two systems, Na_2FePO_4F and Na_2CoPO_4F and the [010] surface for Na_2MnPO_4F; all the three systems in their pristine and OH-adsorbed states. As can be seen, there is a large change in the bond lengths upon OH adsorption for Na_2FePO_4F (a, b), which shows the structural instability upon the ORR and OER. As expected, there are minimal changes in the bond lengths upon OH adsorption, indicating high structural stability for Na_2CoPO_4F (c, d). For Na_2MnPO_4F (e,f), as can be seen there are moderate bond length changes. All the bond lengths mentioned in the figures are given in the units of Å.

4.0.4 Conclusions

Polyanionic transition metal-based sodium fluorophosphates, Na_2MPO_4F (M = Fe/Co/Mn), were first time explored as bifunctional electrocatalysts. Our the-

oretical calculation matches well with the experimentally observed ORR trend i.e. NCPF $\sim$ NMPF $>$ NFPF. In case of OER along with NCPF, NMPF is also found to exhibit equally good catalytic activity which contradicts the experimental observation of NMPF of showing highest overpotential among the three. The theoretical results further corroborates with the experimental observation of NFPF's instability after catalytic cycles.

References

[1] J. Xing, H. Li, M. M.-C. Cheng, S. M. Geyer and K. S. Ng, *Journal of Materials Chemistry A*, 2016, **4**, 13866–13873.

[2] Y. Li, H. Zhang, M. Jiang, Q. Zhang, P. He and X. Sun, *Advanced Functional Materials*, 2017, **27**, 1702513.

[3] C. Yang, T. He, W. Zhou, R. Deng and Q. Zhang, *ACS Sustainable Chemistry & Engineering*, 2020, **8**, 13793–13804.

[4] Y. Gorlin and T. F. Jaramillo, *Journal of the American Chemical Society*, 2010, **132**, 13612–13614.

[5] R. Gond, K. Sada, B. Senthilkumar and P. Barpanda, *ChemElectroChem*, 2018, **5**, 153–158.

[6] X. Jiang, X. Liu, Z. Zeng, L. Xiao, X. Ai, H. Yang and Y. Cao, *I Science*, 2018, **10**, 114–122.

[7] L. Sharma, R. Gond, B. Senthilkumar, A. Roy and P. Barpanda, *American Chemical Society Catalysis*, 2019, **10**, 43–50.

[8] P. Giannozzi *et al.*, *J. Phys. Cond. Matter*, 2009, **21**, 395502.

[9] T. A. Barnes, T. Kurth, P. Carrier, N. Wichmann, D. Prendergast, P. R. Kent and J. Deslippe, *Computer Physics Communications*, 2017, **214**, 52–58.

[10] M. Ernzerhof and G. E. Scuseria, *The Journal of Chemical Physics*, 1999, **110**, 5029–5036.

[11] C. Adamo and V. Barone, *The Journal of Chemical Physics*, 1999, **110**, 6158–6170.

[12] A. M. Rappe, K. M. Rabe, E. Kaxiras and J. Joannopoulos, *Physical Review B*, 1990, **41**, 1227.

[13] K. F. Garrity, J. W. Bennett, K. M. Rabe and D. Vanderbilt, *Computational Materials Science*, 2014, **81**, 446–452.

[14] L. Sharma, P. K. Nayak, E. de la Llave, H. Chen, S. Adams, D. Aurbach and P. Barpanda, *ACS Applied Materials & Interfaces*, 2017, **9**, 34961–34969.

[15] L. Sharma, A. Bhatia, L. Assaud, S. Franger and P. Barpanda, *Ionics*, 2018, **24**, 2187–2192.

[16] S. H. Swafford and E. M. Holt, *Solid State Sciences*, 2002, **4**, 807–812.

[17] B. Hammer, O. H. Nielsen and J. Nørskov, *Catalysis Letters*, 1997, **46**, 31–35.

5

Computational Modelling of MOF Derived Co_3O_4@Co Nanocomposite for Electrochemical Hydrogen Evolution Reaction

5.1 Introduction

Until now we have discussed about the inevitable role of metal air battery, fuel cell in the advancement of green renewable technologies and also about the importance of catalysts showing either oxygen reduction reaction (ORR) or oxygen evolution reaction (OER) or both (bifunctional catalysts). Another half cell reaction of OER (in water splitting process) is hydrogen evolution reaction (HER) and of ORR (in water formation reaction) is hydrogen oxidation reaction (HOR), which are equally important. Interestingly, till date Pt-based catalysts have been proved to be the best for both HER and HOR[1]. In fact, these are being used in commer-

cial scale too. However, the usage comes with severe issues[2–5], namely, high cost and scarcity of Pt metal. Also Pt-based catalysts get easily aggregated and dissolved under poor condition and hence show low electrocatalytic activity. To avoid all these shortcomings and also synthesize cost effective catalysts, the focus has shifted to earth abundant materials. There are many reviews[6–8] discussing about the good catalytic activities of such systems in acidic and in alkaline medium. Similar to the bifunctional catalysts, in recent years, systems have been developed to exhibit OER, ORR and HER, popularly known as trifunctional catalysts.[9–13] Indeed this is a breakthrough in the field of green energy storage and conversion processes. Here, in many cases metal-free and lighter transition-metal impregnated nitrogen doped carbon systems (MNCs), soft materials like gels or organic porous polymers are used as alternatives to the state-of-art precious commercialized catalysts. The distributions of N and C are crucial for the efficiencies and stability of the catalysts in many cases. Various MNCs[14–19] derived from supramolecular assemblies, polymers or metal-organic frameworks (MOFs) show trifunctional activities. Some of the MOF derivative systems have shown bifunctional activities.[20–23] Hence, a proper strategy to design a MOF derived trifunctional catalyst is yet to be explored.

Recently, Maji *et al.,*[24] has reported a detailed approach to prepare Co_3O_4@Co/NCNT (NCNT = nitrogen-doped carbon nanotube), where metallic Co cores decorated with Co_3O_4 semiconductive shells are embedded in N-doped carbon nanotubes, rich in Co–N_4 moieties from dicyanamide-containing Co-based porous MOF $[Co(bpe)_2(N(CN)_2)]\cdot(N(CN)_2)\cdot(5H_2O)_n$ [CoMOF^{-1}, bpe = 1,2-bis(4-pyridyl)ethane), $N(CN)_2^-$ = dicyanamide]. The presence of several functionals in this system has helped in showing all three catalytic activities; for example Co_3O_4@Co/NCNT show both ORR and OER activity, also N-doped carbon nanotube (CNT) with Co-N_4 sites have exhibited activity for HER. An earlier report[25] has suggested that g-C_3N_4 is found to be a good HER catalyst. The

presence of cobalt nanoparticles or Co_3O_4 has improved the HER.[26,27] Hence, it will be interesting to study the role of these atoms (N or Co) on HER and this theoretical study has been conducted in compliance with the experimental observation by T. Maji and his group.

5.1.1 Computational Details:

Spin polarized density functional theory based calculations were performed using the GGA (Generalized gradient approximation) based Perdew Burke Ernzerhoff[28] exchange correlation functional as implemented in the Quantum Espresso 5.2.0 package.[29,30] Along with Rappe-Rabe-Kaxirus-Joannopoulas ultrasoft pseudopotential[31] for valence electrons, the wave function kinetic energy cut-off of 30 Ry was considered. A rectangular supercell of carbon nanotube (CNT) containing 127 atoms of $(20 \times 20 \times 17.2)$ Å was taken, which is periodic in z-direction only. $1 \times 1 \times 4$ uniform k-point mesh was considered to sample the whole system and $1 \times 1 \times 12$ k-point for the projected density of states (pDOS) calculations. The atoms were allowed to be relaxed fully under the convergence threshold of 10^{-4} eV on total energy and 10^{-3} eV on forces on each atom. The electronic adsorption energies at 0K temperature were obtained through the DFT calculations while the zero point energy correction (ZPE) and entropic effect at finite temperature (300K) were considered to calculate the corresponding change in free energy (ΔG) from the data of previously reported[32] paper on the same class of systems. The whole reaction is conducted in the acidic medium, hence directly we are considering the following step:

$$Cat + H^+ + e^- = Cat - H^* \tag{5.1}$$

Here $*$ represents an adsorbed species; in this case the catalytic activity of a system can directly be correlated with the change in free energy ΔG(H*). Theo-

retically, on an ideal HER catalyst, $\Delta G(H^*)$ should be close to zero to facilitate both H* adsorption and desorption.

5.1.2 Results and Discussion:

As mentioned above, *Maji et al.*, have synthesized the structure from MOF and the HER activity is found to be proportional to N-weight%. In fact, their final system has shown highest catalytic activity with the change in free energy being nearly 0 eV. But, the correct configuration of the active system is still unknown. Hence we have done the theoretical modelling by gathering knowledge from the active peak in the X-ray photoelectron spectroscopy (XPS). This plot confirms the presence of metallic Co, Co-N_4 environment and graphitic N. Since the whole system is based upon CNT, the initial simplistic attempt we made, considered the Co-N_4 doped CNT system (from XPS). To determine the active site for H adsorption, we calculated the $\Delta G(H^*)$ on Co and an adjacent N site (here all four N-centers are equivalent). On the pristine model system, CoN_4–CNT, the preferred site of adsorption is Co, although ($\Delta G(H^*)$ is 0.53 eV on Co vs 1.09 eV on N) the binding strength is too weak to exhibit HER activity. Hence, the aim is to modulate the H adsorption by enclosing the Co atom(s) with doping of N in the CNT to push $\Delta G(H^*)$ toward zero. Since this did not result in the reduction of $\Delta G(H^*)$, we studied a single Co-atom encapsulated in the CNT considering the peak corresponding to the metallic Co in XPS, but the resulting system showed comparatively poorer activity than the previous system. Next, we considered a four-atom Co cluster (tetrahedral shaped) encapsulated in the CNT (Co_4@CoN_4-CNT), which showed an activity similar to the first system without metallic Co. Structures of the latter two systems are shown in Fig. 5.1.

Since the former strategy of encapsulating either a Co atom or a 4 atom Co cluster within the CNT did not seem to improve the H adsorption process, we

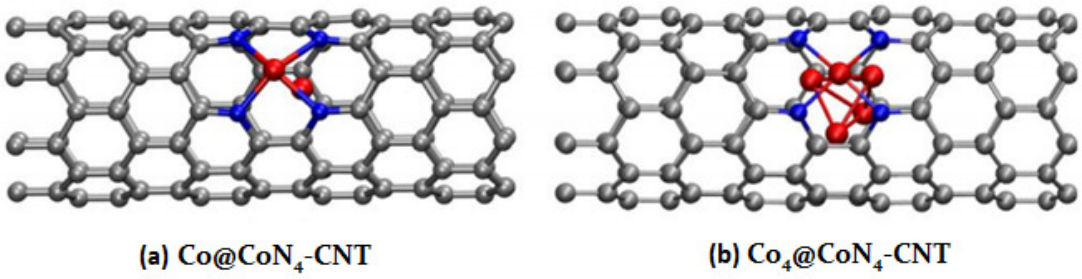

Figure 5.1: (a) Co@CoN_4-CNT, (b) Co_4@CoN_4-CNT

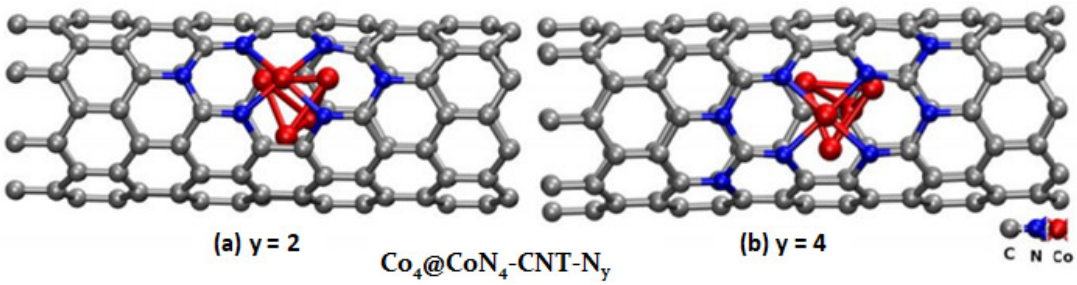

Figure 5.2: (a) Co_4@CoN_6-CNT, (b) Co_4@CoN_8-CNT

proceeded systematically with varying concentration of doped N. We increased N-weight% from 3.08 % to 7.66% with a variance of 1.52% around the CoN_4 moiety (Co_4@CoN_4–CNT-N_y; y = 2, 4, 6). These models were built on the basis of previously reported literature, where the increased weight% of N up to a certain level was shown to enhance the activity.[24] We believed that the present strategy would be able to delineate the synergistic effects among the different components of the catalysts.

We found that the introduction of N atoms in Co_4@CoN_4–CNT has a more pronounced effect. From 5.2, it is clear that all N-centers are not equivalent and hence we have considered the adsorption of H-center on each possible active sites. For Co_4@CoN_4–CNT-N_2, the Co atom remains the active site with slightly lower $\Delta G(H^*)$ compared to that of Co_4@CoN_4–CNT. All the values are given in table 5.1.

Interestingly, with the introduction of two more N atoms in the CNT lattice,

	ΔG(on Co center) eV	**ΔG(on N center) eV**
CoN_4–CNT	0.53	1.09
Co@CoN_4–CNT	0.90	0.90
Co_4@CoN_4–CNT	0.56	1.11
Co_4@CoN_4-N_2–CNT	0.49	1.08
Co_4@CoN_4-N_4–CNT	0.55	0.37
Co_4@CoN_4-N_6–CNT	0.58	**-0.07**

Table 5.1: ΔG values of the H-adsorption

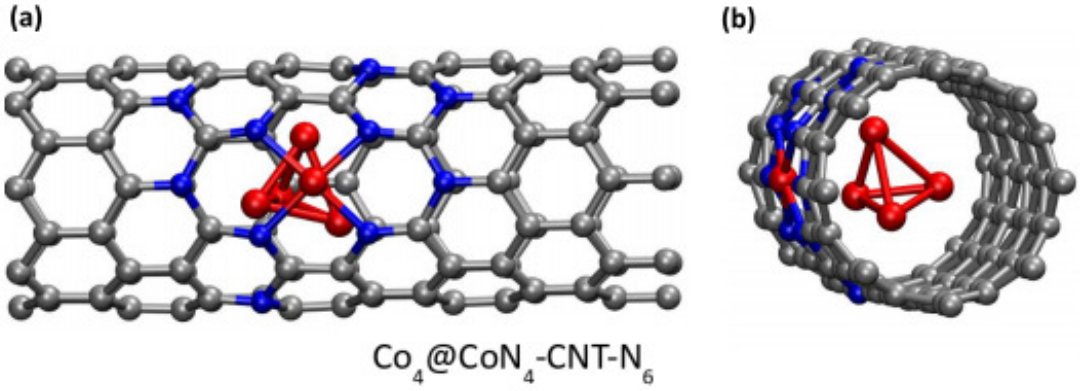

Figure 5.3: Front and side view of the catalytically active system Co_4@CoN_{10}-CNT

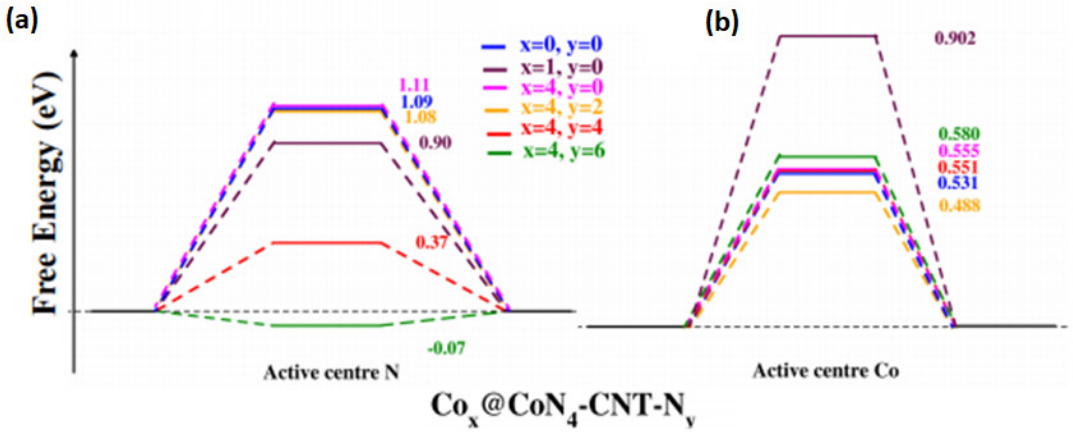

Figure 5.4: Volcano plots for (a) H-adsorption on N-center and (b) Co-center of all the considered systems.

the active site for H adsorption changes over from Co to the N center (of CoN_4); in fact, the $\Delta G(H^*)$ on the N center drops drastically to 0.37 eV in Co_4CoN_4–CNT-N_4 from 1.08 eV in Co_4CoN_4–CNT-N_2. In contrast, the $\Delta G(H^*)$ on the Co center remains $\sim$ 0.5 eV in Co_4CoN_4–CNT-N_4 (which is basically similar in most of the model systems considered).[33] Further increase in N doping concentration leads to $\Delta G(H^*)$ on N as 0.06 eV, implying that Co_4CoN_4–CNT-N_6 is the best candidate for HER of the six models considered. Analyzing all the results, we derived finally the active structure, which was experimentally considered (it is shown in Fig. 5.3). The volcano plot in Fig. 5.4 again clearly shows the shift of active site from Co-center to N-center and the best activity is found at 7.66% of N-weight%.

Taking all these results into account, we arrive at a conclusion that the active site for H adsorption in the MOF-derived catalyst, which has a similar N concentration as Co_4@CoN_4–CNT-N_6, is the N site of the Co–N_4 moiety. In order to point out the role of Co_4 tetrahedral cluster, we have calculated the projected density of states (pDOS) plot of corresponding Co atom. The t_{2g} orbitals of Co are present on the Fermi level, which points out the easy availability of electrons and transfer of charge density to the active site as shown in Fig. 5.5.

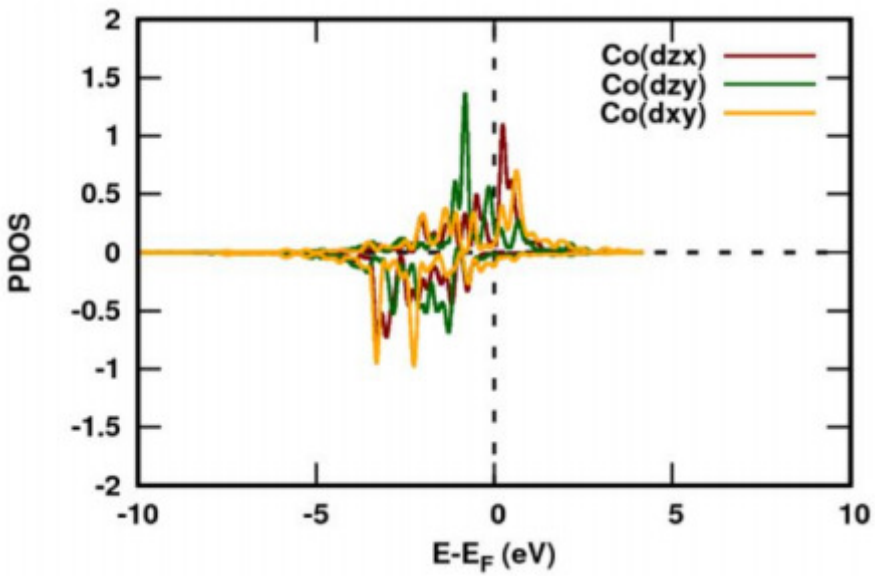

Figure 5.5: The pDOS plot of t_2 orbital of Co atom of Co_4 tetrahedral cluster.

Since this nanocomposite system shows trifunctional behavior, namely OER, ORR and HER, our experimental collaborators set up a Zn-air battery, where this nanocomposite could split water and able to generate energy through hydrogen production as verified by lighting a bulb.

5.1.3 Conclusion:

In this study, we have modelled Co_x@CoN_4–CNT-N_y[x=0,1,4; y=2,4,6] systems systematically following XPS analysis and the active system is decided, based upon $\Delta G(H^*)$ value. The active system (7.66% of N-weight%) is Co_4@CoN_4–CNT-N_6 with N of CoN_4 as the active site and an adsorption energy of -0.07 eV. This proposal and explanation compare fairly well with the experimental results.

References

[1] J. X. Wang, T. E. Springer and R. R. Adzic, *Journal of the ElectroChemical Society*, 2006, **153**, A1732.

[2] D. Li, C. Wang, D. S. Strmcnik, D. V. Tripkovic, X. Sun, Y. Kang, M. Chi, J. D. Snyder, D. van der Vliet, Y. Tsai *et al.*, *Energy & Environmental Science*, 2014, **7**, 4061–4069.

[3] G. Andreadis and P. Tsiakaras, *Chemical Engineering Science*, 2006, **61**, 7497–7508.

[4] E. Antolini, *Applied Catalysis B: Environmental*, 2010, **100**, 413–426.

[5] H. Lv and S. Mu, *Nanoscale*, 2014, **6**, 5063–5074.

[6] J. Wei, M. Zhou, A. Long, Y. Xue, H. Liao, C. Wei and Z. J. Xu, *Nano-Micro Letters*, 2018, **10**, 75.

[7] W. Zhou, J. Jia, J. Lu, L. Yang, D. Hou, G. Li and S. Chen, *Nano Energy*, 2016, **28**, 29–43.

[8] C. A. Campos-Roldán and N. Alonso-Vante, *Electrochemical Energy Reviews*, 2019, **2**, 312–331.

[9] H. Li, Q. Li, P. Wen, T. B. Williams, S. Adhikari, C. Dun, C. Lu, D. Itanze, L. Jiang, D. L. Carroll *et al.*, *Advanced Materials*, 2018, **30**, 1705796.

[10] S. Surendran, S. Shanmugapriya, A. Sivanantham, S. Shanmugam and R. Kalai Selvan, *Advanced Energy Materials*, 2018, **8**, 1800555.

[11] B. Devi, R. R. Koner and A. Halder, *ACS Sustainable Chemistry & Engineering*, 2018, **7**, 2187–2199.

[12] Q. A. Islam, R. Majee and S. Bhattacharyya, *Journal of Materials Chemistry A*, 2019, **7**, 19453–19464.

[13] Z. Bai, S. Li, J. Fu, Q. Zhang, F. Chang, L. Yang, J. Lu and Z. Chen, *Nano Energy*, 2019, **58**, 680–686.

[14] S. Dang, Q.-L. Zhu and Q. Xu, *Nature Reviews Materials*, 2017, **3**, 1–14.

[15] S. Bhattacharyya, C. Das and T. K. Maji, *RSC advances*, 2018, **8**, 26728–26754.

[16] X. Xu, F. Nosheen and X. Wang, *Chemistry of Materials*, 2016, **28**, 6313–6320.

[17] X. Wang, L. Yu, B. Y. Guan, S. Song and X. W. Lou, *Advanced Materials*, 2018, **30**, 1801211.

[18] Q. Ren, H. Wang, X.-F. Lu, Y.-X. Tong and G.-R. Li, *Advanced Science*, 2018, **5**, 1700515.

[19] H. Zhang, X. Liu, Y. Wu, C. Guan, A. K. Cheetham and J. Wang, *Chemical Communications*, 2018, **54**, 5268–5288.

[20] B. You, N. Jiang, M. Sheng, S. Gul, J. Yano and Y. Sun, *Chemistry of Materials*, 2015, **27**, 7636–7642.

[21] Y. Guo, J. Tang, H. Qian, Z. Wang and Y. Yamauchi, *Chemistry of Materials*, 2017, **29**, 5566–5573.

[22] W. Zhang, X. Yao, S. Zhou, X. Li, L. Li, Z. Yu and L. Gu, *Small*, 2018, **14**, 1800423.

[23] N. Cheng, L. Ren, X. Xu, Y. Du and S. X. Dou, *Advanced Energy Materials*, 2018, **8**, 1801257.

[24] N. Sikdar, B. Konkena, J. Masa, W. Schuhmann and T. K. Maji, *Chemistry–A European Journal*, 2017, **23**, 18049–18056.

[25] Y. Zheng, Y. Jiao, Y. Zhu, L. H. Li, Y. Han, Y. Chen, A. Du, M. Jaroniec and S. Z. Qiao, *Nature Communications*, 2014, **5**, 1–8.

[26] W. Zhou, J. Zhou, Y. Zhou, J. Lu, K. Zhou, L. Yang, Z. Tang, L. Li and S. Chen, *Chemistry of Materials*, 2015, **27**, 2026–2032.

[27] X. Yan, L. Tian, M. He and X. Chen, *Nano Letters*, 2015, **15**, 6015–6021.

[28] M. Ernzerhof and G. E. Scuseria, *The Journal of Chemical Physics*, 1999, **110**, 5029–5036.

[29] P. Giannozzi, S. Baroni, N. Bonini, M. Calandra, R. Car, C. Cavazzoni, D. Ceresoli, G. L. Chiarotti, M. Cococcioni, I. Dabo *et al.*, *Journal of Physics: Condensed Matter*, 2009, **21**, 395502.

[30] T. A. Barnes, T. Kurth, P. Carrier, N. Wichmann, D. Prendergast, P. R. Kent and J. Deslippe, *Computer Physics Communications*, 2017, **214**, 52–58.

[31] A. M. Rappe, K. M. Rabe, E. Kaxiras and J. Joannopoulos, *Physical Review B*, 1990, **41**, 1227.

[32] W. Pei, S. Zhou, Y. Bai and J. Zhao, *Carbon*, 2018, **133**, 260–266.

[33] Y. Yang, Z. Lun, G. Xia, F. Zheng, M. He and Q. Chen, *Energy & Environmental Science*, 2015, **8**, 3563–3571.

6

Explaining the deleterious impact of secondary *versus* tertiary Nitrogen center on PNP-pincer Co(I)-complexes for hydrogenation of CO_2

6.1 Introduction

The desire to reducing fossil fuels consumption and CO_2 emission encourage the usage of green fuels on a large scale. In this regard, conversion of CO_2 to HCOOH is considered as a crucial step since HCOOH is a major source of green fuel, H_2. Considering CO_2 as a C1 block source also helps in controlling the amount of this green house gas in the environment. However, this reaction is subjected to a large number of detailed studies worldwide for a last few decades due to the inert nature of CO_2.

The quest for getting a suitable homogeneous catalyst for this conversion had

started way back in 1974 by Inoue's group and over the years, 4d and 5d transition metals have outperformed 3d transition metals, resulting in more studies on 3rd and 4th row transition metals, mainly Ru[1–5], Rh[6–8] and Ir.[9–12] Till date, Ir(III) complex has shown one of the best TON of 3500000 h^{-1} in the basic medium. However, most of these results have been realised at very high pressure. Though these heavy transition metals have shown extremely good performance, the low availability, high price and toxic nature restrict their industrial use and seek the involvement of base metals to synthesize environmental benign and cost effective catalysts. In 2003, the base metals attracted the attention when Jessop's group found a notable good activity of Fe and Ni-complex while screening the catalysts with a high pressure combinatorial approach.[13] Though the usage of base metals had started very lately, they are always being used in the systems synthesized by nature. Over the time, different group has tried to mimic the structure to gain similar TON. One such example is Mn-bipyridine complex synthesized by Khusnutdinova's group[14], showing a TON of 6250 in the presence of external base. Along with base, a proper design of ligand is capable of tuning the reactivity, as suggested by Das et. al.[15] studies on Mn(I)-acylmethylpyridinol and analogous structures. Mn(I)-pincer complex is found to show a TON of 30000 in the presence of external base and Lewis acid.[16] Pincer complex comprises of a special class of chelating agent (aliphatic or aromatic), which binds the metal atom with the three adjacent coplanar sites.[17–20] These complexes are popular for exhibiting good catalytic activity under moderate temperature and pressure.[21,22] The efficiency of aromatic pincer complexes is attributed to the aromatization-dearomatization of the catalyst during the course of the reaction, which reduces the activation energies. This phenomenon is quite common in nature including proteins, enzymes etc and is known as metal-ligand cooperativity (MLC), which was first pointed by R. Noyori.[23] In aliphatic pincer(PXP) complexes (X=N,C) MLC is observed through the deprotonation-protonation of the X-center.[24–27] It has been found

to be favorable in each cases until Bernskoetter's group found an opposite results for a few base metal-based pincer complexes.[28–30] PNP-pincer complexes with tertiary amine(with a methyl group) have outperformed the analogous structure with secondary amine quite significantly but the exact reason is still undetermined.

In this chapter, we have considered Co(I)PNP pincer complexes[30] and have studied their catalytic activity and found that its tertiary analogue shows turn over number (TON) 64 times higher than the secondary one. This result agrees well with the other observations wherein just the nature of the N-center in PNP-pincer complex decides the whole reactivity. This creates a doubt on the role of MLC since according to the our study, the secondary amine is able to exhibit this activity during hydrogenation-dehydrogenation reaction. We are interested in finding the actual reason(s) behind these results by considering all possible reaction pathways of Co(I)PNP pincer in the presence and absence of external base.

6.2 Computational Details

All the density functional theory (DFT) calculations were carried out in the Gaussian 16 suite of programs[31] by considering the M06[32] exchange correlation functional along with the all-electron 6-31+G(d,p) basis set for lighter elements (C, H, N, O and P) and effective core potential, LanL2DZ for Co. This basis set combination is hereafter denoted by BS-I. The gas phase energy was calculated using higher basis set 6-311++G(d,p) for lighter elements and SDD with mdf10 effective core potential for Co. This combination is designated as BS-II. Solvent (acetonitrile) effects were taken into account by SMD model of Truhlar and Cramer.[33] Thermal corrections were computed at T = 318.15 K and 1 atm pressure considering the harmonic potential approximation[34] on optimized structures. The nature of all the optimized structures were verified on the basis of harmonic vibrational analysis: minima with zero imaginary frequency and transition state with

one imaginary frequency. Intrinsic reaction coordinate calculations have verified the connections of the transition states with the desired minima on the either side of the saddle point. Zero-point energy corrections are considered in all the Gibbs free energies.

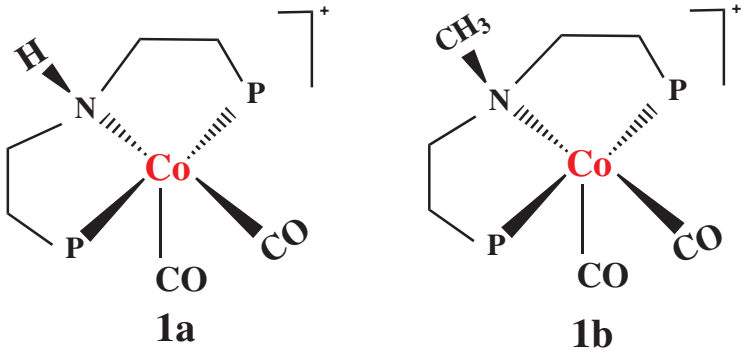

Figure 6.1: 1a: Co(I)PNP [secondary N] and 1b: Co(I)PNP [tertiary N]

6.3 Results

The homogeneous reduction of CO_2 to HCOOH proceeds in the following manner. A sigma complex (H_2-catalyst adduct) is first formed, followed by the splitting of H-H bond in the presence of external base resulting in hydride atom attached to the metal (M)-center. With the approach of CO_2 towards the M-center, the hydride gets transferred to the C-center of CO_2 resulting in formate. So, there are two transition states (TS) i.e. splitting of H-H bond of sigma complex and transfer of hydride anion to the C-center, hence it is a two step mechanism. However, for several monohydride and dihydride complexes, the reaction begins with the transfer of hydride to the M-center and then formation of sigma complex followed by heterolytic cleavage of H-H bond resulting in the starting complex. Now, the rate determining step (RDS) can either be of these two TS's. There are several studies which show splitting of sigma complex is the RDS[35–37] while some found

the hydride transfer to be the RDS.[11,38] The RDS has significant effect on the catalytic activity of the complex, hence detecting of it will help to improve the reactivity. Fig. 1 shows the structures of the catalysts under investigations, **1a** and **1b**. Their structural parameters are in well agreement with the experimental data. In this section, we shall elucidate the mechanism of hydrogenation of CO_2 to formate in detail for **1a** and **1b**, separately.

6.3.1 Catalyst 1a:

1a features Co(I) in a distorted square pyramidal geometry in which three out of four equatorial sites are taken by the PNP-pincer ligand while a CO ligand occupies the remaining one. One axial site is occupied by another CO ligand and that leaves the sixth coordination site free for binding with reactant/solvent molecules. According to our computations, binding of a solvent molecule is predicted to be endergonic by 22.7 kcal/mol, suggesting that well availability of the active site to participate in the hydrogenation reaction.

Fig. 2 depicts the tentative mechanistic scenarios for the hydrogenation of CO_2 by **1a**. First of all, H_2 molecule coordinates to the Co center to form a weak σ-complex, **2a**.The slightly stretched H-H bond length in **2a** corresponds to a Co-d to $\sigma*(H-H)$ donation as confirmed by the NBO analysis. Perhaps more striking is the substantial increase in the Co-N(pincer) bond length upon H_2 coordination which leads to an opening of the catalyst pincer backbone. This structural change comes at a heavy energy price making the σ-complex formation endergonic by 28.8 kcal/mol. In the next step, 2a is deprotonated and as shown in Fig. 4, this step can be assisted by either DBU or the pincer N atom; hereafter, these reaction routes are denoted by base-assisted pathway (BAP) and bifunctional pathway (BiFP-1), respectively. Additionally, we have also considered the possibility that, prior to the formation of σ-complex, DBU might deprotonate the catalyst 1a itself to form 1a$'$.

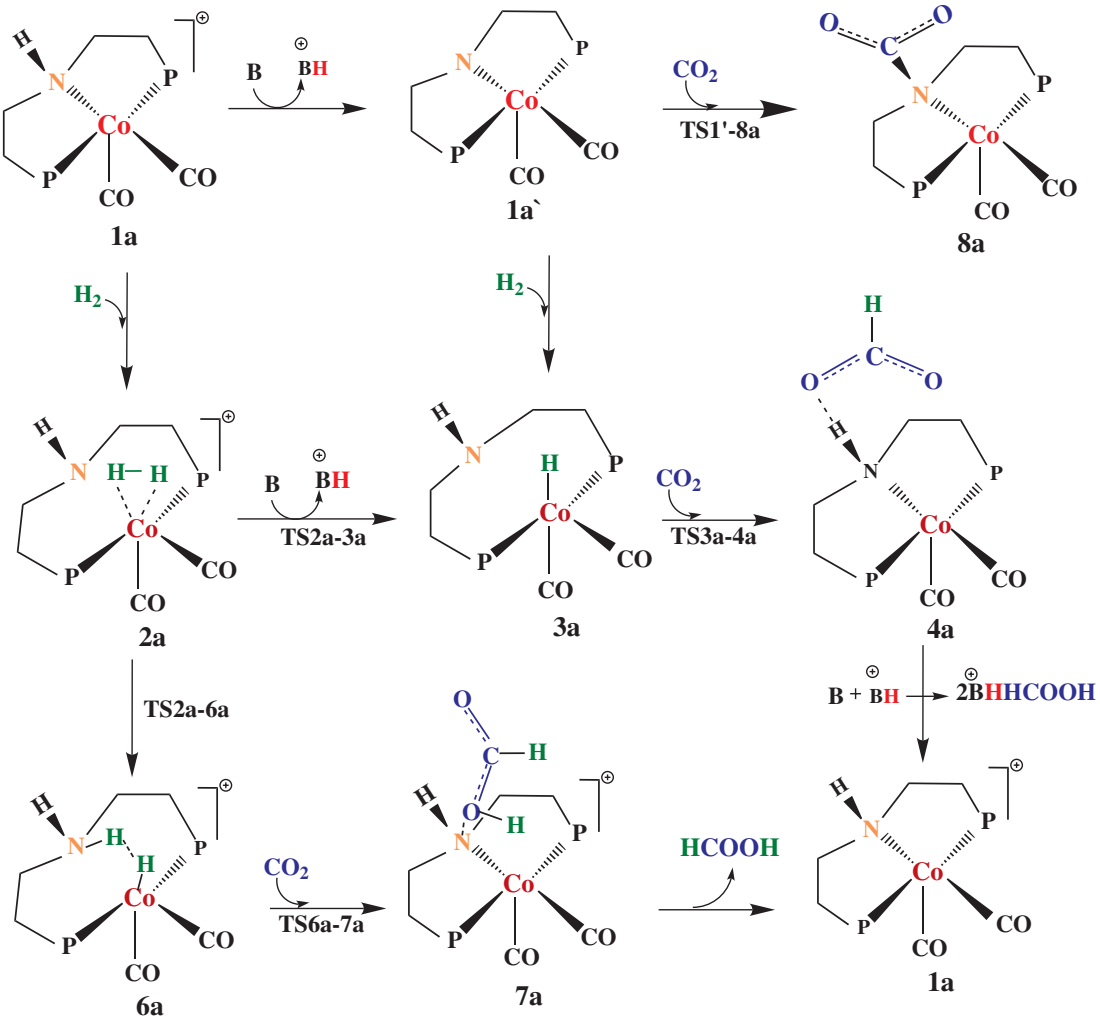

Figure 6.2: All pathways of 1a for CO_2 to HCOOH

Thereafter, H_2 cleavage by 1a′ could also lead to a third hydrogenation pathway, which we denote as BiFP-2. We will discuss each of these pathways separately.

BAP

In the DBU-assisted pathway, the H_2 is cleaved heterolytically between the Co and the N(DBU) centers leading to the formation of the Co-hydride intermediate, **3a** and $DBUH^+$. H_2 splitting occurs via **TS2a-3a** with an free energy activation barrier of **3.5** kcal/mol with respect to reference state, 1a+H_2+DBU. The pincer N atom continues to move apart from the Co center through out the H_2 cleavage and eventually, **3a** features a Co-N distance of 3.95 Å . The Co-H distance in 3a is 1.6 Å . The cycle completes as **3a** transfers the hydride to CO_2 through **TS3a-4a**, which lies at **38.1** kcal/mol. All the optimised TS structures are shown in Fig. 6.3. In **TS3a-4a**, the Co-H and the C-H distances are **1.64 Å** and **1.44 Å** , respectively. A close inspection of the TS structure reveals a series of non-covalent interactions such as (i) the oxygen atom of the CO_2 molecule weakly interacts with the isopropyl groups on the nearby Pincer P atom and (ii) more importantly, the bent CO_2 motif is involved in a H-bonding interaction with the pincer NH moiety with a N-H...O distance and angle of **2.09 Å** and **146.8**°, respectively. **TS3a-4a** relaxes to **4a** in which the formate anion remains attached to the catalyst structure through weak non-covalent interactions. Interestingly, as the hydride is released from the Co center, the Co-N(Pincer) distance decreases consistently; in **TS3a-4a** d(CO-N) reduces to **3.26 Å** before restoring the to its initial value at **1a**. These observation points to a situation wherein the hydride transfer is assisted by a push on the Co atom by a pincer N atom. Following HT, the catalyst is regenerated by dissociating **4a** to release formate and **1a**. The formate anion is further stabilized by forming H-bonding interaction with $DBUH^+$. The overall transformation from H_2+CO_2+2DBU→ 2$DBUH^+$+$HCOO^-$ is computed to be

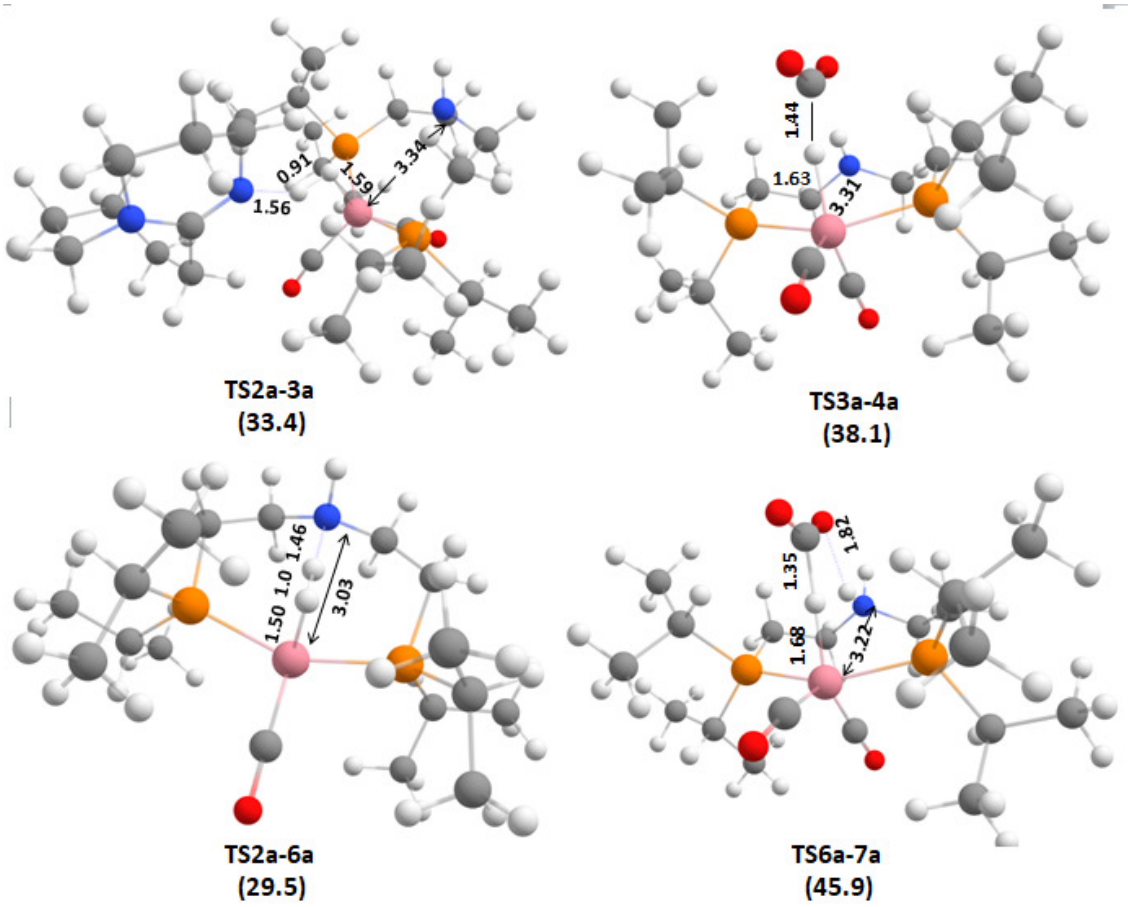

Figure 6.3: Optimised structures of transition states of 1a. All the distances are given in Å . Solvent-corrected Gibbs free energy values(in kcal/mol) are given in parentheses.

exergonic by **3.7** kcal/mol.

BiFP-1:

Next, we examine the bifunctional nature of the Co-pincer complex in which the Co and the pincer N atoms work in tandem to split H_2. In BiFP-1, H_2 activation proceeds through **TS2a-5a** leading to **5a**. The Co-H, N-H and H-H distances in TS2a-5a are 1.62 Å, 1.42 Å(DBU), and 0.93 Å respectively. **TS2a-5a** lies **3.9** kcal/mol below **TS2a-3a** in the BAP. Interestingly, HT to CO_2 in BiFP is accompanied by a simultaneous transfer of proton to the CO_2 oxygen. The corresponding TS, **TS5a-6a** lies **7.8** kcal/mol higher than that in **BAP**. **TS5a-6a** features a bent CO_2 ($\angle OCO$ = 143.6 °) molecule with a quasi-linear Co-H-C(CO_2) geometry. The Co-H and N-H distances in TS5a-6a are 1.68 Åand 1.04 Å. **TS5a-6a** relaxes to a **7a** in which the FA molecule is weakly bound to the catalyst structure. Dissociation of **7a** regenerates the catalyst and HCOOH is stabilized in the solution in the form of 2DBUH+$HCOO^-$.

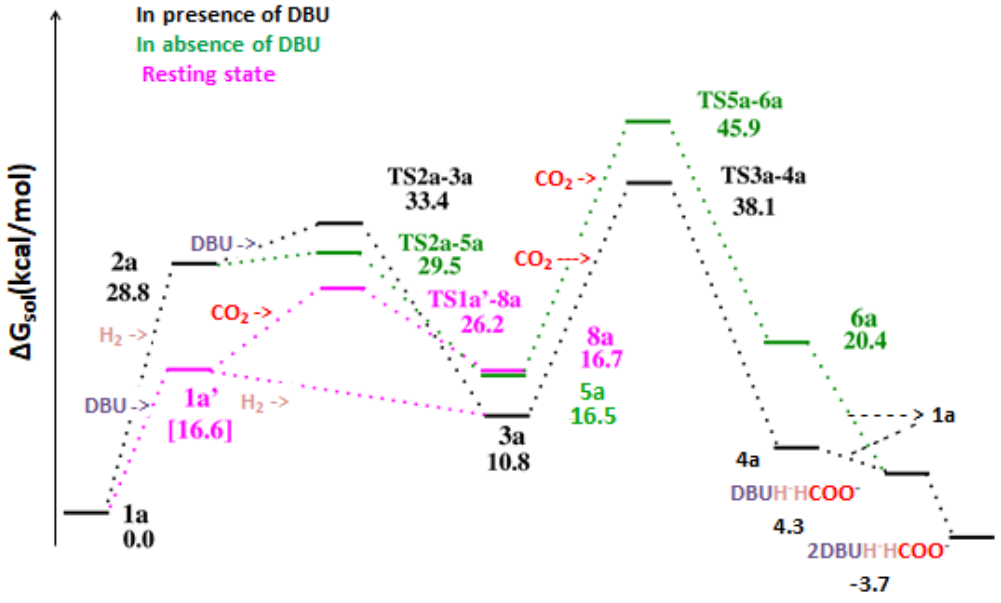

Figure 6.4: The potential energy diagram of 1a for all possible pathways. Solvent-corrected Gibbs free energy (kcal/mol) values are given in parenthesis.

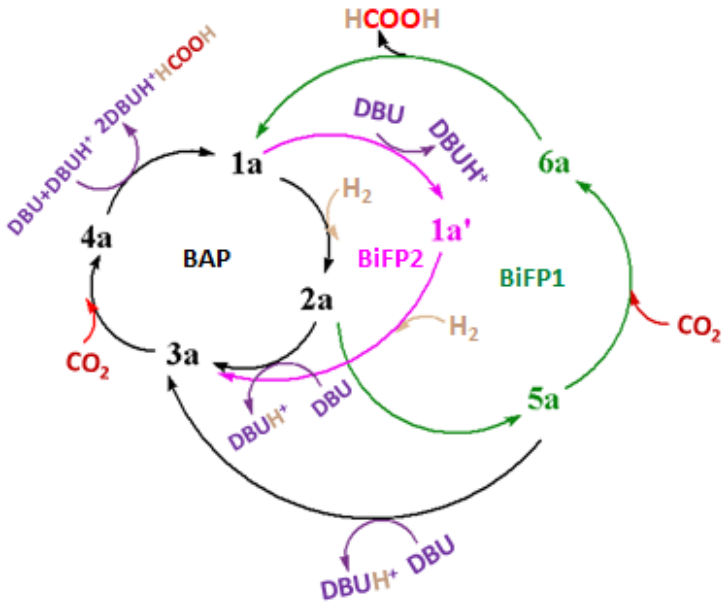

Figure 6.5: All plausible catalytic pathways

BiFP-2:

The deprotonation of N-H proton by DBU is computed to be endergonic by 16.6 kcal/mol. The structure of 1a′ features a even more reduced Co-N distance compared to 1a owing to the enhanced basicity of N-center upon deprotonation. Heterolytic cleavage of H_2 by 1a′ between the Co and N(pincer) leads to 3a which is a common intermediate with the BAP. In this case, the H-H bond gets cleaved so spontaneously that we are unable to locate the corresponding TS. HT from **3a** might follow the same route as BAP to yield FA i.e **3a** →**4a**→**1a**+**FA**. An alternative possibility is a further deprotonation of 3a to yield 7a. However, HT from 7a proceeds through TS7a-8a, which lies substantially higher (75.8 kcal/mol) than HT TS in BAP and BiFP-1, which is why we have eliminated this pathway in Fig. 4. The overall pathway is also shown in Fig. 5.

6.3.2 Resting State:

Instead of following the CO_2 reduction pathway, we find that **1a′** could capture a CO_2 molecule and this constitutes a off-cycle resting state for the catalyst. The deprotonated N-center in 1a′ having a strong nucleophilic affinity forms a stable bond with CO_2 after crossing the activation barrier of 9.6 kcal/mol. The resulting adduct, **8a** is endergonic by 0.1 kcal/mol with respect to 1a′ with N(pincer)-C(CO_2) distance of 1.60 Å . The $\angle OCO$ angle in the adduct is 134.6° with the elongated C-O bond of 0.07 Å . Interestingly, the overall structure remains closed with a slight increase of Co-N distance from 2.01 Å to 2.15 Å suggesting no extra energy (i.e. distortion energy) is required for the adduct formation. All these suggest the ease of formation of the adduct.

Lowest energy pathway for 1a

Overall, we examined three pathways leading to the hydrogenation of CO_2 to formate. Now, we analyze, compare and determine the lowest energy pathways for 1a. Fig. 5 depicts the interconnections among the three pathways. The BAP and BiFP2 pathways merge after the formation of hydride complex (3a) whereas BiFP1 and BAP bifurcates after the formation of σ-complex (2a). Although, σ-complex splitting is more favorable in case of BiFP1, the bottle neck of the reaction is hydride transfer. And from PES diagram in fig. 4, it is clear that CO_2 hydrogenation is favored for **BAP** over **BiFP1** by **7.8** kcal/mol.

6.3.3 Catalyst 1b:

In order to have a fair comparisons, we have considered all the pathways similar to 1a for 1b except BiFP2. The presence of methyl group on N-center has resulted in a steric interaction leading to elongation of N-Co bond (2.18 Å) compared to that in 1a (2.07 Å) and also the structure more looks like distorted trigonal bipyramid

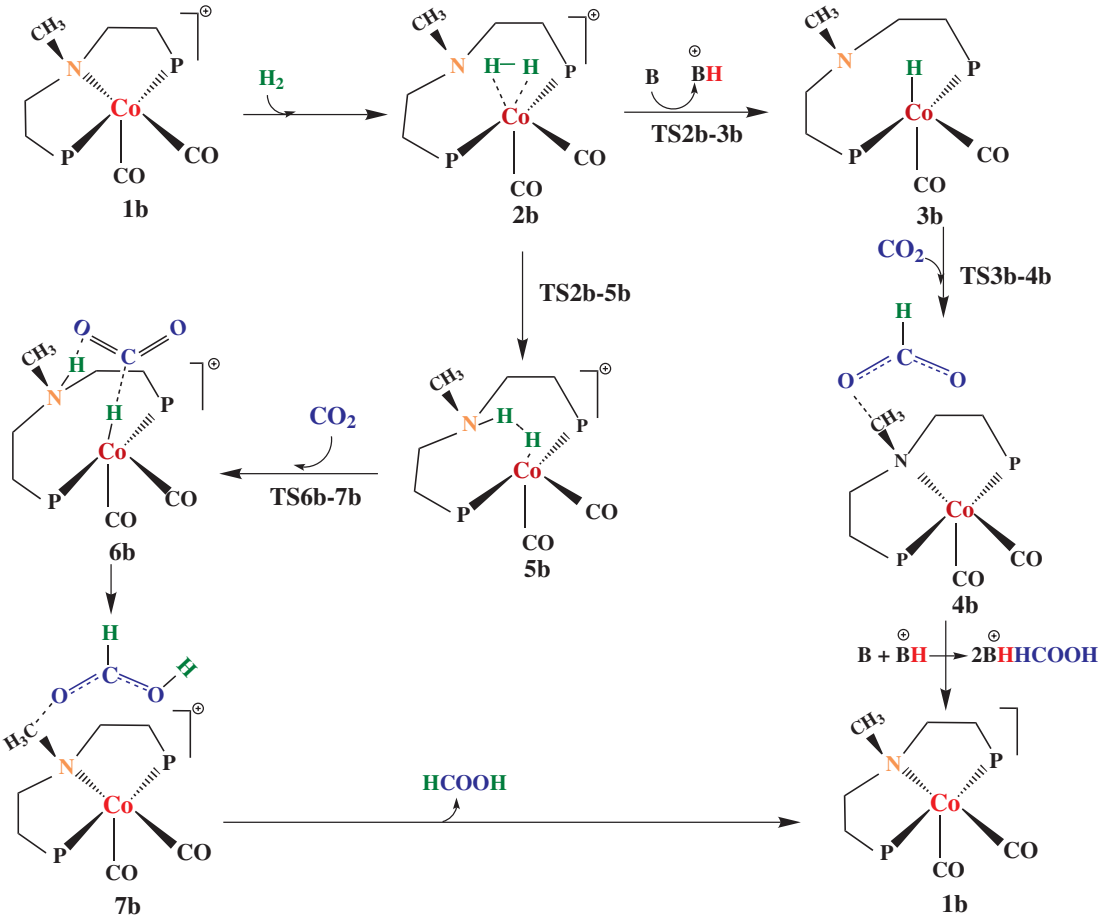

Figure 6.6: All pathways of 1b for CO_2 to HCOOH

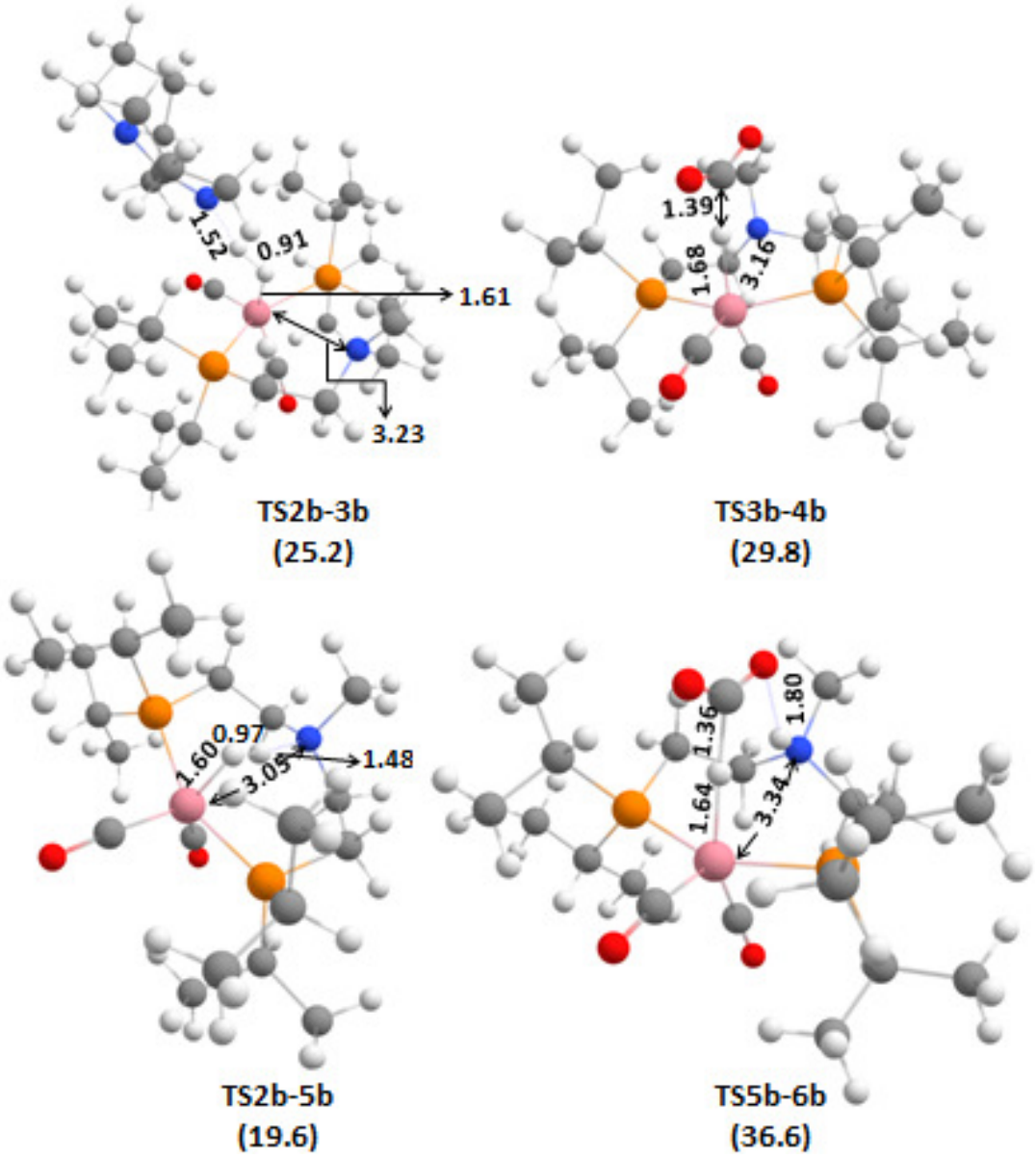

Figure 6.7: Optimised structures of transition states of 1b. All the distances are given in Å . Solvent-corrected Gibbs free energy values(in kcal/mol) are given in parenthesis

(TBP). The binding of a solvent molecule is endergonic (12.9 kcal/mol) in nature leaving the active site available. The detailed mechanistic pathways are shown in Fig 6. The σ-complex (2b) formation, involves opening of the closed structure, is endergonic by 19.3 kcal/mol.

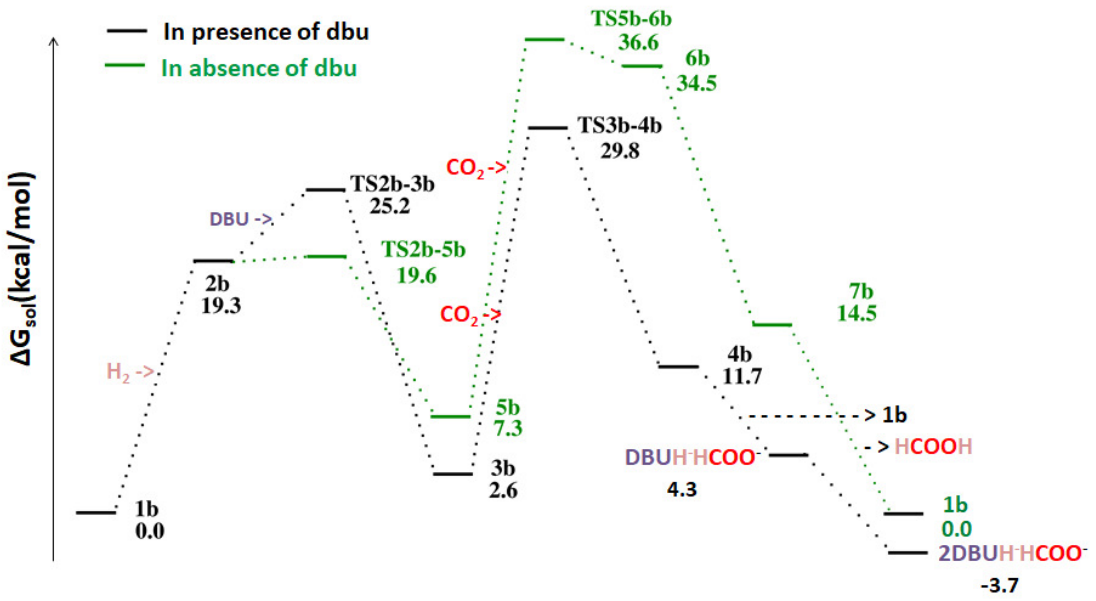

Figure 6.8: The potential energy diagram of 1b for all possible pathways. Solvent-corrected Gibbs free energy (kcal/mol) values are given in parenthesis.

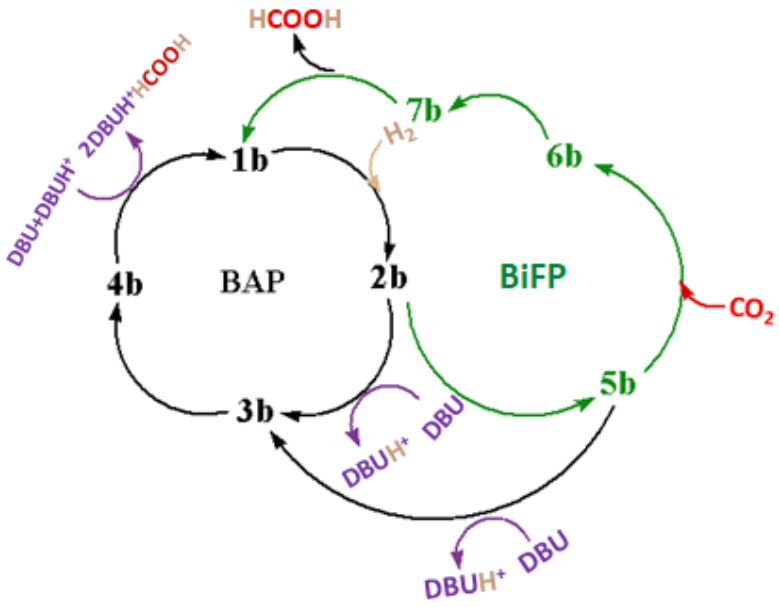

Figure 6.9: All plausible catalytic pathways

BAP

The activation energy of DBU assisted splitting of sigma complex is **5.9** kcal/mol with respect to the reference state, 1b+H_2+DBU. The Co-N bond gets stretched

till formation of hydride complex (3b) with the highest distance of 3.76 Å . Note that, the Co-H bond length here is 1.50 Å . The next step, hydride transfer to the C-center of CO_2 at TS2b-3b lies at 29.8 kcal/mol (shown in Fig. 7). The Co-H-C centers are almost aligned in a straight line with (¡Co-H-C=160.1°) and Co-H and C-H bond lengths of 1.68 Å and 1.39 Å respectively in the TS. The structure gets back to its original closed form soon after formation of $HCOO^-$ (4b). A weak interaction has been suggested among O($HCOO^-$)-H(methyl group at N-center) at a distance of 2.09 Å . The intermediate figures are given in Fig. 7.

BiFP

Next we focus on the pathway (shown in Fig. 8 and Fig. 9) in absence of DBU which commences with σ-complex (2b) splitting by the simultaneous involvement of Co- and N-centers. Contrary to the previous observation in the presence of DBU, the Co-N distance has reduced slightly from 3.13 Å (2b) to 3.05 Å in TS2b-5b. The NBO analysis also suggests unequal charge distribution on H-H part with comparatively less electron density on H towards N-side. Surprisingly, the activation energy is 19.6 kcal/mol with respect to the reference state **1b** + $\mathbf{H_2}$. The **TS2b-5b** looks familiar with **1b** as both has TBP structure, which is further confirmed from the alignment of the orbitals. The reaction proceeds with the transfer of hydride and proton in two consecutive steps. At **TS5b-6b** the $\angle CHCo$ is 177.8 ° with Co-H and C-H distance of 1.64 Å and 1.36 Å respectively. The NBO study reveals that the O-center near to the N-H is more negatively charged (-0.70) compared to the other(-0.57). The **TS5b-6b** lies at 36.6 kcal/mol.

6.4 Discussion

The theoretical analyses agree with the experimental observation that 1b outperforms 1a. According to Bernskoetter et. al. MLC may be the reason behind the

Table 6.1: Energy variations of 1a-systems in kcal/mol and distance of N-Co in Å .

Systems	**Free Energies**	**Distortion Energies**	**N-Co**
1a	0.0	0.0	2.07
2a	28.8	43.2	3.11
TS2a-3a	33.4	31.8	3.34
3a	12.1	61.0	3.95
TS3a-4a	38.1	45.3	3.31
4a	7.0	8.7	2.02
TS2a-6a	29.5	25.4	3.03
6a	16.5	43.2	3.11
TS6a-7a	45.9	38.4	3.22
7a	20.4	5.6	2.14

diminished activity of 1a, which is certainly not the case as sigma complex splitting is favourable in the absence of DBU in each case. It again suggests that in this case, both the systems are capable of showing MLC irrespective of the nature of N-center. Interestingly, we find that the disruption of Co-N bond is allowing N-center to participate in the reaction. However, the second transition state i.e. hydride transfer is the rate determining step and both in presence and absence of DBU, 1b favors the reduction reaction. As mentioned earlier, the opening of the closed structure during the course of the reaction contributes to the corresponding activation energies which is calculated in terms of distortion energies. Distortion energies are proportional with the Co-N distances (shown in Fig. 10) with Pearson correlation coefficient of 0.94 and 0.97 for 1a and 1b respectively. The reason behind this structural variations is unavailability of sixth coordination of Co(I) and it is a common phenomenon in biology named as "flexidentate" or "hemilability",

Table 6.2: Energy variations of 1a-systems in kcal/mol and distance of N-Co in Å .

Systems	**Free Energies**	**Distortion Energies**	**N-Co**
1b	0.0	0.0	2.18
2b	19.3	28.2	3.14
TS2b-3b	25.2	36.4	3.23
3b	2.6	56.4	3.76
TS3b-4b	29.8	32.9	3.16
4b	11.7	4.2	2.22
TS2b-5b	19.6	21.5	3.05
5b	7.3	39.4	3.14
TS5b-6b	36.6	40.5	3.34
6b	34.5	36.3	3.42
7b	14.5	0.0	2.18

which provides flexibility in the structure through the reversible conversion.[39] Unlike MLC, hemilability involves masking of the vacant site of the metal-center, through a weak bond with one of the center of multidentate hybrid ligand and on approaching of reactant towards metal-center the bond gets weakened in order to make space on the M-center. This is found to be highly promising in tuning the proper selectivity by regulating the weak metal-ligand (M-L) bond.[40,41] It is expected that bifunctionality and hemilability combinedly can enhance the activity.[42] Comparision of Table 1 and 2, suggests distortion energies are higher in case of 1a with respect to 1b. For BiFP, TS6a-7a has lower distortion energy but still higher activation energy by 9.3 kcal/mol than TS5b-6b, because both hydride and proton gets transferred in one step but for latter system, it happens in two consecutive steps. The reason behind the better performance of 1b over 1a is not only because of the difference in the distortion energies but also due to the off-cycle resting state of 1a (1a′). 1a′ is quite stable adduct with comparatively lower activation energy indicates the stable bond between N(pincer)-C(CO_2) act as a catalytic poison for 1a.

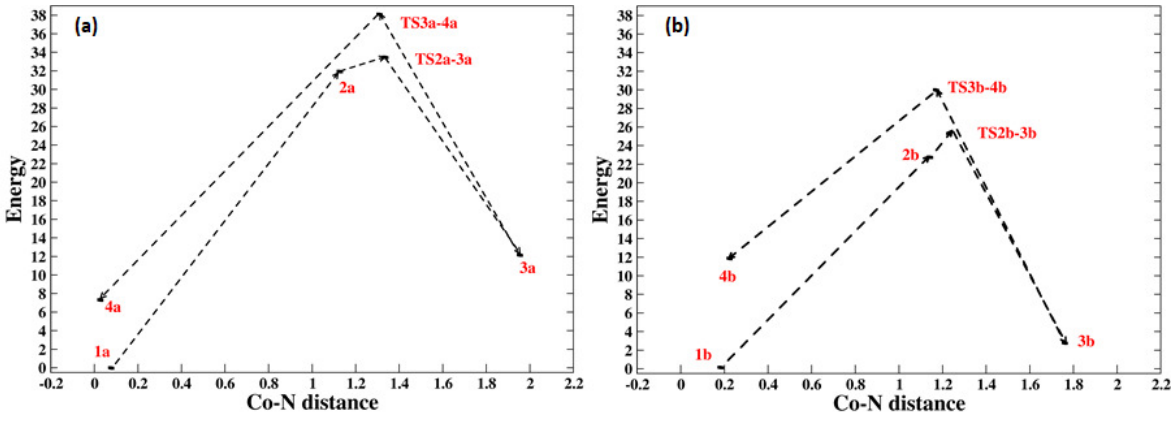

Figure 6.10: (a)Free energy vs N-Co distance of 1a; (b)(a)Free energy vs N-Co distance of 1b

6.5 Conclusion

In summary, we have studied all possible mechanism of 1a and 1b in the presence and absence of external base (DBU). For both the systems, σ-complex splitting will follow the one i.e. **BiFP** with lower activation energy of **29.5** kcal/mol and **19.6** kcal/mol for **1a** and **1b** respectively. However, the rate determining step is hydride transfer for which **BAP** has comparatively lower activation energy of **38.1** kcal/mol and **29.8** kcal/mol for **1a** and **1b** respectively. An additional proton transfer occurs in **BiFP** in concerted and sequential manner for 1a and 1b respectively. Interestingly, 1b has lower activation energy in each case, which agrees well with the experimental observation. The reason behind is the distortion energy associated with the opening of the closed structure. Our theoretical calculation has also found a off-cycle resting state of 1a, **1a′**, which is stable and poison the catalytic activity of 1a leading to such a drastic fall in TON. Thus, the main point of our study is that the MLC is not the reason behind lower activity of 1a which was anticipated by experimental study.

References

[1] C.-C. Tai, J. Pitts, J. C. Linehan, A. D. Main, P. Munshi and P. G. Jessop, *Inorganic Chemistry*, 2002, **41**, 1606–1614.

[2] C. A. Thomas, R. J. Bonilla, Y. Huang and P. G. Jessop, *Canadian Journal of Chemistry*, 2001, **79**, 719–724.

[3] P. Munshi, A. D. Main, J. C. Linehan, C.-C. Tai and P. G. Jessop, *Journal of the American Chemical Society*, 2002, **124**, 7963–7971.

[4] G. A. Filonenko, R. van Putten, E. N. Schulpen, E. J. Hensen and E. A. Pidko, *ChemCatChem*, 2014, **6**, 1526–1530.

[5] G. A. Filonenko, E. J. Hensen and E. A. Pidko, *Catalysis Science & Technology*, 2014, **4**, 3474–3485.

[6] W. Leitner, *Angewandte Chemie International Edition in English*, 1995, **34**, 2207–2221.

[7] F. Gassner and W. Leitner, *Journal of the Chemical Society, Chemical Communications*, 1993, 1465–1466.

[8] N. Ezhova, N. Kolesnichenko, A. Bulygin, E. Slivinskii and S. Han, *Russian Chemical Bulletin*, 2002, **51**, 2165–2169.

[9] C. Caix, S. Chardon-Noblat and A. Deronzier, *Journal of Electroanalytical Chemistry*, 1997, **434**, 163–170.

[10] S. E. Witt, T. A. White, Z. Li, K. R. Dunbar and C. Turro, *Chemical Communications*, 2016, **52**, 12175–12178.

[11] S. Ogo, R. Kabe, H. Hayashi, R. Harada and S. Fukuzumi, *Dalton Transactions*, 2006, 4657–4663.

[12] Y. Himeda, N. Onozawa-Komatsuzaki, H. Sugihara and K. Kasuga, *Organometallics*, 2007, **26**, 702–712.

[13] C.-C. Tai, T. Chang, B. Roller and P. G. Jessop, *Inorganic Chemistry*, 2003, **42**, 7340–7341.

[14] A. Dubey, L. Nencini, R. R. Fayzullin, C. Nervi and J. R. Khusnutdinova, *American Chemical Society Catalysis*, 2017, **7**, 3864–3868.

[15] S. Das and S. K. Pati, *Catalysis Science & Technology*, 2018, **8**, 3034–3043.

[16] F. Bertini, M. Glatz, N. Gorgas, B. Stöger, M. Peruzzini, L. F. Veiros, K. Kirchner and L. Gonsalvi, *Chemical Science*, 2017, **8**, 5024–5029.

[17] R. Tanaka, M. Yamashita, L. W. Chung, K. Morokuma and K. Nozaki, *Organometallics*, 2011, **30**, 6742–6750.

[18] G. A. Filonenko, M. P. Conley, C. Copéret, M. Lutz, E. J. Hensen and E. A. Pidko, *ACS Catalysis*, 2013, **3**, 2522–2526.

[19] C. Gunanathan and D. Milstein, *Accounts of Chemical Research*, 2011, **44**, 588–602.

[20] D. Milstein, *Philosophical Transactions of the Royal Society A: Mathematical, Physical and Engineering Sciences*, 2015, **373**, 20140189.

[21] R. Langer, Y. Diskin-Posner, G. Leitus, L. J. Shimon, Y. Ben-David and D. Milstein, *Angewandte Chemie International Edition*, 2011, **50**, 9948–9952.

[22] O. Rivada-Wheelaghan, A. Dauth, G. Leitus, Y. Diskin-Posner and D. Milstein, *Inorganic Chemistry*, 2015, **54**, 4526–4538.

[23] K.-J. Haack, S. Hashiguchi, A. Fujii, T. Ikariya and R. Noyori, *Angewandte Chemie International Edition in English*, 1997, **36**, 285–288.

[24] S. Chakraborty, P. O. Lagaditis, M. Forster, E. A. Bielinski, N. Hazari, M. C. Holthausen, W. D. Jones and S. Schneider, *Acs Catalysis*, 2014, **4**, 3994–4003.

[25] N. M. Rezayee, D. C. Samblanet and M. S. Sanford, *ACS Catalysis*, 2016, **6**, 6377–6383.

[26] R. Xu, S. Chakraborty, S. M. Bellows, H. Yuan, T. R. Cundari and W. D. Jones, *ACS Catalysis*, 2016, **6**, 2127–2135.

[27] U. Jayarathne, Y. Zhang, N. Hazari and W. H. Bernskoetter, *Organometallics*, 2017, **36**, 409–416.

[28] Y. Zhang, A. D. MacIntosh, J. L. Wong, E. A. Bielinski, P. G. Williard, B. Q. Mercado, N. Hazari and W. H. Bernskoetter, *Chemical Science*, 2015, **6**, 4291–4299.

[29] J. B. Curley, N. E. Smith, W. H. Bernskoetter, N. Hazari and B. Q. Mercado, *Organometallics*, 2018, **37**, 3846–3853.

[30] M. R. Mills, C. L. Barnes and W. H. Bernskoetter, *Inorganic Chemistry*, 2018, **57**, 1590–1597.

[31] M. Frisch, G. Trucks, H. Schlegel, G. Scuseria, M. Robb, J. Cheeseman, G. Scalmani, V. Barone, G. Petersson, H. Nakatsuji *et al.*, *Wallingford CT*, 2016, **2**, year.

[32] Y. Zhao and D. G. Truhlar, *Theoretical Chemistry Accounts*, 2008, **120**, 215–241.

[33] A. V. Marenich, C. J. Cramer and D. G. Truhlar, *The Journal of Physical Chemistry B*, 2009, **113**, 6378–6396.

[34] G. Luchini, J. V. Alegre-Requena, I. Funes-Ardoiz and R. S. Paton, *F1000Research*, 2020, **9**, 291.

[35] M. S. Ahlquist, *Journal of Molecular Catalysis A: Chemical*, 2010, **324**, 3–8.

[36] X. Yang, *ACS Catalysis*, 2011, **1**, 849–854.

[37] C. Hou, J. Jiang, S. Zhang, G. Wang, Z. Zhang, Z. Ke and C. Zhao, *ACS Catalysis*, 2014, **4**, 2990–2997.

[38] M. S. Jeletic, M. T. Mock, A. M. Appel and J. C. Linehan, *Journal of the American Chemical Society*, 2013, **135**, 11533–11536.

[39] J. C. Jeffrey and T. B. Rauchfuss, *Inorganic Chemistry*, 1979, **18**, 2658–2666.

[40] P. Braunstein and F. Naud, *Angewandte Chemie International Edition*, 2001, **40**, 680–699.

[41] P. Braunstein, F. Naud, A. Dedieu, M.-M. Rohmer, A. DeCian and S. J. Rettig, *Organometallics*, 2001, **20**, 2966–2981.

[42] Z. G. Specht, S. A. Cortes-Llamas, H. N. Tran, C. J. van Niekerk, K. T. Rancudo, J. A. Golen, C. E. Moore, A. L. Rheingold, T. J. Dwyer and D. B. Grotjahn, *Chemistry–A European Journal*, 2011, **17**, 6606–6609.

7 Electrocatalytic Reduction of CO_2 on Ni-Corrole Based Systems

7.1 Introduction

CO_2 plays a crucial role in the eco-system, however, massive emission of it has ruined the natural balance. There are exploitation of existing resources over the years, which has created excessive emission of CO_2 causing worldwide problem. A reassuring way to fix the CO_2 level is to electrochemically convert it to various renewable fuels. Such an approach has been proved to solve the twin goals of green environment and sustainable energy. Over the years, different systems-hetero, bio, homo-have been considered for study. But being an inert molecule, a high negative potential is required to activate CO_2 which often leads into the mixture of products including carbon monoxide, formic acid, methane etc. Hence, developing of a catalyst which can reduce CO_2 into a specific chemical fuel effectively and selectively is a great challenge.

In nature, porphyrinoid systems (heterocyclic macrocycle organic compounds) have been found to be a promising one. Such an example is methanogenic archaea, an important group of microorganisms, which is able to convert CO_2 to methane within thermodynamic limit. The active center, that accomplishes this reaction, is Nickel porphyrinoid.[1] An astounding activity of $[Ni(cyclam)]^{2+}$ on mercury electrode in aqueous media for CO_2 to CO has been reported by Sauvage and co worker[2] more than three decade ago. However, mercury electrode is proved to be playing a crucial role in the efficiency of Ni-cyclam complex showed by the Froehlich and Kubiak experiments.[3] Since mercury is poisonous to nature, further research to improve the reduction efficiency is required. Later on the same group replaced the mercury electrode with glassy carbon electrode and found a drop in the reactivity. Many groups[4–9] have exploited the use of this catalyst, still mercury electrode stands to be the most efficient one till date. Ni(II)-azacyclam derivatives[10] have shown reactivity close to its cyclam analogue in aqueous medium. Another example of Ni-complex functioning in water medium for CO_2 to CO conversion is Ni-N-heterocyclic carbene pyridene complex(R)bimpy, R=Me, Et, Pr)[11], where a homologous series has been synthesized to examine the effects of chain length on catalytic activity. Ni- and Co-phthalocyanine(Pc)[12] in their bi-negative state are able to reduce CO_2. On the contrary, Mn-Pc and Fe-Pc show very poor activity in this regard; the main difference between the first two systems with the latter is the electron densities which emphasizes out the importance of d_{z^2} orbital occupancy or excess π-electrons over ligand to initiate the reaction. Similarly Ni-corrole (Ni(C)) has shown activity towards CO_2 reduction. A completely dehydrogenated corrole system is trianionic in nature, which can stabilize higher metal valent metals. Unlike the porphyrin and phthalocyanine analogues cobalt and iron Ni(C)[13] are able to reduce CO_2 to CO photochemically. Gonglach and coworkers[14] have synthesized modified molecular cobalt [triphenylphosphine 5,10.15-tris(2,3,5,6-tetraluoro-4-(MeO-PEG(7))thiophenyl)] Ni(C)

heterogenized over glassy carbon as working electrode (in methyl nitrile solvent) which successfully convert CO_2 to ethanol and methanol electrochemically. Contrast to earlier Co-Ni(C) complex this derivative prefers formic acid pathway over CO one. De and coworker[15] have synthesized a revised Mn-Ni(C) complex with polyethylene glycol at three meso position immobilized on a Carbon Paper electrode, has preferably converted CO_2 to acetic acid in mild acidic medium (pH 6). Surprisingly, not much studies have been conducted using Ni(C) systems hence it will be interesting to explore more in this direction.

Recently, Omori *et.al.*[16] has synthesized Ni(II) phosphacorrole (Ni(P)) and Ni(II) boracorrole (Ni(B)) with P- and B-atom at meso-position respectively. All the systems, they have synthesized are uni-negatively charged, which can favor the first step in CO_2 reduction reaction.

7.2 Methodology

All geometry optimizations are performed without a symmetry constraint using the b3lyp functional[17,18] within the unrestricted DFT formalism. We have considered both the low spin and high spin electronic configurations for all geometries. In all cases, the energy of the low spin configuration shows the lowest energy. van der Waals correction has been incorporated in total energy calculation using Grimme's DFT-D3 dispersion correction. For the light atoms (C, H , N, O, B ,P), 6–31G(d) basis set is employed while the SDD basis set is used on Ni atom . Solvent (water) effects are taken into account using the smd model.[19] All calculations have been carried out using Gaussian 16 package.[20] Mulliken charge analysis and NBO are also done. Computational hydrogen electrode (CHE) model is used for computing the standard equilibrium potentials of electrochemical steps. This technique also provides an elegant way of avoiding the explicit treatment of solvated protons. In this technique, zero voltage is defined based on the reversible hydrogen electrode

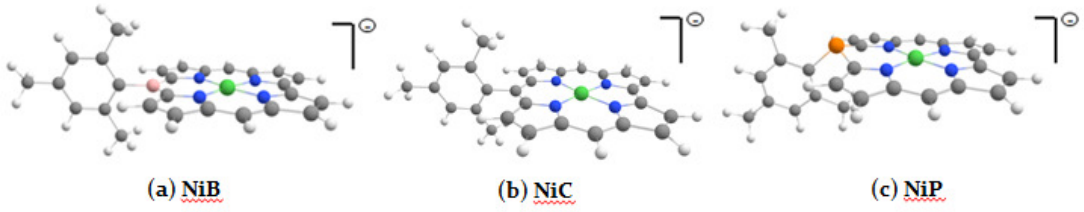

Figure 7.1: (a)Ni(II)boracorrole; (b)Ni(II)corrole; (c)Ni(II)phosphacorrole

(RHE), in which the reaction,

$$H^+ + e^- \Longleftrightarrow \frac{1}{2}H_2 \tag{7.1}$$

is set to be in equilibrium at zero voltage, at all values of pH, at all temperatures, and with H_2 at 101325 Pa (or ∼1 bar) pressure. Therefore, in the CHE, the chemical potential of a proton-electron pair, $\mu(H^+)$ + μ(e) is equal to half of the chemical potential of gaseous hydrogen (1/2) $\mu(H_2)$ at a potential of 0 V. In this way, the chemical potential of the proton-electron pair can be calculated simply by calculating the chemical potential of gas-phase H_2. CHE model can be applied to steps in which an equal number of protons and electrons are transferred i.e concerted proton-electron transfer. The equilibrium potentials for concerted proton-coupled electron transfer reactions are calculated as

$$E^\circ = -\Delta G/e \tag{7.2}$$

where E° is the standard equilibrium potential on the RHE scale , ΔG is the free energy change of the reaction, and e is the elementary charge.

7.3 Result and Discussions:

As discussed above, the activation of inert CO_2 can be initiated by a nucleophilic or electrophilic attack. Hence it would be interesting to observe how tuning the electron-density of the catalyst can directly affect the CO_2 adsorption. In order to do that, the C-atom at meso position (with respect to the Ni-atom) of Ni(C) is replaced with trivalent B and pentavalent P resulting in Ni(B) and Ni(P) respectively. All the systems considered are uni-negatively charged and the feasibility of all possible pathways for CO_2 reduction is considered for bi-negatively charged systems as well.

The macrocyclic skeletons of all the three structures are planar with mesityl group in the perpendicular fashion except in case of Ni(P) where it is tilted more in one side of the plane. The NBO analysis indicates a spread of electron density within Ni(C) part which is also observed through the bondlengths. Here, the endocyclic meso C-C bond is shorter (1.41 Å) than the exocyclic (1.50 Å) and it is true for both Ni(P) (P-C bond 1.81 Å vs 1.86 Å) and Ni(B) (B-C bond 1.52 Å vs 1.58 Å), which suggests an extensive π-conjugation inducing the aromaticity to the structures. Interestingly, the four N-centers belong to two different groups; in one group two N-atoms are part of 6-membered ring with Ni-N bond lengths of 1.88, 1.95 and 1.92 Å for Ni(C), Ni(P) and Ni(B) respectively; the other group N-atoms are part of 5-membered ring with Ni-N bond lengths of 1.86, 1.89 and 1.88 Å respectively. The bi-anionic structures of Ni(C) and Ni(B) remain the same as in uni-negative systems except for phosphacorrle with mesityl group completely aligned at one side of the plane and also with tilted sheet. Previous studies suggest that, CO_2 adsorption is favourable for electron-rich systems. According to that, uni/bi negatively charged phosphacorole should show the most favourable adsorption followed by Ni(C) and Ni(B). Here, our results partially match with this observation but with some exceptions. The uni-negative Ni(P) shows most

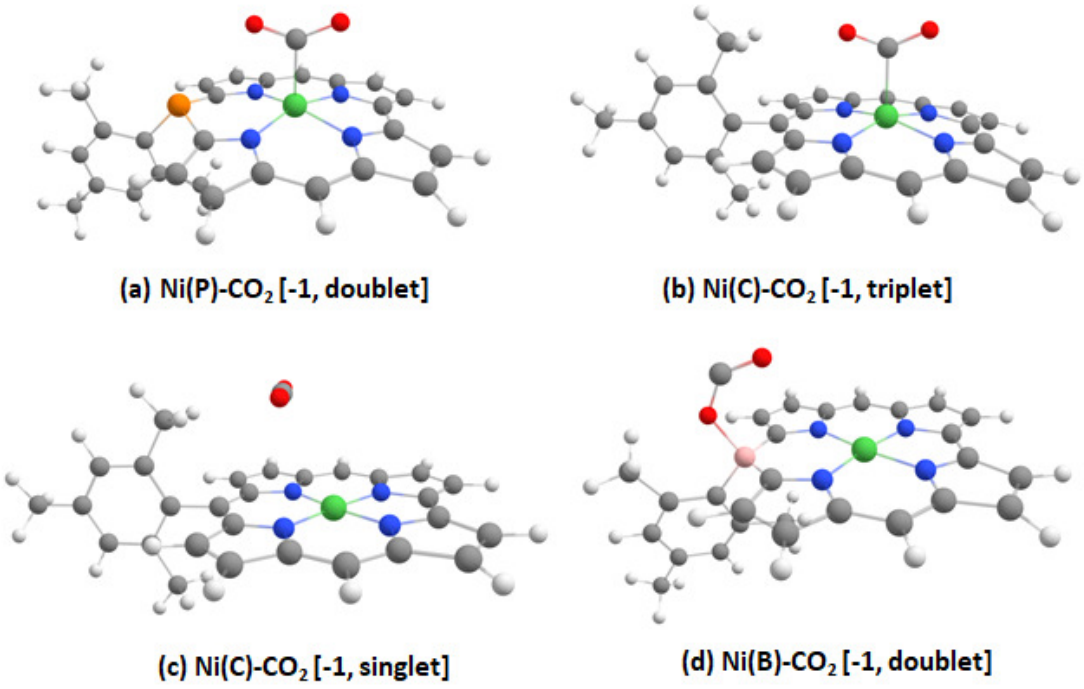

Figure 7.2: CO_2 adsorption at uni-negative systems. Grey atoms refer to C; green refers to Ni; blue refers to N; red refers to O; orange refers to P; pink refers to B.

favourable CO_2 adsorption with lowest endothermic adsorption energy value (8.8 kcal/mol) than uni-negative Ni(B) (36.6 kcal/mol). The active site of Ni(P) is different than that of Ni(B), for Ni(P) CO_2 gets adsorbed through C-center with Ni-C distance of 2.07 Åand pointing upward with $\angle OCO$ 133.7°; on the other hand for Ni(B) CO_2 gets adsorbed via O-center on B with B-O bond length of 1.61 Å and pointing downward with $\angle OCO$ 133.7°. In order to understand the nature of the bonding, we have investigated the orbital interactions and charge distributions of both the systems. For Ni(P), a transfer of electron density is found from Ni-center and nearby π-orbitals to the adsorbed CO_2 leaving an extra electronic charge (-0.31) on it and due to this all four Ni-N bonds become equivalent after little stretching. Now, for Ni(B) though the bonding between B-O centers apparently looks like electrophilic attack on O-center, however, NBO calculation suggest a flow of electron density from the nearby C-centers through B to the C-center of CO_2 leaving an extra electron charge of -0.56 on adsorbed CO_2 and the frontier orbitals show the interactions. As discussed earlier, Ni(C) should have favoured the CO_2 adsorption compared to Ni(B) and here all possible adsorption sites have been considered. But CO_2 does not get adsorbed at all and the minimum distance is found to be 3.35 Å with no charge transfer from Ni(C) to CO_2 as suggested by NBO calculation. This observation arises question whether CO_2 adsorption only depend on electron density of the system. So, we focused on other difference between Ni(C) and other two and found the uni-negative Ni(C) is singlet with no unpaired electron while other two are doublet. This intrigued us to check the CO_2 binding for triplet state of Ni(C) and the energy difference between the singlet and triplet state is 21.06 kcal/mol which favors the existence of this state. In case of triplet state, the CO_2 molecule gets bent ($\angle OCO = 134°$) with slight elongation of C-O bond (1.25 Å) but with quite high N-C distance of 3.54 Å . All the structures of adsorbed CO_2-systems are provided in Fig. 7.2

On the other hand, the dianionic Ni(C) is a spin doublet in the ground state,

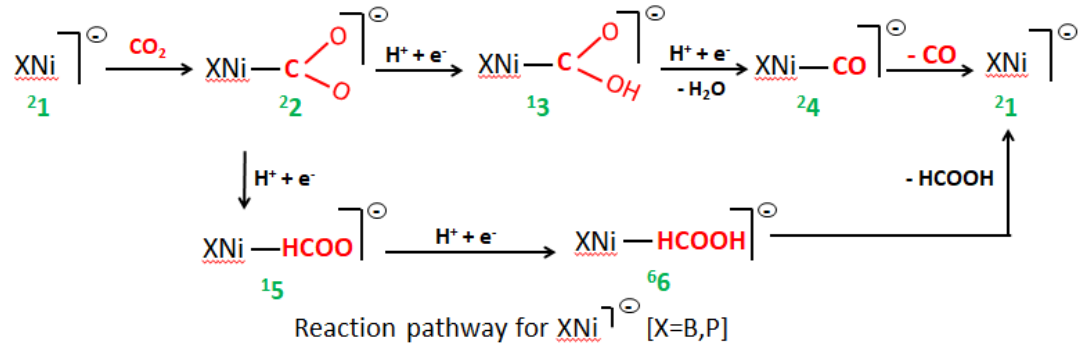

Figure 7.3: Schematic diagram of uni-negative(doublet) systems

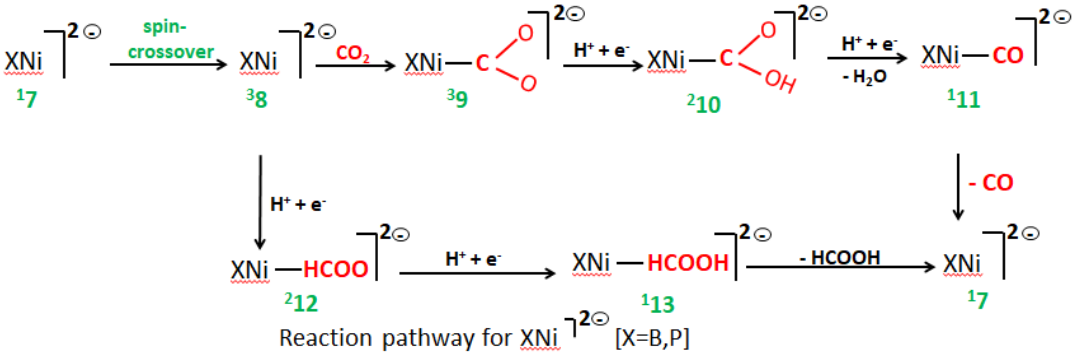

Figure 7.4: Schematic diagram of bi-negative(singlet) systems

while the other two are in spin singlet ground state. The CO_2 gets adsorbed on the Ni-center with Ni-C distance of 2.02 Å with an adsorption energy of 1.91 kcal/mol, while the other two, with spin singlet ground state, are unable to bind. We then looked at the triplet state of Ni(P) and Ni(B) systems (which had spin singlet as theirground state). The NBO studies suggest that in all the triplet cases, the transfer of electron density from Ni-center to the C-center of CO_2 occurs. So, we checked with the triplet state and found triplet Ni(P) and Ni(B) show feasible CO_2 adsorption with adsorption energy of -2.77 and 6.64 kcal/mol respectively. Incidentally, the triplet states in each case are quite closer to the singlet states with the energy difference of 4.30 and 17.08 kcal/mol for Ni(P) and Ni(B) respectively. These observations emphasize the importance of presence of unpaired electron over the electron density.

All the further steps are shown below through the schematic diagrams in Fig. 7.3 and 7.4. In the following equations systems are referred as Ni(X), where X=C, B, P

$$[Ni(X)]^{-1} + CO_2 \rightarrow [Ni(X) - (CO_2)]^{-1} \tag{7.3}$$

$$[Ni(X)]^{-1} + CO_2 + H^+ + e^- \rightarrow [Ni(X) - (COOH)]^{-1} \tag{7.4}$$

$$[Ni(X) - (COOH)]^{-1} + H^+ + e^- \rightarrow [Ni(X) - (CO)]^{-1} + H_2O \tag{7.5}$$

Since Ni(C) does not bind CO_2 in singlet or triplet state, we did not consider the concerted proton and electron transfer to adsorbed CO_2 here. There are three Ni(B)-COOH* intermediates with varying position of H(*COOH) having similar energy values i.e. -4.26 kcal/mol (trans-COOH* with H-facing towards B), -3.81 kcal/mol (cis-COOH*) and -0.27 kcal/mol (trans-COOH* with H-facing away from B) and Ni-C. All these structures have the Ni-C bond with average bond length of 2.025 Å and a significant amount of charge transfer has been observed from Ni-center to C-center as found from NBO and HOMO orbital analyses. In case

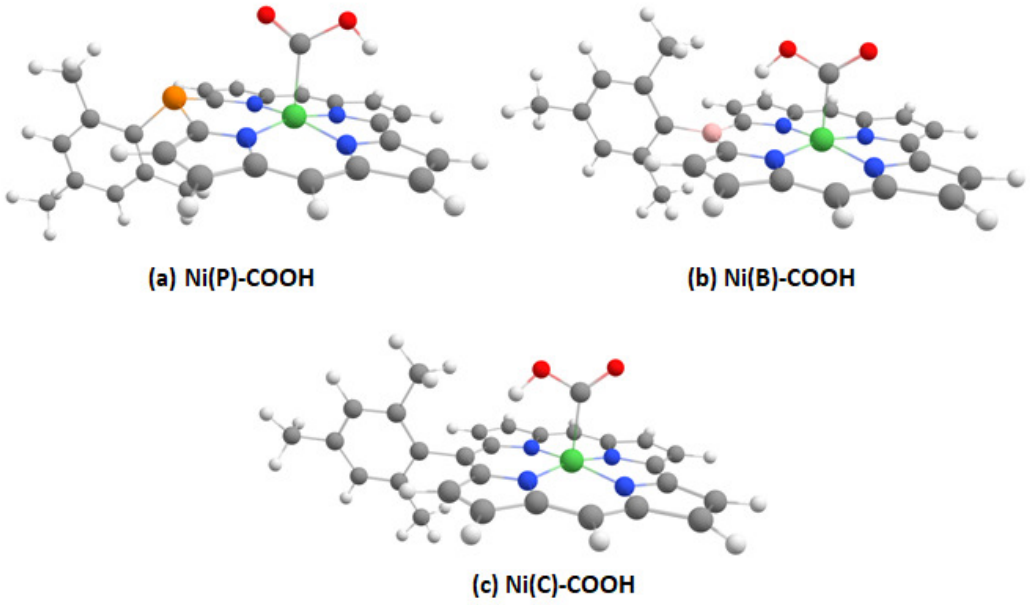

Figure 7.5: Interaction of COOH with the catalytic systems in uninegative states.

of first intermediate structure, the accumulation of charge over B-center suggest a weak interaction between H-atom of COOH with B at a distance of 2.56 Å . Degenerate *COOH intermediate structures for phosphacorrole have been found as well. The pathway gets completed with the formation of CO after a concerted H^+ and e^- transfer. The equilibrium potential corresponding to this step is 0.60 V for both Ni(B) and Ni(P), showing this step favorable. The same route has been considered for binegative Ni(C) system (which has favored the CO_2 adsorption) and in contrast to the Ni(P) and Ni(B) in uninegative states, COOH stays perpendicular facing downward with H(*COOH)-N and O(*COOH)-H(mesityl group) distance to be 2.26 and 1.99 Å respectively. The NBO analysis show excess charge on N-center (one interacting with COOH) favouring the interaction. The presence of HOMO orbital on *COOH suggest transfer of electron density from Ni(C) and the equilibrium potential of this and next step is -0.42 V and -0.30 V respectively. Intermediate structures are shown in Fig. 7.5.

As mentioned earlier, we have considered in detail the formation of HCOOH as a product through hydride transfer to the C-center of adsorbed *CO_2.

$$[Ni(X)]^{-1} + CO_2 + H^+ + e^- \rightarrow [Ni(X) - (OCHO)]^{-1} \tag{7.6}$$

$$[Ni(X) - (OCHO)]^{-1} + H^+ + e^- \rightarrow [Ni(X)]^{-1} + HCOOH \tag{7.7}$$

Interestingly, the *OCHO intermediate does not get adsorbed on any catalytic surface including uninegative Ni(B) and Ni(P) or binegative Ni(C). In each cases, we have considered all possible sites with different orientation of *OCHO intermediate but each time the structure gets optimized with the minimum distance of 3.20 Å from the catalyst surface. Unlike *COOH intermediate for binegative Ni(C) system, where a non-bonding interaction is present in between with a transfer of electron density to *COOH, here we have found no such interaction from NBO and MO-analysis. Due to the lack of interaction with the intermediate, here we discard the possibilities of formation of HCOOH.

7.3.1 Conclusion:

The preference of CO_2 adsorption towards the systems containing unpaired electron emphasize the fact that along with electron density this is also playing a crucial role. This fact is supported by the favourable adsorption of CO_2 by the triplet states compared to corresponding singlet state. Among the three considered systems, phosphacorrole in uni-negative state has shown best activity. We have explored all possible products from CO_2 reduction and CO is favourable product in each case. The reason behind is favourable interaction of the catalytic systems with the intermediate, *COOH.

References

[1] M. Goubeaud, G. Schreiner and R. K. Thauer, *European Journal of Biochemistry*, 1997, **243**, 110–114.

[2] M. Beley, J.-P. Collin, R. Ruppert and J.-P. Sauvage, *Journal of the Chemical Society, Chemical Communications*, 1984, 1315–1316.

[3] J. D. Froehlich and C. P. Kubiak, *Inorganic Chemistry*, 2012, **51**, 3932–3934.

[4] M. Beley, J. P. Collin, R. Ruppert and J. P. Sauvage, *Journal of the American Chemical Society*, 1986, **108**, 7461–7467.

[5] M. Fujihira, Y. Hirata and K. Suga, *Journal of Electroanalytical Chemistry and Interfacial Electrochemistry*, 1990, **292**, 199–215.

[6] G. B. Balazs and F. C. Anson, *Journal of Electroanalytical Chemistry*, 1992, **322**, 325–345.

[7] J. Schneider, H. Jia, K. Kobiro, D. E. Cabelli, J. T. Muckerman and E. Fujita, *Energy & Environmental Science*, 2012, **5**, 9502–9510.

[8] J. Song, E. L. Klein, F. Neese and S. Ye, *Inorganic Chemistry*, 2014, **53**, 7500–7507.

[9] J. D. Froehlich and C. P. Kubiak, *Journal of the American Chemical Society*, 2015, **137**, 3565–3573.

[10] F. Abba, G. De Santis, L. Fabbrizzi, M. Licchelli, A. M. Manotti Lanfredi, P. Pallavicini, A. Poggi and F. Ugozzoli, *Inorganic Chemistry*, 1994, **33**, 1366–1375.

[11] V. S. Thoi and C. J. Chang, *Chemical Communications*, 2011, **47**, 6578–6580.

[12] S. Meshitsuka, M. Ichikawa and K. Tamaru, *Journal of the Chemical Society, Chemical Communications*, 1974, 158–159.

[13] J. Grodkowski, P. Neta, E. Fujita, A. Mahammed, L. Simkhovich and Z. Gross, *The Journal of Physical Chemistry A*, 2002, **106**, 4772–4778.

[14] S. Gonglach, S. Paul, M. Haas, F. Pillwein, S. S. Sreejith, S. Barman, R. De, S. Müllegger, P. Gerschel, U.-P. Apfel *et al.*, *Nature Communications*, 2019, **10**, 1–10.

[15] R. De, S. Gonglach, S. Paul, M. Haas, S. Sreejith, P. Gerschel, U.-P. Apfel, T. H. Vuong, J. Rabeah, S. Roy *et al.*, *Angewandte Chemie*, 2020.

[16] H. Omori, S. Hiroto, Y. Takeda, H. Fliegl, S. Minakata and H. Shinokubo, *Journal of the American Chemical Society*, 2019, **141**, 4800–4805.

[17] A. D. Becke, *Journal of Chemical Physics*, 1993, **98**, 5648–5652.

[18] C. Lee, W. Yang and F. Parr, *Condens. Matter*, 1988, **37**, 785.

[19] A. V. Marenich, C. J. Cramer and D. G. Truhlar, *The Journal of Physical Chemistry B*, 2009, **113**, 6378–6396.

[20] M. Frisch, G. Trucks, H. Schlegel, G. Scuseria, M. Robb, J. Cheeseman, G. Scalmani, V. Barone, G. Petersson, H. Nakatsuji *et al.*, *Wallingford CT*, 2016, **2**, year.

8

Summary and Outlook

In the thesis, we have looked into the catalytic activities of both heterogeneous and homogeneous catalytic systems. In chapter 2, 6 and 7, we have focused on theoretical analyses of OER and CO2 reduction reaction; in chapter 2, we have proposed a series of doped O-deficient double perovskites ($Ca_2Mn_2O_5$) [dopants: Sr, In, Bi, La, Ce, Eu] with varying % from 10 to 40% exhibiting better oxygen evolution activity compared to the pristine one. Based on the calculations, we have proposed linear regression based machine-learning model with the structural properties (Fermi level, p-band center, covalency, Goldschmidt tolerance factor) as descriptors, which can be easily obtained, with reasonable good accuracy (Pearson correlation factor, $R^2 = 0.86$). In chapter 6 and 7, we have studied role of homogeneous catalysts for CO_2 reduction in basic and acidic medium respectively. In chapter 6, detailed kinetic analysis of all possible pathways of Co(I)-PNP pincer complex with secondary and tertiary amine have been carried out in order to find out the underneath reasons behind the huge difference in catalytic activity of tertiary amine system (turn over number $\sim$ 64 times higher) than the secondary analogue. In this context, we have also discussed about the role of metal ligand cooperativity (MLC) in both cases as to verify previous anticipation that MLC is reason behind the huge difference in catalytic activities of the two almost similar

structures. Chapter 7 explores the CO_2 reduction activity of Ni(II) corrole and recently synthesized Ni(II) phosphacorrole and Ni(II) boracorrole in acidic medium. Here we have explored the effects of electron density upon CO_2 adsorption and considered the thermodynamic feasibility of all possible reaction pathways.

In chapter 3, 4 and 5, we have carried out detailed theoretical works with experimental group and tried to find out the electronic reasons behind their observations. In chapter 3 and 4, Prof. P. Barpanda and his group have considered pyrophosphate and a group of fluorophosphate respectively, as bifunctional catalysts (i.e. showing both oxygen evolution and reduction reaction) and found to show excellent catalytic activity. Here, we have modelled the systems, considered the reaction pathways and explained about their stability and superior activities. Qualitatively, our results match with the experimental observations. In chapter 5, we have collaborated with Prof. T. Maji and his group, where they have synthesized a system from Co-MOF showing a good activity towards the three reactions (oxygen evolution, oxygen reduction and hydrogen evolution) hence known as exhibiting trifunctionality. We have systematically model the systems with the help of the peaks from XPS and studied their hydrogen evolution reactivity. We were able to find out the active site as well.

Thus far during my graduation years, I have studied heterogeneous and homogeneous systems separately, have found that both of them have their pros and cons. In future, I intend to work on heterogenized molecular systems, which belong to an emerging field and grabbing a great attentions in the recent years. We all are already aware of the fact that homogeneous systems show higher selectivity but while attaching them with the electrodes might affect their reactivity. Heterogenized molecular system can help in solving this issue, as in this case, the molecular structure is already doped or put on the suitable heterogeneous systems and afterward their catalytic activity will be studied. However, the the kinetic stability of the system needs to be verified.

In this thesis, we have used density functional based computational tools to analysis, which does not consider the temperature effects or dynamic variations. From T=0 static nudged elastic band data, we need to do the necessary calculations to check the kinetic path and stability at finite temperature, which can be done using kinetic monte carlo methods. In fact, I also have interest to develop microkinetics algorithm together with the machine learning methods by which various industrial scale reactions can be studied on a number of active and inexpensive surfaces.